PHYSICAL ADSORPTION ON SINGLE WALL CARBON NANOTUBES

by

Petro Kondratyuk

B.S., Kiev National University, Kiev, Ukraine, 2000

M.S., Kiev National University, Kiev, Ukraine, 2001

Submitted to the Graduate Faculty of
Arts and Sciences in partial fulfillment
of the requirements for the degree of
Doctor of Philosophy

University of Pittsburgh

2007

UNIVERSITY OF PITTSBURGH

FACULTY OF ARTS AND SCIENCES

This dissertation was presented

by

Petro Kondratyuk

It was defended on

April 26, 2007

and approved by

Prof. J. Karl Johnson, Department of Chemical Engineering

Prof. Kenneth D. Jordan, Department of Chemistry

Prof. David W. Pratt, Department of Chemistry

Dissertation Advisor: Prof. John T. Yates, Jr., Department of Chemistry

PHYSICAL ADSORPTION ON SINGLE WALL CARBON NANOTUBES

Petro Kondratyuk, Ph.D.

University of Pittsburgh, 2007

The adsorption of molecules on single wall carbon nanotubes in the regime of physical adsorption was investigated by means of temperature programmed desorption (TPD) and infrared spectroscopy under ultrahigh vacuum conditions.

Three adsorption sites could be resolved in the TPD spectra of a number of molecules, such as CCl_4, normal alkanes with 5-9 carbon atoms in the chain, and an unsaturated hydrocarbon, 1-heptene. The resolution of spectral features in the TPD spectra is especially pronounced in the case of normal alkane molecules. By comparison with theoretical simulations, these three adsorption sites were shown to correspond to: (1) to the nanotube interior; (2) the groove sites between adjacent nanotubes on the outside of the nanotube bundles; and (3) the exterior surface of the nanotubes. The nanotube interior has the highest binding energy, followed by the groove sites and exterior sites.

When two different adsorbates, such as CCl_4 and n-C_9H_{20}, are coadsorbed on nanotubes, the adsorbate with higher polarizability (n-nonane) occupies the more highly-binding adsorption sites, qualitatively displacing the other adsorbate to sites with lower binding energies.

By studying the dependence of the capacity of the adsorption sites on the shape and length of the adsorbed molecules, it was shown that linear groove sites behave as a one-dimensional adsorption space. In contrast, the interior adsorption sites, which have diameters substantially larger than the size of the typical adsorbate molecules, behaved as a three-dimensional adsorption space.

When 1-heptene confined inside nanotubes was subjected to a flux of an aggressive chemical agent, atomic H, it was seen that the rate of reaction was 3-4 times slower compared to 1-heptene on the exterior of the nanotubes. This demonstrates that the nanotube walls can provide shielding for interior-adsorbed species.

Infrared spectroscopy showed that the ν_3 vibrational mode of CF_4 (the mode with the highest transition dipole moment) shifts to lower frequency upon adsorption on carbon nanotubes. The shift is greatest for the internally-adsorbed species (35 cm^{-1}), while the exterior-adsorbed CF_4 shows a shift of 15 cm^{-1}. This points at the stronger van der Waals interaction when the molecule is adsorbed in the interior.

TABLE OF CONTENTS

LIST OF TABLES

LIST OF FIGURES

PREFACE

This Dissertation summarizes the results of the research that was conducted while I was in graduate school at the Surface Science Center in the department of Chemistry, University of Pittsburgh. Not even a fraction of this work could be accomplished without the direction, help and advice from the many people that I worked with. Most notably, I sincerely thank my research advisor, Professor John T. Yates, Jr., for his endless dedication and patience. It was an honor to work and learn in his group.

I also thank Professor J. Karl Johnson, as well as his postdocs and graduate students, whose theoretical contributions enriched and gave a new perspective to many pieces of research work discussed here.

I gratefully acknowledge the help and support from all members of the Surface Science Center, and numerous members of the Department of Chemistry. I thank my fellow graduate student, Oleg Byl, with whom I worked on a number of research projects, for practical help and interesting discussions.

I thank the Army Research Office (ARO) for the funding of this work.

LIST OF PUBLICATIONS

1. Petro Kondratyuk, John T. Yates, Jr. **Molecular Views of Physical Adsorption Inside and Outside of Single Wall Carbon Nanotubes (Review).** Accepted by Accounts of Chemical Research.

2. Petro Kondratyuk, John T. Yates, Jr. **Effects of molecular confinement inside single walled carbon nanotubes on molecular reactivity – atomic H + 1-heptene.** Accepted by JACS.

3. Petro Kondratyuk, Yang Wang, Jinchen Liu, J. Karl Johnson and John T. Yates, Jr. **Inter- and intra-tube self-diffusion in n-heptane adsorbed on carbon nanotubes.** Journal of Physical Chemistry C (2007), 111, 4578-4584.

4. Petro Kondratyuk, Yang Wang, J. Karl Johnson, John T. Yates, Jr. **Observation of a one-dimensional adsorption site on carbon nanotubes: adsorption of alkanes of different molecular lengths.** Journal of Physical Chemistry B (2005), 109, 20999-21005.

5. Petro Kondratyuk, John T. Yates, Jr. **Desorption kinetic detection of different adsorption sites on opened carbon single walled nanotubes: the adsorption of n-nonane and CCl_4.** Chemical Physics Letters (2005), 410, 324-329.

6. Petro Kondratyuk, John T. Yates, Jr. **Design and construction of a semiautomatic temperature programmed desorption apparatus for ultrahigh vacuum.** Journal of Vacuum Science & Technology A (2005), 23, 215-217.

7. Petro Kondratyuk. **Analytical formulas for Fermi resonance interactions in continuous distributions of states.** Spectrochimica Acta (2005), 61A, 589-593.

8. Oleg Byl, Petro Kondratyuk, John T. Yates, Jr. **Adsorption and dimerization of NO inside single-walled carbon nanotubes - an Infrared Spectroscopic Study.** Journal of Physical Chemistry B (2003), 107, 4277-4279.

9. Oleg Byl, Petro Kondratyuk, Scott T. Forth, Stephen A. FitzGerald, Liang Chen, J. Karl Johnson, John T. Yates, Jr. **Adsorption of CF_4 on the internal and external surfaces of opened single-walled carbon nanotubes: a vibrational spectroscopy study.** Journal of the American Chemical Society (2003), 125, 5889-5896.

10. Petro Kondratyuk, John T. Yates, Jr. **Nanotubes as molecular sponges: the adsorption of CCl_4.** Chemical Physics Letters (2004), 383, 314-316.
11. Dimitar Panayotov, Petro Kondratyuk, John T. Yates, Jr. **Photooxidation of a Mustard Gas Simulant over TiO_2-SiO_2 Mixed-Oxide Photocatalyst: Site Poisoning by Oxidation Products and Reactivation.** Langmuir (2004), 20, 3674-3678.

1.0 INTRODUCTION

The first experimental observation of carbon nanotubes by Iijima in 1991 [1] opened up a field of research that has since been seeing a flurry of scientific activity. Countless applications of nanotubes were proposed with a view to exploiting the unique electronic, mechanical, and adsorptive properties they possess.

At present time, about 19,000 papers have been published on carbon nanotubes and about 5% of these relate to their adsorption properties. Figure 1 shows the evolution of the total research activity on nanotubes since the birth of this field. A doubling of research activity occurs every 2-3 years, even 10 years after the discovery of this interesting allotrope of carbon.

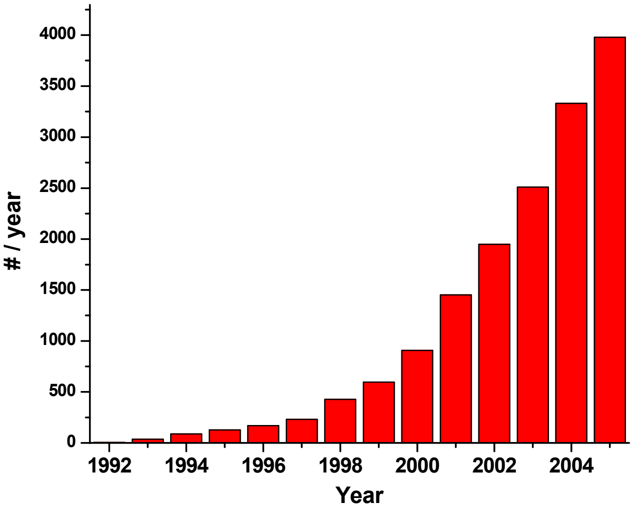

Figure 1. Number of scientific publications on carbon nanotubes per year since their discovery (from the Chemical Abstracts database).

1.1 STRUCTURE OF CARBON NANOTUBES

Carbon nanotubes are long cylindrical structures consisting of sheets of sp^2-hybridized carbon. When the carbon atom is in the sp^2 hybridization state, one *s* and two *p* orbitals are mixed, giving three orbitals pointing to the vertices of an equilateral triangle. These three orbitals are capable of producing σ bonds. The remaining *p* orbital, lying perpendicular to the triangle, can interact with identical *p* orbitals on other carbon atoms giving π bonds. Thus, a sheet-like structure can be formed from sp^2-hybridized carbon. The sheets are commonly referred to in the literature [for instance, ref. 2] as graphene sheets when they are considered as separate entities. In graphite, a layered structure is formed from such graphene sheets. Each atom in graphite forms three σ bonds with its neighbors in the layer and contributes its p orbital to the delocalized π cloud. The resulting bond is 142 pm long with formal order of 1.33 [3]. In contrast to strong bonding in the layer, the bonds between the layers are weak van der Waals type.

It was predicted as early as 1970 [4, 5], far before the first experimental observations, that stable closed shell structures with graphene-like connectivity must exist. The formation of such closed shell molecules, later called fullerenes, was indeed confirmed in the experiments of Kroto, Smalley and others in 1985 [6], who discovered the C_{60} molecule, a closed polyhedron.

It follows from a consequence of Euler's theorem that a closed polyhedron cannot consist entirely of hexagons and has to include exactly 12 pentagons [7]. Thus, if a closed structure is built from a finite graphene sheet, it must contain 12 pentagonal rings. The smallest stable structure of this type is C_{60}, buckminsterfullerene, which has 12 pentagonal and 20 hexagonal faces. Although the number of pentagons is always 12, the number of hexagons is not limited, and one can imagine rolling up a graphene sheet (consisting only of hexagons) to form a cylinder and creating a hemispherical surface containing a mixture of pentagons and hexagons at the ends of the cyllinder to close the shape. The hollow tubular structures of sp^2-hybridized carbon that one obtains in this way are known as *closed carbon nanotubes*. Figure 2 shows schematic models of three nanotubes with different hexagon orientations.

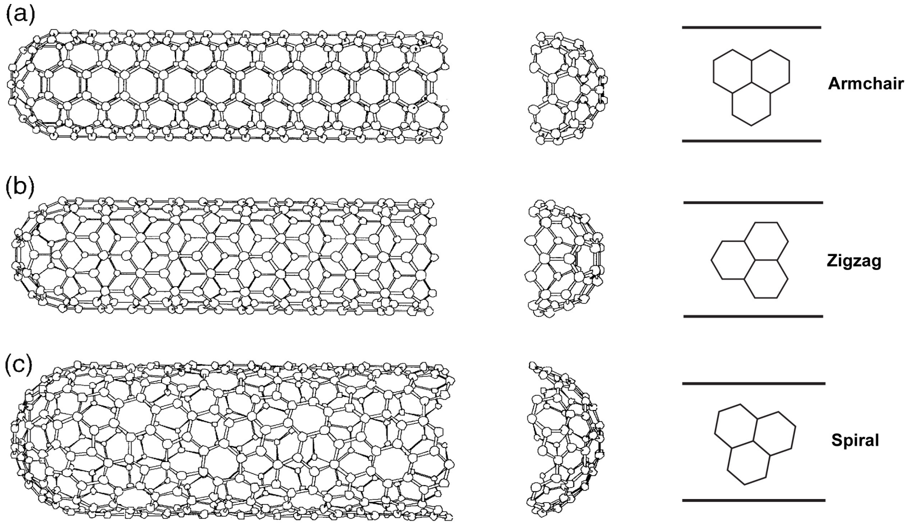

Figure 2. Schematic models of nanotubes: (a) - armchair (5,5) nanotube, (b) – zigzag (9,0) nanotube, (c) - chiral (10,5) nanotube. Schematics on the right show the relative orientation of hexagons with respect to the tube axis. Fullerene-like end caps are also shown. The images of the nanotubes are reproduced with permissions from M.S. Dresselhaus et al., Carbon 1995, 33, 883 [8]. Copyright 1995, Elsevier.

The hexagon orientation with respect to the nanotube axis in combination with its diameter uniquely determines the nanotube structure. The most straightforward way of specifying the structure is the vector model [9]. The (two-dimensional) vector that joins two equivalent points on the graphene lattice is expressed as

$$C = n \cdot a_1 + m \cdot a_2 \qquad (1)$$

where n and m are integers and a_1 and a_2 are unit cell base vectors for the graphene sheet, shown in Figure 3. Vector C points from the (0,0) point in Figure 3 to other bold dots denoting different nanotubes. Integers in parentheses are (n,m) pairs.

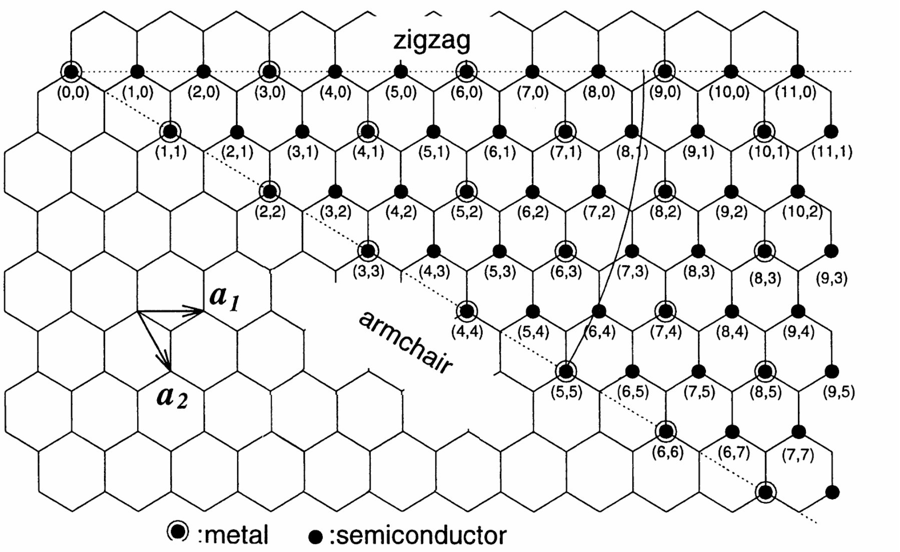

Figure 3. Possible ways of folding a graphene sheet to obtain a carbon nanotube. The (n,m) pairs specify the vector joining two identical points on the nanotube. Vectors a_1 and a_2 are the unit cell base vectors of graphene. Reproduced with permission from M.S. Dresselhaus et al., Carbon 1995, 33, 883 [8]. Copyright 1995, Elsevier.

When the graphene sheet in Figure 3 is "rolled up" so that the (0,0) point joins the other point indicated by a pair of (n,m) integers, a nanotube is formed. The tubule thus generated has no distortions of the bond angles other than caused by the cylindrical curvature.

The chiral angle θ is defined as the angle between vectors C and a_1. Differences in the angle θ and tubule diameter give rise to differences in the properties of various carbon nanotubes.

The so-called armchair configuration of the nanotube is obtained when n=m. When m=0, the configuration is referred to as zigzag. These two types of nanotubes are achiral, that is, they can be superimposed with their mirror images. All other nanotubes have lower symmetry and are chiral [10]. Since the chiral nanotubes can exist as both right- and left-handed enantiomers, they are optically active to polarized light propagating along the nanotube axis.

In order to avoid giving different (n,m) indexes to identical nanotubes, which can occur due to symmetry of the graphene sheet, an additional requirement is introduced, that $n \geq m$, and n and m must both be nonnegative. This results in the selection of “irreducible wedge” on the graphene sheet, shown in Figure 3 by an arc spanning 30°.

The diameter d can be expressed in terms of integers n and m as

$$d = \sqrt{3} \cdot a \cdot \sqrt{m^2 + mn + n^2} / \pi , \qquad (2)$$

where a is the distance adjacent carbon atoms (0.1421 nm in graphite). The chiral angle, θ, is given by

$$\theta = Arc\tan[\sqrt{3}m/(m+2n)]. \quad (3)$$

All zigzag tubes will have θ=0 ° according to this formula, while for armchair tubes θ=30°.

Initially the nanotubes were observed in the transmission electron microscopy (TEM) images of the soot formed on the negative electrode in an arc between two carbon electrodes in inert atmosphere [1]. Later an efficient method of synthesis capable of producing large quantities of nanotubes was developed [11, 12]. These were so-called multiwall carbon nanotubes (MWNTs), as they consisted of several nested tubes, with diameters typically between 2 and 20 nm. The spacing between the layers is slightly larger than in graphite (0.340 versus 0.335 Å) due to geometrical constraints caused by curvature. Unlike in graphite, the layers are rotationally disordered, as it is in general not possible to create a matching nested structure. The length could reach several micrometers, giving an aspect ratio of the order of 10^3-10^4.

Another type of nanotubes, containing just a single graphene cylinder, was first synthesized independently by Iijima and Ichihashi [13] and Bethune et al. in 1993 [14]. They are typically referred to as single wall carbon nanotubes (SWNTs). In SWNTs, unlike in MWNTs, no surfaces are closed to adsorption by graphite-like layering. The studies described in this dissertation used SWNTs. Unlike the multiwall nanotubes, which grow on the surface of the electrode, SWNTs grow in the gas phase and require a catalyst - a transition metal element such as Ni, Co, Y or Fe. In the *arc discharge synthesis method* the metal is co-evaporated with graphite in the electric arc [15, 16]. SWNTs generally exhibit smaller diameters compared to MWNTs, usually in the range from 8 to 18 Å. It was theoretically predicted that the nanotubes should be stable down to the diameters of around 3-4 Å [17]. Below this diameter the strain produced by the curvature of the walls should make the structure unstable [18]. Confirming the predictions, experimental work has demonstrated the possibility of synthesis of 4 Å diameter nanotubes [19].

Considering that the strain energy is proportional to $1/d^2$, there is no theoretical limit on the upper radius of the nanotubes [20], although one should expect that the formation of very large tubes would be limited kinetically compared to the smaller diameter ones, since entropy per atom is smaller in larger tubes. At large radii, the properties of the nanotubes can be expected to asymptotically approach those of graphene.

A very efficient method of synthesis of SWNTs involves laser vaporization of graphite mixed with metal catalyst in a 1200^{o} C furnace [21, 22]. By using bimetallic Ni-Co catalyst, as much as 70% of the evaporated graphite could be converted into SWNTs. The SWNTs used in the experiments discussed here were produced by this method.

Another group of methods that lead to the production of SWNTs is based on chemical decomposition of organic molecules on supported nanocrystalline catalytic particles (typically transition metals and their oxides). Significant progress was made with such molecules as C_2H_4, CO [23, 24] and CH_4 [25]. These methods offer the advantage of being readily scalable to large volumes. *The high pressure CO* ("HiPco") *process* is a gas-phase synthesis [26], however its mechanism is similar. CO gas with a small concentration of $Fe(CO)_5$ is passed into the reaction zone kept at 800-1200^{o}C. At this temperature $Fe(CO)_5$ decomposes forming iron nanoclusters that catalyze the CO disproportionation reaction leading to C and CO_2. Carbon is deposited on the catalytic particles in the form of SWNTs. The HiPco process has the advantage of giving nanotubes with small diameters (down to 7 Å) that are essentially free of an amorphous carbon overcoating.

During the formation phase, van der Waals forces between the individual nanotubes cause them to form ropes, or bundles, consisting of tens of axially aligned nanotubes [22, 27]. The structure of the bundle is a hexagonal array of nanotubes with a nanotube-nanotube spacing of around 3.4 Å, as has been verified by TEM and XRD studies [28, 29]. Figure 4 shows a typical SEM image of SWNT material.

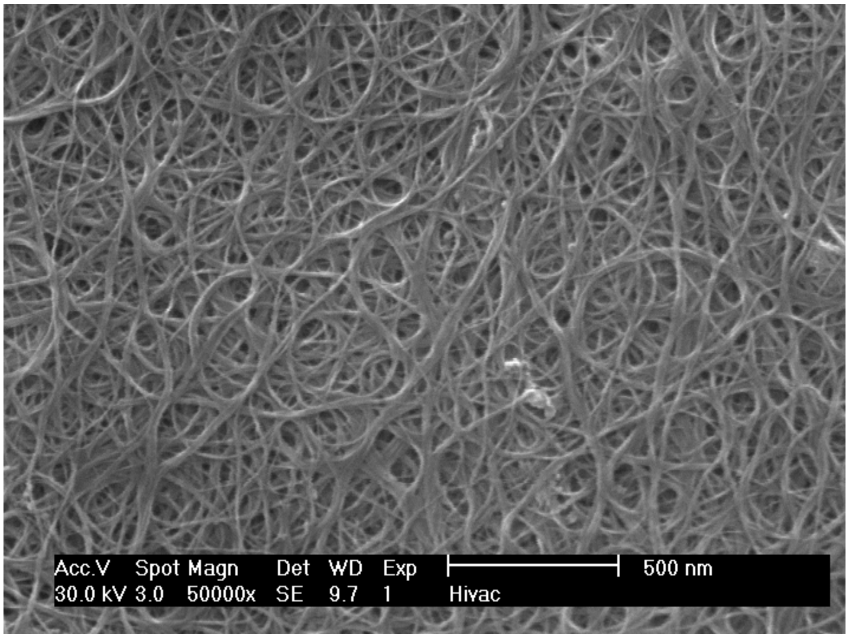

Figure 4. SEM image of SWNT material used in this work. Reproduced with permission from Kuznetsova et al., J. Chem. Phys. 2001, 115, 6691. Copyright 2001, American Institute of Physics.

The “ropes” visible in the image are the entangled bundles of SWNTs. In the axial direction the structure of the bundles is similar to the structure of nematic crystals – when one nanotube ends, other nanotubes take its place giving bundles that can be centimeters long [30].

Nanotubes in the bundle do not all have the same diameter, resulting in various imperfections in the bundle structure.

1.2 MECHANICAL AND ELECTRONIC PROPERTIES

Mechanical and electronic properties of nanotubes have attracted a large amount of interest. With Young's modulus comparable to that of the diamond (1.1-1.3 TPa) [31], nanotubes show surprising flexibility under loads [32]. Even large deformations are not permanent, and once the deforming force is removed, the structure is fully restored. This elastic, rather then brittle, behavior for such a hard material indicates extreme strength (Figure 5). One of the consequences of a very high Young's modulus of carbon nanotubes is very a high thermal conductivity (around 3000 W/K*m) [33], resulting from a high phonon propagation velocity in the graphene-like structure.

Figure 5. Simulated bending of a nanotube under a deforming force. Deformation is elastic rather than permanent. Reproduced with permission from B.I. Yakobson et al., Phys. Rev. Lett. 1996, 76, 2511 [32]. Copyright 1996, American Physical Society.

Studies of the electron conduction by the nanotubes showed a ballistic transport of carriers (almost without scattering) [34] and capability to withstand current densities of up to 10^9 A/cm^2 [35].

Nanotubes show either metallic or semiconducting behavior. A simple rule connects (n,m) integers with metallicity and semiconductivity: if (n-m) is divisible by 3, then the nanotube is metallic; if not, it is semiconducting. It follows that of the possible nanotube structures, two thirds are semiconductors, while the rest are metallic (in particular, all armchair tubes are metallic). Figure 6 shows the electronic density of states plots for two nanotubes – semiconducting (10,0) and metallic (9,0). The density of states for graphite, a zero band gap semiconductor, is shown for comparison by the dotted line.

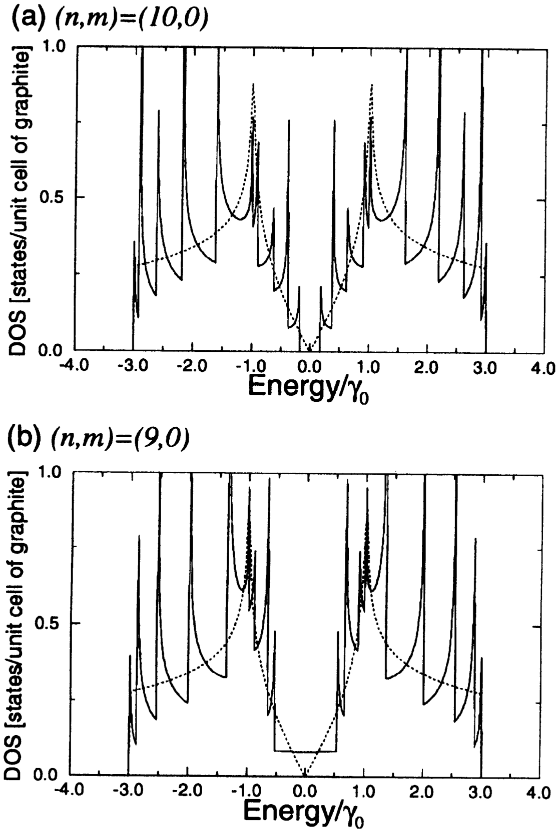

Figure 6. Electronic density of states (DOS) per unit cell of graphene lattice: (a) for a semiconducting (10,0) nanotube, and (b) for metallic (9,0) nanotube. DOS for the graphene sheet is shown for comparison (dotted line). The Fermi edge is at 0 energy. γ_0 is the energy of the nearest-neighbor overlap integral for graphite. Reproduced with permission from T.D. Burchell (ed.),"Carbon Materials for Advanced Technologies". Copyright 1996, Elsevier.

The (9,0) nanotube, unlike (10,0), has a finite density of states at the Fermi level. It must be expected that as the diameter of the nanotube increases, its electronic, mechanical and chemical properties must asymptotically approach those of graphene, as graphene can be thought of as an infinite-diameter nanotube. It is indeed observed that the band gap for semiconducting nanotubes decreases with diameter [36] (proportionally to 1/d), as does the density of states at the Fermi level for metallic nanotubes. For large diameters the distinction between the two types of tubes disappears as they approach the electronic structure of graphene.

From the standpoint of applications [37, 38], it is important that either a synthetic method be developed capable of producing substantial quantities of nanotubes with given electronic properties, or a suitable separation procedure be found. The latter direction has recently started to show promise. Dielectrophoretic separation [39] employs the difference in relative dielectric constants of the two nanotube species, with metallic nanotubes being attracted to a set of electrodes while semiconducting ones remain in the solvent. Authors estimate that in their experiment about 100 pg of metallic nanotubes were separated from an initial 100 ng sample with this technique. A method developed by Papadimitrakopoulos and coworkers [40] is based on preferential physisorption of octadecylamine on semiconducting nanotubes in tetrahydrofuran suspension. The metallic nanotubes tend to precipitate out with increasing concentration of the suspension. The method could potentially be scaled up to produce gram quantities of nanotube material enriched in one type of nanotubes. Zheng et al. [41] took another approach. A systematic search enabled them to select a DNA sequence that self-assembles around the individual nanotubes in such a way that the interaction with the nanotube depends on the diameter and the electronic properties, which allowed separating the nanotubes with anion exchange chromatography. Optical adsorption and Raman spectroscopy showed that the early fractions are enriched in small diameter and metallic nanotubes. Chen et al. [42] used preferential formation of charge-transfer complex of metallic nanotubes with bromine. The increased density of bromine-containing nanotube material allowed them to use a centrifugation-based separation procedure. With the most efficient separation parameters the authors could obtain samples that were 2.8 times richer in metallic nanotubes than the initial material.

1.3 ADSORPTION ON CARBON NANOTUBES[1]

Single wall carbon nanotubes (SWNTs) occupy an interesting place among carbonaceous adsorptive materials. On one hand, they offer chemically inert surfaces for physical adsorption, and their high specific surface areas are comparable to those of activated carbons (surface areas of up to 1600 m^2/g have been reported [43, 44]. On the other hand, SWNTs are fundamentally different from activated carbons in that their structure at the atomic scale is far more well-defined and uniform. While parameters such as the pore diameter distribution and adsorption energy distribution are needed to quantify adsorption on activated carbons, in the case of carbon nanotubes one can deal directly with various well-defined adsorption sites available to the adsorbing molecules. From the standpoint of structure, the relationship between carbon nanotubes and other carbonaceous adsorptive materials is similar to that between single crystals and polycrystalline materials.

---

[1] This section is reproduced with modifications from a manuscript by P. Kondratyuk and J.T. Yates, Jr., titled “Molecular Views of Physical Adsorption Inside and Outside of Single Wall Carbon Nanotubes” which has been accepted for publication in the Accounts of Chemical Research, published by the American Chemical Society.

1.3.1 Adsorption sites on carbon nanotubes

As mentioned before, SWNTs associate with each other due to attractive dispersive forces to form bundles, typically comprising tens or hundreds of individual nanotubes. Adsorption of molecules takes place on these bundles. Thus to gain insight into adsorption on SWNTS it is instructive to consider the structure of the bundle and the adsorption sites available to the adsorbate molecules (Figure 7).

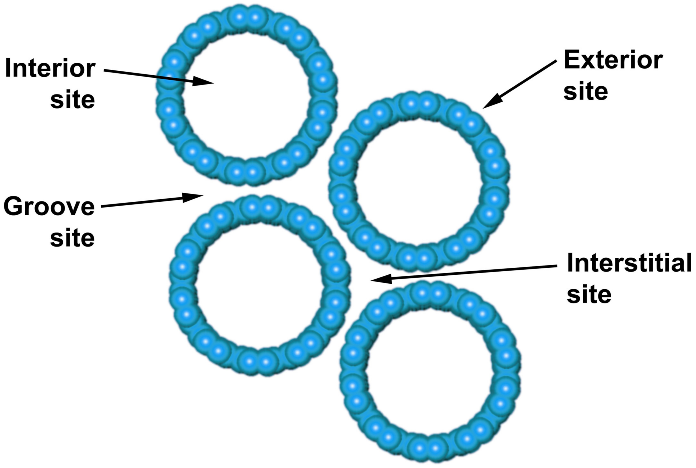

Figure 7. A schematic of a hexagonally packed SWNT bundle consisting of four (10, 10) nanotubes viewed end-on. Four types of adsorption sites are shown.

Four types of adsorption sites can be identified: the nanotube interior sites, the sites on the exterior surface, the groove sites, and the interstitial sites. The groove sites are narrow troughs formed on the outside of the bundles where two nanotubes meet. The interstitial sites are channels between individual nanotubes inside the bundle. It has been theoretically predicted that only the smallest adsorbate molecules (such as H2, He and Ne) can access the interstitial channels in a hexagonally packed bundle of typical SWNTs [45]. It has been further suggested that in non-ideally packed bundles the channels can become large enough for adsorption of other adsorbates [46]. However, experimental results indicate that the contribution of the interstitial channels to the total adsorptive capacity is negligible [47-49].

The nanotube interior is expected to have a high binding energy toward adsorbing molecules because the closeness of the surrounding walls to the adsorbed molecule maximizes the attractive van der Waals interaction. On the contrary, on the nanotube exterior the walls curve away from the adsorbed molecules, meaning that the adsorption energy must be smaller compared to the interior, and compared to flat graphene. This intuitive picture is corroborated by molecular simulations [45, 50] and experimental results [51]. Simonyan et al. [50] calculated the potential energy of a Xe atom in the interior and on the exterior of a (10,10) single wall nanotube having a diameter of 13.6 Å. The plot of the potential energy versus distance from the nanotube center is shown in Figure 8. The difference between the adsorption energies for the interior and exterior surfaces was found to be about 800 K. An experimental estimate of the binding energy of Xe on untreated (closed) carbon nanotubes was recently provided by Rawat et al. [51]. The authors placed this value at 256 meV (2970 K), which is ~60% higher than the binding energy of Xe on a flat graphite surface.

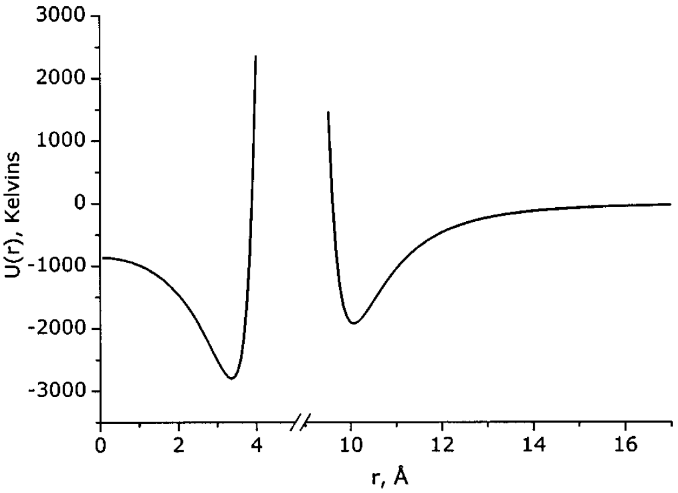

Figure 8. Interaction potential for a Xe atom in the vicinity of a (10,10) SWNT. The zero on the distance axis corresponds to the center of the nanotube. The curve on the left corresponds to a Xe atom inside the SWNT, while that on the right corresponds to a Xe atom outside of the SWNT. Reproduced with permission from V. Simonyan et al., J. Chem. Phys. 2001, 114, 4180 [50]. Copyright 2001, American Institute of Physics.

As far as the adsorption energies for the groove sites are concerned, theoretical and experimental work has shown that the adsorption energy for groove sites present on the exterior of the SWNT bundles lies in between the adsorption energies for exterior and interior sites [52].

1.3.2 Molecular access into the nanotube interior

In the synthesized material, nanotube ends are closed by hemispherical fullerene-like caps that block molecular access into the nanotube interior [7]. However, it is the nanotube interior that presents the most interest for the adsorption of molecules as far as potential practical applications are concerned, owing to its deep potential well and significant capacity [45, 53].

Thus, an opening process is needed capable of removing the end caps to enable interior adsorption. Kuznetsova [54] observed that an aqueous phase acidic oxidative process developed by the Smalley group [55] and usually employed for nanotube purification also opens the end caps for Xe adsorption. This purification procedure is used to dissolve graphitic impurities and Ni-Co catalyst particles present in the as-synthesized SWNTs. The procedure consists of treatment with an aqueous solution of HNO_3/H_2SO_4 followed by sonication in aqueous H_2O_2/H_2SO_4 [55]. Aside from opening the end caps, this procedure also results in the cutting of the SWNTs, decreasing the average length of the SWNTs in the sample. It was found that after purification both the capacity and the sticking coefficient of SWNTs toward Xe at 95 K were greatly enhanced. This effect can be seen in the temperature programmed desorption (TPD) traces of Xe for purified and unpurified material in Figure 9. The area under the TPD trace is directly proportional to the amount of Xe adsorbed on the SWNTs. After the oxidative treatment, the adsorption capacity of the SWNTs increased by a factor of ~12, while the sticking coefficient

– the probability that an incoming gas phase Xe atom will be adsorbed on the surface – increased by a factor of ~6.

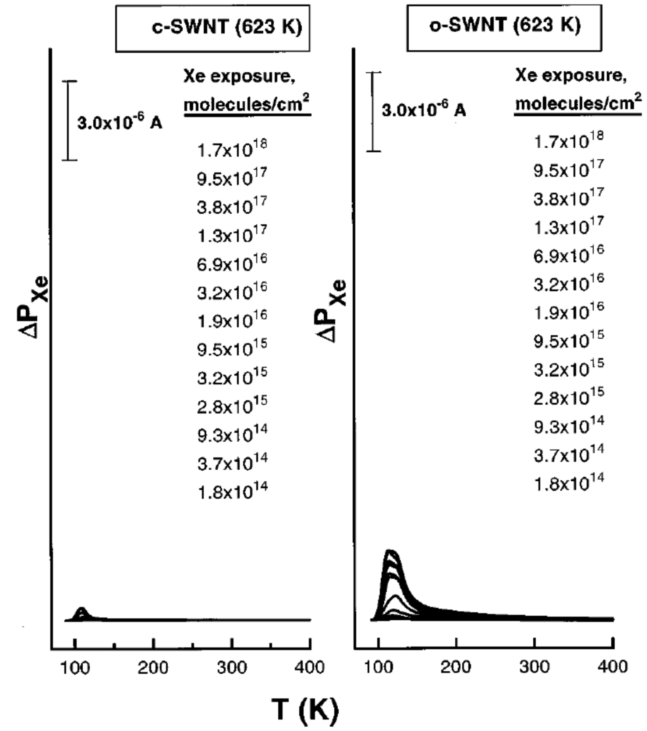

Figure 9. Temperature programmed desorption (TPD) of Xe on closed (c-SWNTs) and chemically opened SWNTs (o-SWNTs). The area of the desorption traces is proportional to the Xe coverage achieved at a given exposure to Xe(g). The capacity is significantly increased by opening the c-SWNTs, as is the initial sticking coefficient (not shown). Reproduced with permission from A. Kuznetsova et al., J. Chem. Phys. 2000, 112, 9590 [54]. Copyright 2000, American Institute of Physics.

Moreover, it was found that heating the chemically etched material to a high temperature (1073 K) increases the capacity and the sticking coefficient even further [54, 56]. Such heating is accompanied by the evolution of CH_4, CO, H_2 and CO_2 gases from the SWNT sample. This implies that there are functional groups on unannealed oxidized SWNTs that somehow block the entry ports created by the oxidative chemical etching. Removing these functional groups through annealing maximizes the adsorptive capacity of SWNTs (Figure 10), leading to an increase in the adsorption capacity by a factor of ~20.

The reason for such a noticeable effect of the chemical groups in question on the interior adsorption appears to be the large magnitude of the dipole moment they possess. Monte Carlo and molecular dynamics modeling of the Xe adsorption process [57] shows that if 1.5-3.0 D dipoles are placed around a wall opening leading into the nanotube interior, the kinetics of adsorption is slowed down. The dipole-induced dipole interactions of the Xe atoms with the functional groups cause clustering of the Xe atoms around the entry and prevent efficient adsorption into the interior.

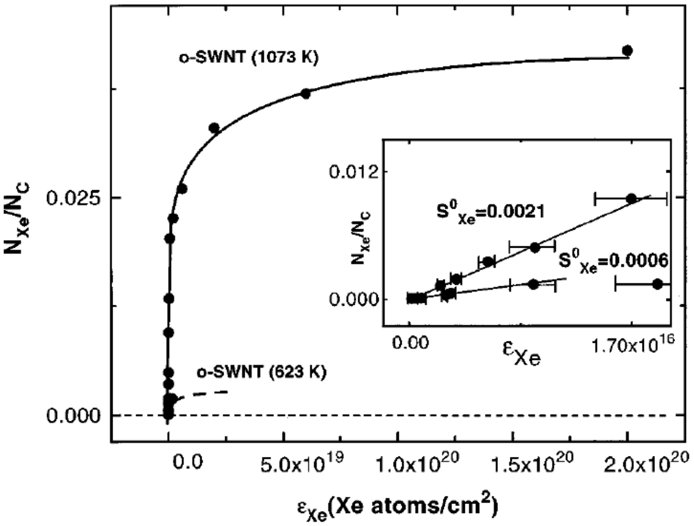

Figure 10. Removing the functional groups from oxidatively etched SWNTs increases the adsorptive capacity by a factor of ~20. The sticking coefficient (inset) is increased by approximately a factor of 3.5. Reproduced with permission from A. Kuznetsova et al., J. Chem. Phys. 2000, 112, 9590 [54]. Copyright 2000, American Institute of Physics.

Evidence for the disappearance of specific functional groups from the SWNTs after heating in vacuum has been obtained by transmission IR spectroscopy. Carbonyl groups and C-O single bonds, as well as –OH groups, were detected by IR spectroscopy on oxidized SWNTs before heating [56]. As the temperature is gradually increased, these groups are destroyed (Figure 11). The presence and decomposition of these groups during heating to 1073 K was also verified with near-edge X-ray absorption fine structure spectroscopy (NEXAFS) [58]. This study enabled the determination of the oxygen-to-carbon ratio, O/C, which was measured to be 5.5-6.7% on the oxidized SWNTs. On the other hand, nanotubes that had not been treated with oxidizing acidic solutions had an O/C ratio of only 1.9%. It was found that the most stable groups containing oxygen involve C-O single bonds. Raman spectral measurements indicated that the carbon bond structure of the nanotubes themselves was not perturbed by the heating, as expected for a highly stable sp^2-hybridized conjugated configuration.

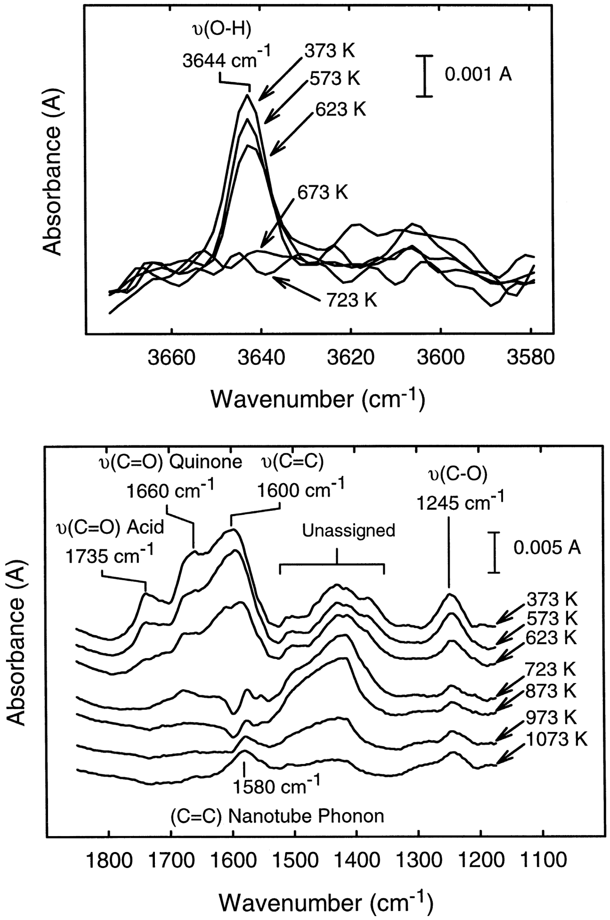

Figure 11. Decomposition of the functional groups introduced onto SWNTs by the oxidizing chemical etching, as observed by transmission IR spectroscopy in vacuum. Carbonyl and ester groups present on SWNTs decompose as the annealing temperature is increased. Reproduced with permission from A. Kuznetsova et al., Chem. Phys. Lett. 2000, 321, 292 [56]. Copyright 2000, Elsevier.

A similar fraction of carbon atoms at defects, ~5%, was found for chemically etched nanotubes in a study where the defect density in the SWNT walls was determined experimentally by titration with a reactive oxidizing molecule, ozone [59, 60]. Ozone readily reacts with carbon atoms at the vacancy defect sites, as well as carbon atoms at the nanotube ends. The reaction with a defect-free nanotube surface should, however, be far slower. By exposing nanotubes to ozone, then heating them to a high temperature (1273 K) to remove the oxygen-containing functional groups, and measuring the amount of carbon in the evolved CO_2 and CO, one can estimate the percentage of carbon atoms located at defect sites. The experiment indicated that 5±2.5% of the carbon atoms are located at defects. This defect density is far greater than the fraction of carbon atoms on the perimeter of the open ends of the nanotubes [59], indicating that reactions with defect sites in the SWNT walls will dominate the etching process either in oxidizing acidic etching solution or in O_3.

Ozone treatment and subsequent annealing to liberate CO and CO_2 were also found to enhance the adsorptive capacity of the SWNTs for Xe. If many successive cycles of treatment with O_3 and annealing to 973 K are carried out, the adsorptive capacity initially increases and then decreases [57]. The increase is explained by ozone expanding the diameter of entry ports already present on the walls of the nanotubes, as well as introducing new ones. After a certain point, however, the loss of carbon through CO and CO_2 formation leads to a reduction in the adsorptive capacity (Figure 12). Through the entire ozone-etching process it is seen that when the SWNT sample is functionalized with oxygen-containing groups, it exhibits a lower adsorption capacity, due to blocking of the entry ports by strongly dipolar oxygen-containing functionalities.

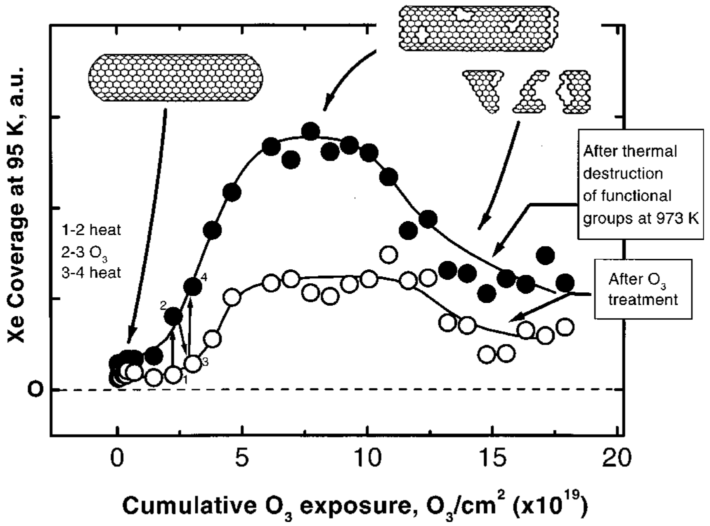

Figure 12. Evolution of the Xe adsorption capacity of SWNTs with successive cycles of O_3 etching and annealing at 973 K. The upper curve corresponds to adsorption capacity after annealing to remove blocking functional groups; the lower curve is the adsorption capacity after treatment with O_3, but before annealing. Reproduced with permission from Kuznetsova et al., J. Chem. Phys. 2001, 115, 6691 [57]. Copyright 2001, American Institute of Physics.

A variety of oxidation methods will result in the opening of the SWNTs. Jakubek and Simard [61] used oxidation in dry air at 475 K in order to open the nanotubes. Similarly to results described above, the surface area increased, and the microporous area approximately tripled after a 2 hour oxidation treatment.

Mechanical ball milling with diamond particles has also been demonstrated to enhance molecular access into the SWNT interior as shown using adsorption isotherm measurements [62-64]. Before the ball-milling procedure, the isotherms of CCl_4 on SWNTs [63] show two steps that the authors attribute to groove and exterior site adsorption. They find that the adsorption energy on the exterior surface is less than the adsorption energy on graphite, in accordance with the intuitive understanding that the convex outer surface provides less coordination for the adsorbed molecules. After the ball milling, an additional step appears in the isotherm at very low partial pressures of CCl_4, corresponding to interior adsorption. It was estimated that the proportion of open tubes after the ball milling was ~30% [62, 64].

Experiments of Matranga and Bockrath [65] as well as those by Lafi et al. [44], emphasize the importance of removing the functional groups from the entry ports into the nanotubes for molecular adsorption. Interestingly, Matranga reports that the controlled introduction of such blocking groups can be also used to lock small quantities of gases (SF_6 and CO_2) in SWNTs. After the functional groups are removed by heating, the gases can be adsorbed in the SWNTs at cryogenic temperatures. If the SWNTs with the molecules adsorbed inside are then treated with ozone, the adsorbed molecules will be prevented from exiting by the added functional groups. The authors report that samples of SWNTs with SF_6 or CO_2 blocked inside are stable in vacuum over periods of 24 hours and can withstand exposure to air.

1.3.3 Changes in the adsorbates due to confinement

Spatial confinement of molecules by their adsorption in SWNTs results in significant changes of their properties compared to the bulk phase. A number of examples have been described by our group as well as by other authors that suggest a possible use of nanotubes as atomic scale templates to produce specific arrangements of matter having special properties.

It has been proposed that adsorption in carbon nanotubes can produce a system where the adsorbate will behave as one-dimensional fluid, both from the classical and quantum points of view [45, 66-68]. Evidence for such one-dimensional behavior was seen experimentally in the adsorption isotherms of Xe and Ar on SWNT bundles [66] and in the heat capacity of ^{4}He adsorbed on SWNTs at 100 mK and 6 K [69].

Theoretical calculations have been reported [70, 71] predicting that He atoms or H_2 molecules will undergo Bose-Einstein condensation when adsorbed in the interstitial channels present in bundles of SWNTs.

When water molecules are confined inside of nanotubes at cryogenic temperatures, a new hydrogen-bonded structure results that has a characteristic infrared signature [72]. MC simulations show that water molecules inside SWNTs form a layered cylindrical structure (Figure 13).

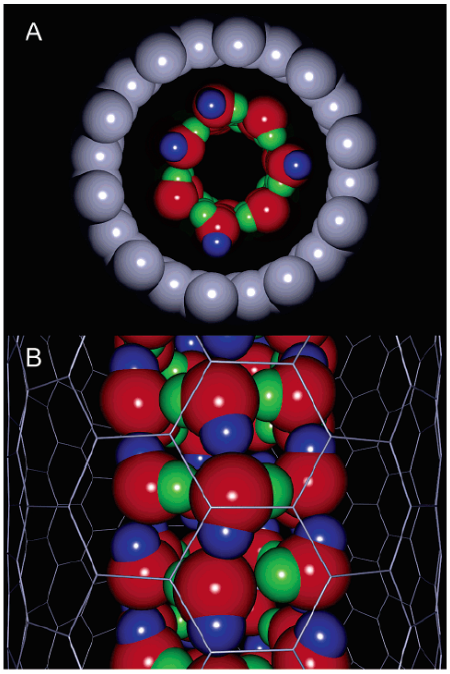

Figure 13. Structure of water inside a (10, 10) SWNTs at 123 K seen in a MC simulation, end view (A) and side view (B). Water molecules form heptagonal rings. Oxygen atoms are shown as red spheres, hydrogens that form inter-ring hydrogen bonds are blue, and those forming intra-ring bonds are green. The mesh structure in part B represents carbon-carbon bonds of the SWNT [72]. Reproduced with permission from O. Byl et al., J. Am. Chem. Soc. 2006, 128, 12090. Copyright 2006, American Chemical Society.

In the case of a (10, 10) nanotube each layer is composed of seven water molecules hydrogen-bonded into a heptagonal ring. More narrow nanotubes produce water rings with a smaller number of water molecules. The hydrogen atoms not taking part in the intra-ring bonding make hydrogen bonds with neighboring rings, as demonstrated in the side view in Figure 13. Such layered structures are stable at temperatures up to 270 K in (10, 10) nanotubes, while for more narrow nanotubes the range of temperature stability is extended even higher.

MD simulations of water in SWNTs were performed to calculate the vibrational frequencies of OH bonds due to intra-ring and inter-ring hydrogens. The simulations indicate that the intra-ring hydrogen bonds are bulk-like, while the inter-ring bonds have a distorted geometry and are weakened as a result. The hydrogen atoms taking part in such weak bonds give rise to a distinct sharp OH stretching mode. This vibrational mode stands out from other OH stretching vibrations that result in a broad peak in experimental IR spectra, as shown in Figure 14. After the water molecules have been deposited on the SWNT surface at 123 K, annealing at 153 K allows the water molecules to diffuse into the SWNTs, leading to the appearance of the mode associated with the inter-ring hydrogen bonds at 3507 cm^{-1}. The interior adsorption of H_2O or N_2 may be effectively blocked using n-nonane [72, 73].

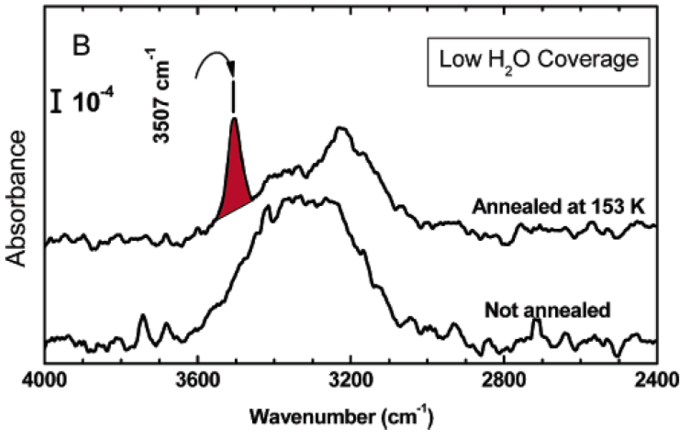

Figure 14. The appearance of the vibrational mode due to water molecules confined in SWNTs in an ordered ring structure. As the SWNTs with water deposited at 123 K are annealed, water molecules migrate into interior sites of SWNTs producing the 3507 cm^{-1} OH stretching mode [72]. Reproduced with permission from O. Byl et al., J. Am. Chem. Soc. 2006, 128, 12090. Copyright 2006, American Chemical Society.

1.4 MOLECULAR TRANSPORT IN NANOTUBES[2]

With a view to an area of application in nanoporous membranes, a number of workers studied diffusion and molecular transport in nanotubes, both experimentally [74-76] and theoretically [77-82].

Theoretical studies show that diffusion inside nanotubes should be rapid at low concentrations of molecules, mainly due to the smoothness of the potential along the nanotube wall, meaning that the diffusing molecule undergoes few scattering events. As the concentration increases, the molecules begin to scatter on each other and the diffusion coefficient decreases [79]. However, there are strong indications that even at high adsorbate density the diffusion of molecules inside SWNTs is significantly faster than in the bulk. As will be described in Chapter 7, even at full loading the self-diffusion coefficient of n-heptane in SWNTs is about a factor of 35 larger than the self-diffusion coefficient in bulk n-heptane at the same temperature [83]. This is the result of molecular ordering of the confined adsorbate in the nanotubes. N-heptane molecules tend to orient themselves parallel to the nanotube axis when they are adsorbed inside SWNTs. This makes translational motion along the nanotube axis less hindered, thus increasing the diffusion coefficient. A similar increase in diffusivity due to the formation of ordered structure is seen in the simulations of N_2 diffusion in SWNTs [77], where an ordered row of molecules is formed in the nanotube center.

When the motion of molecules is concerted rather than random, the smoothness of the potential along the nanotube walls provides a dramatic enhancement of transport properties over

---

[2] This section is reproduced with modifications from a manuscript by P. Kondratyuk and J.T. Yates, Jr., titled "Molecular Views of Physical Adsorption Inside and Outside of Single Wall Carbon Nanotubes", which has been accepted for publication in the Accounts of Chemical Research, published by the American Chemical Society.

those predicted by hydrodynamic flow equations. Majumder et al. [75] measured the flow rates through a membrane composed of aligned multiwall carbon nanotubes for several liquids (water, alkanes and alcohols). The flow rates were found to be four to five orders of magnitude more rapid than the hydrodynamic equations predict. Additionally, the flow rate did not correlate with the viscosity of the liquid. The authors attribute both of these effects to a nearly frictionless nanotube-liquid interface.

2.0 DESIGN AND OPERATION OF THE TPD EXPERIMENTAL APPARATUS[3]

Here the experimental system is described that has been employed for the acquisition of all the temperature programmed desorption (TPD) data presented in this Dissertation. This computer-controlled system has been designed with a view to the acquisition of large amounts of TPD data. The vacuum part of the system consists of a sample mounted on a rotation-translation manipulator, a shielded quadrupole mass spectrometer for the desorption flux measurement, and a collimated molecular beam doser for adsorbate delivery. A typical experiment involves a series of tasks: (1) dosing of the adsorbate onto the surface; (2) calibrating the mass spectrometer gain; (3) translating the dosed sample to the mass spectrometer position by using stepper motors on the rotation-translation manipulator; (4) linearly ramping the temperature of the sample to acquire the desorption spectrum; and (5) cooling the sample. In the system described here, these tasks are accomplished automatically via an attached computer system.

The preparation of an SWNT sample is also described. The results of CCl_4 adsorption on SWNTs are presented as a typical example of the system in operation.

---

[3] This chapter is reproduced with modifications from: P. Kondratyuk, J.T. Yates, Jr.; Design and construction of a semiautomatic temperature programmed desorption apparatus for ultrahigh vacuum. J. Vac. Sci. Technol. A (2005), 23, 215-217.

2.1 BACKGROUND

Temperature programmed desorption (TPD) occupies an important place in the range of techniques employed by surface science [84-86]. While a single TPD spectrum can be used to deduce some information about the adsorbate-surface and adsorbate-adsorbate interactions, usually a series of TPD spectra are acquired for varying gas exposures. In many cases this approach provides information about the kinetics of desorption as a function of coverage, and about the relative sticking coefficient as a function of coverage [87, 88].

Here we show a series of TPD measurements made for CCl_4 adsorption on a 30 μg quantity of single walled carbon nanotubes (SWNTs), supported on a gold surface, which can be heated by contact with two tungsten support wires.

2.2 PARTS OF THE EXPERIMENTAL SYSTEM.

The stainless steel ultrahigh vacuum (UHV) chamber is equipped with a 360 L/s ion pump, a 120 L/s turbomolecular pump and a standard gas handling system. The base pressure after bakeout was 2×10^{-10} Torr. Figure 15 shows the arrangement of components inside the UHV chamber.

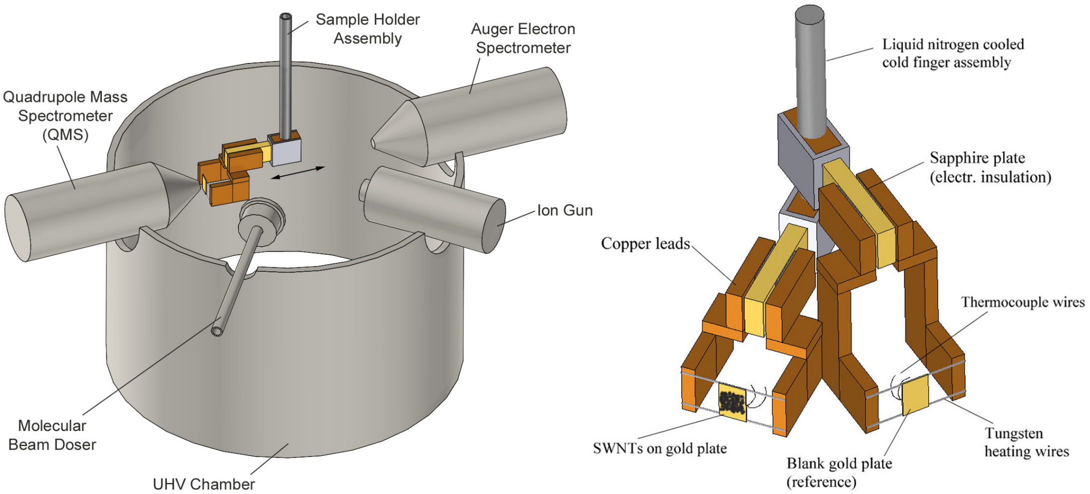

Figure 15. Schematic of the vacuum system. An enlarged view of the sample holder is shown on the right, with both SWNT and reference gold plates. Only one part of the sample holder is shown inside the chamber for clarity.

Dosing of the adsorbate gas onto the sample is achieved by using a molecular beam doser consisting of an absolutely calibrated pinhole conductance that controls the total flux to the surface and a microcapillary array doser head that ensures an even distribution of the adsorbate across the sample [89-91]. By measuring the dependence of pressure on time in the gas line behind the pinhole one can calculate the absolute flux of molecules at the sample, which in the case of CCl_4 was determined to be 8.7×10^{12} molecules $Torr^{-1}$ cm^{-2} s^{-1}.

Figure 15 shows a schematic of the vacuum part of the system. The sample holder assembly, shown on the right in Figure 15, incorporates two 10×14 mm gold plates. One of them is used to support the deposited material (in this case, SWNTs), while the other is used as a reference to monitor the desorption from the gold surface itself. Depending on how the electrical connections are made, either one or the other can be connected to the temperature control circuit. In the following description, whenever the “sample” is mentioned, it is understood that the same can apply to the “reference” plate. The two gold plates are in thermal contact with a liquid N_2 filled cryogenic Dewar via two copper conductors, enabling cooling to about 90 K. They can be ohmically heated to about 1100 K. Their temperatures are measured by a type K thermocouple attached directly to the gold plate.

After dosing of the adsorbate with the molecular beam the sample (or reference) is rotated to the 3.0 mm opening of a shielded quadrupole mass spectrometer (QMS) and the sample temperature is linearly increased. The flux of the desorbing molecules as a function of increasing temperature can then be measured as the output signal of the QMS at a particular m/e ratio. An end cap of the QMS is electrically isolated from the shield and is biased to -100 V to prevent the electrons from the QMS ionization region from reaching the sample.

Two stepper motors (type Nema 23, 1 A current rating) are installed on the manipulator, one on the rotational axis and the other on one of three translational axes (see the arrow showing the direction of movement for the translational axis in Figure 15). The stepper motors allow computer controlled positioning of the sample in front of the QMS or doser. The motors operate as an open loop control system, without position feedback to the computer.

A schematic of the system representing the main functional blocks is given in Figure 16. A computer program on a PC integrates all control functions and acquires all data. It can be written in a variety of programming languages, for instance in LabView, the graphical programming language for laboratory use developed by National Instruments. A data acquisition (DAQ) board installed on the PC (National Instruments PCI-6036E) serves as a digital-to-analog and analog-to-digital converter. The 100 kHz timer function of the DAQ board is also utilized, as it gives a superior time resolution compared to the standard PC timer.

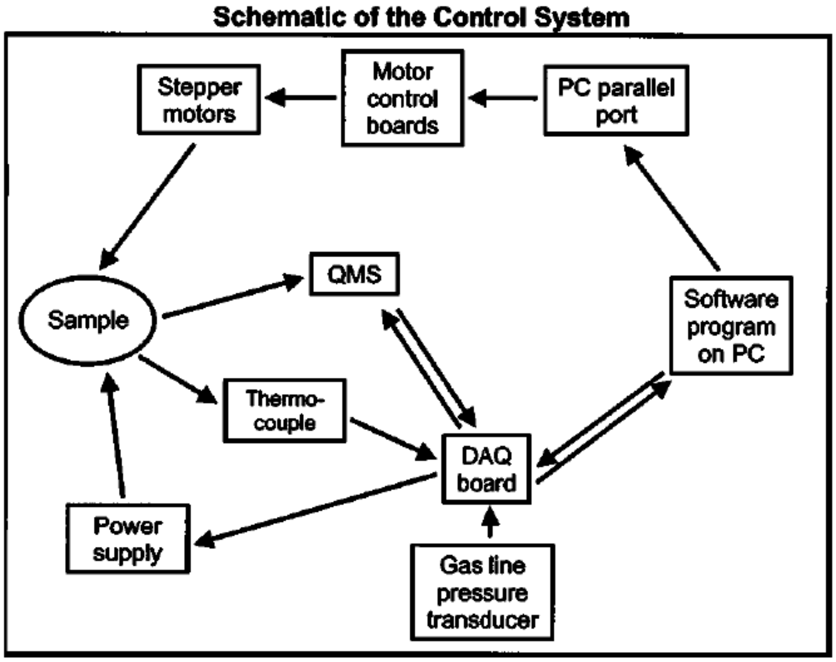

Figure 16. Functional modules of the automatic TPD system and the interrelations between them.

Through the DAQ board the computer controls the power supply that feeds the heating current to the sample. The DAQ board also reads the amplified output of the thermocouple attached to the sample. Temperature control is accomplished as a part of the software program using the PID algorithm [92], which updates the power output ~18 times a second. The operation of the PID temperature control, as implemented here, is described in Appendix B. Temperature stability of around 0.1 K is achieved with this set-up, as well as an excellent linearity during the temperature ramping.

The QMS (UTI 100C) receives the control input from the DAQ board as well, in the form of an analog signal (m/e setting) and digital signal (multiplier sensitivity range). The desorption flux reading recorded by the QMS is then returned to the computer.

The stepper motors are driven by two motor control boards (Motion Group, model MS2.0), which in turn are run through the parallel port of the PC. The motors provide an angular resolution of 1.8^{o}, translating into an angular resolution of 0.045^{o} on the rotational axis of the manipulator when the gear ratios are taken into account. The resolution on the translational axis is in the micrometer range, although lack of precision in the mechanical components probably degrades this resolution somewhat. Such resolution guarantees reproducible positioning of the sample in front of the QMS or doser.

2.3 PREPARATION OF THE NANOTUBE SAMPLE

The single walled nanotube samples were produced by R. Smalley and his collaborators [21, 22] using pulsed laser vaporization. A schematic of the pulsed laser vaporization setup is given in Figure 17.

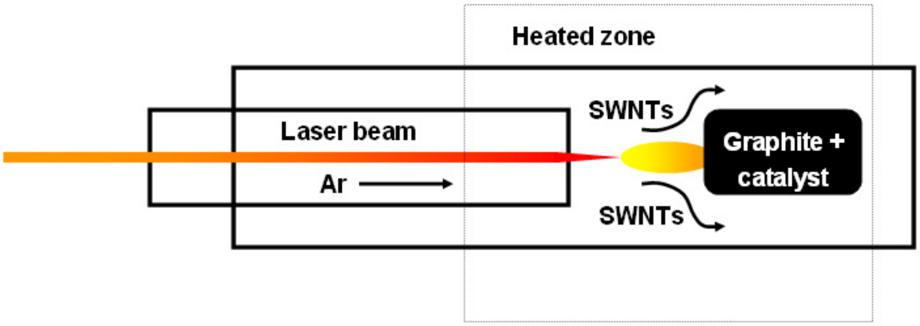

Figure 17. A schematic of an experimental setup for producing SWNTs by pulsed laser vaporization of graphite mixed with a metal catalyst.

In such a setup, the graphite target positioned in the flow of Ar gas is irradiated with a pulsed high-power laser (in [22] the laser operated at 30 Hz with 300 mJ per pulse, 532 nm wavelength). The graphite target contains around 1.2 at. % of a metal catalyst, usually a Ni/Co mixture. The graphite target is placed in an oven so that its temperature can be maintained at around 1300 K. The SWNTs are formed in the plasma plume produced by the laser evaporating the graphite target. They are carried away by the flow of Ar gas and are collected on a water-cooled collector surface. For Ni/Co as the catalyst, the yields of the nanotubes produced (relative to the amount of evaporated carbon) were as high as 70% [22]. The most probable SWNT diameter in the sample was ~13.6 Å.

The as-produced material is contaminated with significant amounts of catalyst impurities and amorphous carbon. They were purified by reflux treatment in aqueous HNO_3, HNO_3/H_2SO_4 and sonicated in H_2O_2/H_2SO_4 following procedures developed by the Smalley group[55]. The oxidizing acids and H_2O_2 primarily attack reactive metal particles and amorphous carbon, leaving the nanotube structure mostly intact. However, the nanotube ends (and to a small degree, walls, possibly at defect sites) are oxidized, leading to the opening and cutting of the SWNTs. The purified nanotubes have a measured most probable length of 320 nm, with a range of lengths up to ~ 1500 nm.

An approximately 36 μg sample of SWNTs was deposited on the Au support plate (area = 1.4 cm^2) in air from a suspension in dimethylformamide (DMF) with a concentration of 12 mg/L. The suspension was placed on the gold support plate kept at a temperature of 50-70° C and the solvent was allowed to evaporate. At this temperature the evaporation proceeds quickly enough to ensure even distribution of SWNTs across the gold support. At lower temperatures agglomeration of the nanotube material may occur. After the sample was placed into the UHV system, it was annealed at 1073 K for 10 min in order to decompose oxygen-containing functionalities that were shown to block molecular access into the SWNT interior [56].

2.4 STAGES OF THE TYPICAL EXPERIMENT.

We employed the set-up described above for the study of CCl_4 adsorbed on single walled carbon nanotubes (SWNTs). The experiment was conducted as follows. First the gas line was filled with the adsorbate gas (CCl_4) to the required pressure and the valves leading to the doser were opened. At this point the gas begins to be dosed into the system and continues to be dosed for the duration of the experiment. A steady, low background pressure exists throughout the experiment, and the molecular beam supplies a high local pressure on axis. The gas is pumped rapidly by the condensation on the cold parts of the Dewar and by the pumps. This ensures that when the sample is not positioned in front of the doser, very little adsorbate is delivered to the surface. We estimate that the amount of the adsorbate that the sample receives in this indirect way during the typical experimental cycle is only 1-2% of what is delivered when the sample is positioned in the molecular beam for dosing.

The parameters of the experiment, such as the temperature ramp rate, the dosing temperature, dosing times etc., are then entered into the computer program and it is started. Figure 18 outlines the steps that the program goes through for a typical TPD experiment. It first moves the sample into the molecular doser beam and waits for the prescribed time to reach the needed exposure.

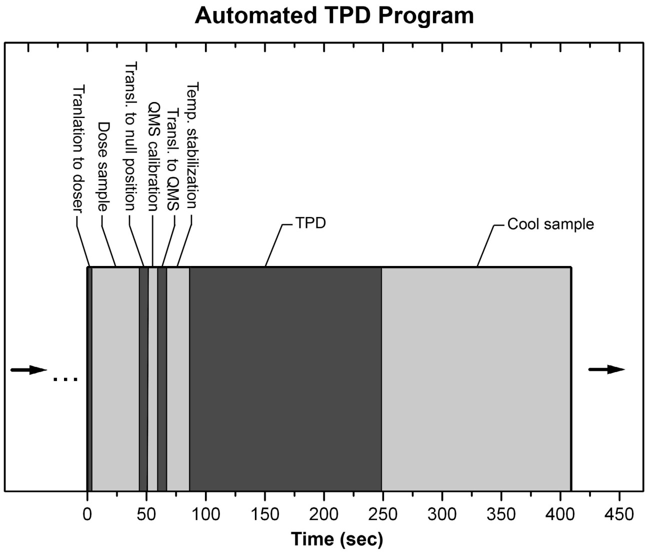

Figure 18. Timing of consecutive steps of the experimental sequence.

In the course of our study it was found that a correction has to be made for a slow variation in the sensitivity of the QMS detector as the sequence of experiments progresses. By modifying the computer program, additional steps were introduced into each TPD experiment to accomplish calibration. They involved a careful measurement of the small background signal generated by the molecular beam doser and subsequent normalization of the TPD spectrum by this value.

Thus after the adsorbate has been delivered to the surface the sample is rotated to the position where no dosing occurs and the routine that calibrates the mass spectrometer sensitivity is executed. The sample is then placed in front of the QMS opening and the TPD spectrum is recorded as the temperature is linearly ramped. When the TPD spectrum has been acquired, the program decreases the heating power fed to the sample and waits for it to reach the dosing temperature again. After this the next cycle of dosing, calibration and obtaining the desorption spectrum is begun.

TPD spectra of CCl_4 adsorbed on the nanotubes are shown in Figure 19 for a range of exposures. A number of overlapping features are observed to develop as the exposure increases.

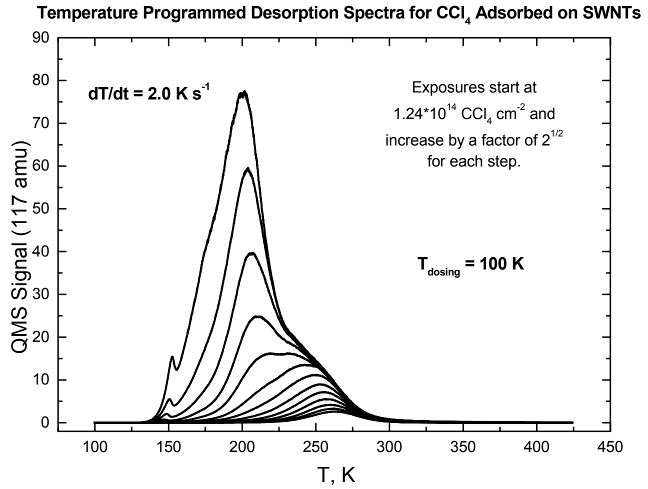

Figure 19. TPD spectra of CCl_4 adsorbed on SWNTs at 100 K for a range of exposures. The development of new features is observed as coverage increases.

The area under the TPD curves is proportional to the amount of adsorbate desorbing from the sample. When the areas from Figure 19 are plotted versus the exposure to the adsorbate (Figure 20), a linear relationship is observed, indicating that CCl_4 adsorption occurs in a reproducible fashion with a constant sticking coefficient.

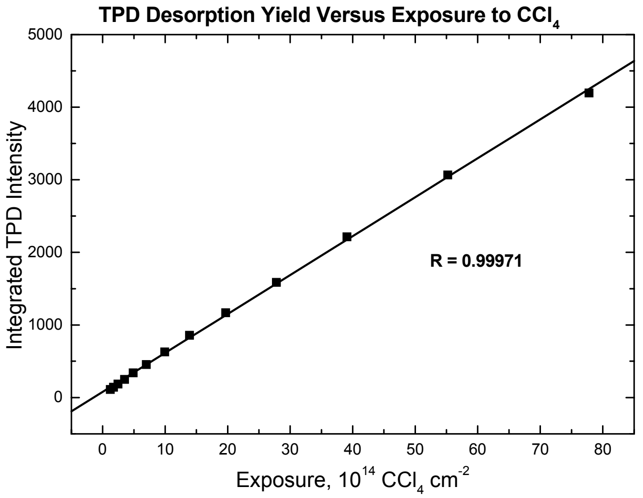

Figure 20. Integrated area under the TPD spectra from Figure 5 versus exposure. The line is the best linear fit to the data.

3.0 PREFERENTIAL ADSORPTION INSIDE NANOTUBES COMPARED TO FLAT SUBSTRATE[4]

It is shown that carbon nanotubes can take up adsorbate from supporting surfaces they are in contact with. This effect is due to stronger binding forces that the molecules experience on the nanotube adsorption sites.

3.1 INTRODUCTION.

Carbon single walled nanotubes (SWNTs) expose adsorption sites with high binding energies for physical adsorption compared to planar surfaces [50, 93]. These sites are the interior nanotube sites as well as the exterior groove sites present at the boundary between adjacent nanotubes. The inner surface of a nanotube, and the groove exterior sites between nanotubes, maximize attractive interactions for adsorbed molecules due to the enhanced surface proximity provided to an adsorbed molecule by the curved nanotube surfaces [45, 94]. By studying a sample of SWNT bundles held by van der Waals forces on a gold support surface, we have directly observed that

---

[4] This chapter is reproduced with modifications from: P. Kondratyuk, J.T. Yates, Jr.; Nanotubes as molecular sponges: the adsorption of CCl_4. Chem. Phys. Lett. (2004), 383, 314-316.

the presence of high binding energy nanotube adsorption sites causes the nanotubes to act as molecular sponges, sweeping up weakly-bound adsorbed species on the gold support surface with high efficiency.

3.2 EXPERIMENTAL METHODS.

The sample of purified and cut SWNTs supported on a Au plate was prepared as described in Section 2.3. Such SWNTs have openings on the walls and at the ends that allow adsorbates to access the nanotube interior. Auger spectroscopy indicates that the Au is covered by a graphite layer which is at least 100 Å thick, as it is able to obliterate completely the underlying Au Auger spectrum. A second blank Au plate with a similar graphite coating was used as a control and contained no SWNTs. A non-uniform deposit of nanotubes on the Au support surface could be seen by the eye, with Au regions visible through the deposit. The two sample plates, mounted on a rotary manipulator, were loaded into an ultrahigh vacuum system which achieved a base pressure of 2×10^{-10} Torr after system bakeout. The sample (and its control) were heated in vacuum to 1073 K to remove the oxidized groups from the nanotubes, opening them for adsorption in their interior [56]. Adsorption of $CCl_4(g)$ onto these samples was achieved at 97 K by using a molecular beam doser which was absolutely calibrated for CCl_4 delivery, providing a flux of CCl_4 to the sample of 8.7×10^{12} molecules Torr^{-1} cm^{-2} s^{-1}. Following delivery of the adsorbate, the samples were rotated to a differentially-pumped quadrupole mass spectrometer with a 3.0 mm diameter gas sampling aperture, accurately located 1 mm from the sample plate as described previously [54]. The samples were heated from 97 K using a linear temperature program of 2.0 K s^{-1} to cause CCl_4 desorption into the mass spectrometer. The CCl_3^+

cracking fragment from the CCl_4 was monitored at 117 a.m.u. The 0.5 mm thickness of the Au support plate, heated by contact with W resistive heater support wires, guarantees that thermal gradients do not occur across the sample. In the case of CCl_4 desorption from the graphite-covered Au, the leading edge of the profile was analyzed to determine the desorption activation energy.

3.3 RESULTS AND DISCUSSION.

Figure 21 shows a comparison between the thermal desorption kinetics of CCl_4 from the graphitized-Au support surface and from the sample containing SWNTs on the Au support in ten experiments where the coverage is systematically increased. In each individual experiment the CCl_4 dose was identical on the SWNT/Au and on the Au control surface. *A dramatic effect is evident, in that the desorption of CCl_4 at about 175 K from the graphitized-Au support is almost completely suppressed when nanotubes are present on the Au surface.*

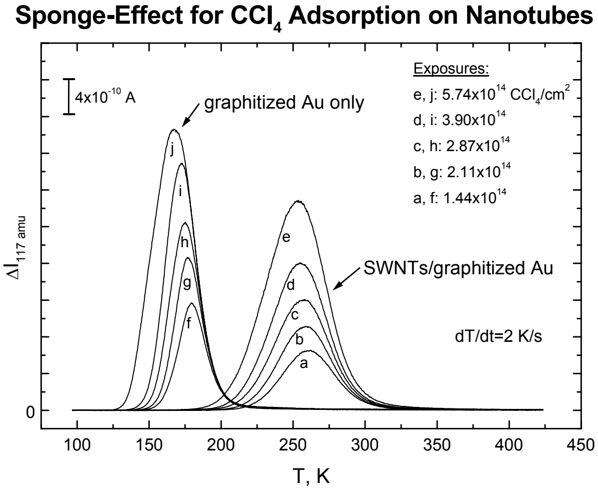

Figure 21. Temperature programmed desorption of CCl_4 from single walled carbon nanotubes on a graphitized-Au support plate, and from a support plate without nanotubes. Desorption from SWNT/Au

occurs at higher temperature than from Au, and the presence of SWNTs on the Au completely suppresses desorption from the Au. The CCl_4 adsorption energy on graphitized-Au as calculated from the leading edge kinetics of trace f is 44.2 kJ mol^{-1}

Figure 22 shows a schematic kinetic picture for the suppression of CCl_4 desorption from the Au when SWNTs are present. An adsorbed CCl_4 molecule migrates laterally on the Au surface until it encounters a deep potential well for adsorption at the nanotube, either at an interior site or at a strong-binding groove site. Thus the nanotubes act as efficient sinks for the mobile CCl_4 molecules. As the temperature is raised above the CCl_4 desorption temperature from Au, CCl_4 desorption begins to occur from the nanotubes, at a temperature near 200 K. The desorption rate from the nanotubes maximizes at about 260 K. At these temperatures, the lifetime for CCl_4 on Au will be very short, and the desorption rate will therefore be governed by the kinetics of desorption from the stronger binding sites on the SWNTs.

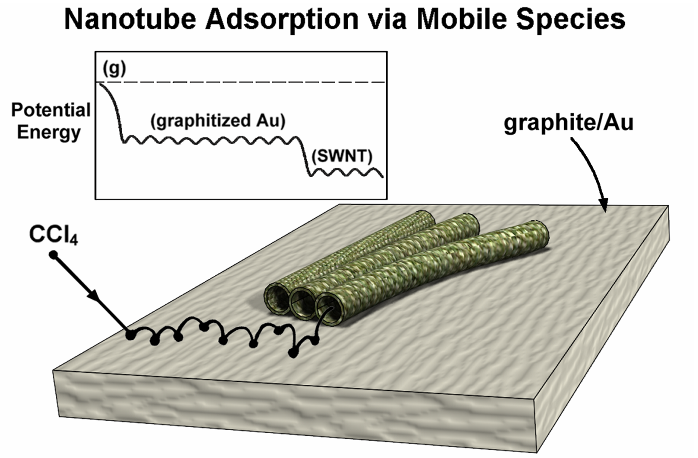

Figure 22. Schematic of adsorption into nanotubes via a mobile species on the graphitized-Au support plate.

A leading edge kinetic analysis of the desorption from the graphitized-Au (trace f in Figure 21) yields an activation energy for first-order CCl_4 desorption of 44.2 kJ mol^{-1} (this value is somewhat higher than 32.6 kJ/mol given by Meyer and Feil [95] for CCl_4 adsorption on Sterling FT graphite at 333 K). With this desorption energy and assuming a standard preexponential factor of 10^{13} s^{-1}, we calculate that the adsorption half-life of CCl_4 on the graphitized-Au surface at 260 K will be only 2×10^{-4} s.

We have not performed a kinetic analysis of CCl_4 desorption from the nanotubes, since the presence of multiple adsorption sites with different energies will compromise an accurate kinetic fit.

Since the *sponge effect* due to the nanotubes is dramatically clear and quantitatively complete, we believe that CCl_4 molecules are able to migrate over macroscopic distances on the Au support before adsorbing at the nanotube sinks which have a total internal and external surface area of the order of 200 times that of the Au support surface. Using an Einstein random walk model, we provide an upper limit estimate for the activation energy for surface migration for CCl_4 on graphitized-Au, as shown below.

Assume that adsorbed CCl_4 migration from the Au surface to the nanotube surface sites begins at a temperature near 150 K, prior to substantial CCl_4 desorption from Au and that migration to the nanotube sites is complete by 200 K, where CCl_4 desorption begins from the SWNTs. At a temperature scan rate of 2 K s^{-1}, this will require 25 s. Assume also that characteristic migration distances of $\sim1\times10^{-3}$ m exist, which is the size of the clean Au regions observed by eye between clusters of SWNTs. Assuming a CCl_4 jump distance, $a = 3\times10^{-10}$ m, a preexponential factor for surface migration of $\nu = 10^{12}$ s^{-1}, and an activation energy for surface migration = E_m, we may write the diffusion coefficient, D, in m^2s^{-1}, as

$$D = a^2\nu \cdot Exp(-E_m / RT) = 9\times10^{-8} \cdot Exp(-E_m / RT). \qquad (1)$$

The rms migration distance, $\langle x \rangle$, for two-dimensional surface migration is

$$\langle x \rangle = (Dt)^{1/2} \cong 1 \times 10^{-3} \quad m \qquad (2)$$

Equations (1) and (2) permit a crude estimate of the order of magnitude of the activation energy for CCl_4 surface migration on graphitized-Au at $E_m \cong 1$ kJ mol^{-1}. This compares with the measured activation energy for CCl_4 desorption from graphite-coated Au of 44.2 kJ mol^{-1}.

3.4 SUMMARY OF RESULTS.

Nanotubes act as molecular sponges for molecules adsorbed on support surfaces in contact with the nanotubes which more weakly bind adsorbed molecules than the nanotubes. Quantitative transfer occurs from the support surface into the nanotubes.

These results corroborate the potential applicability of carbon nanotubes or nanotube-containing materials to the purpose of molecular storage or capture of toxic compounds. The key properties permitting such potential use are high specific surface area and the presence of high binding energy adsorption sites.

4.0 COMPETITION FOR INTERNAL, GROOVE AND EXTERNAL SITES IN COADSORBED N-NONANE AND CARBON TETRACHLORIDE[5]

We show that thermal desorption kinetics clearly resolve adsorbates bound in different sites on single walled carbon nanotube bundles. The molecules n-C_9H_{20} and CCl_4 were compared and it was found that the nanotube internal sites exhibited the highest desorption temperature, whereas external groove sites exhibited the next highest desorption temperature for both molecules. When n-C_9H_{20} and CCl_4 coadsorb, the more strongly bound n-C_9H_{20} quantitatively displaces CCl_4 from internal sites to groove sites. Molecular shape governs the capacity of the different sites for the two molecules.

4.1 INTRODUCTION.

The nature of adsorption sites in and on carbon nanotubes, and how the adsorptive properties of the material can be enhanced by its modification, has been addressed in a number of studies [50, 54, 61, 63, 64, 66, 96-101, and references therein]. The interest in adsorption on nanotubes stems

---

[5] This chapter is reproduced with modifications from: P. Kondratyuk, J.T. Yates, Jr.; Desorption kinetic detection of different adsorption sites on opened carbon single walled nanotubes: the adsorption of n-nonane and CCl_4. Chem. Phys. Lett. (2005), 410, 324-329.

partly from their relative uniformity as compared to such widely used materials as activated carbons, and the fact that the curvature of the nanotube walls results in high binding energy for molecules bound on internal adsorption sites, and in groove sites between adjacent nanotubes [45, 50].

Previous studies in this laboratory [57, 60] showed that etching with O_3 can open both end cap and wall entry ports in closed nanotubes permitting adsorption into the nanotube interior. Vibrational spectroscopy experiments with the simultaneous adsorption of two molecules showed that a more polarizable Xe molecule displaces CF_4 from the interior of the nanotubes [100].

In this chapter we present an investigation of the adsorptive properties of opened single walled carbon nanotubes (o-SWNTs) by temperature programmed desorption (TPD) of two dissimilar molecules, CCl_4 and n-C_9H_{20}. Previously we have shown that TPD is a useful analytical method to observe adsorption in o-SWNTs [54, 102]. While CCl_4 is a compact almost spherical molecule, n-nonane is a long chain alkane that is approximately twice as long as the diameter of a CCl_4 molecule. This difference in molecular shapes leads to interesting configurational effects in the external linear groove sites in SWNT bundles.

4.2 EXPERIMENTAL PROCEDURES.

The single walled carbon nanotubes were produced by R. Smalley and collaborators using the pulsed laser vaporization technique [21, 22]. Purification by HNO_3/H_2SO_4 treatment was employed to remove catalyst particles and graphitic impurities. The purification step also results in chemical cutting and opening of the nanotubes, giving opened SWNTs with a most probable length of 320 nm [55]. Section 2.3 details the preparation and purification of the SWNT sample.

The sample consisting of approximately 36 μg of nanotubes was deposited onto a 0.5 mm thick gold support plate from a suspension in dimethyl formamide. Prior to adsorption the sample is cooled to 100 K (or 120 K, in the case of n-C_9H_{20}) via thermal contact with a liquid nitrogen-filled tube which acts to support the sample holder.

An identical gold plate containing no nanotubes was used as a blank reference to monitor the desorption from the gold itself compared to desorption from the nanotubes. Non-multilayer adsorption on the Au support plate was found to be less than 1% of that observed on the SWNT samples.

Before adsorption experiments the sample and reference plate were annealed at 1073 K to decompose oxygen-containing functional groups that might be present on the nanotubes. Such groups had earlier been shown to prevent transport of the molecules into the interior of the nanotubes [56]. The annealing step also serves to remove adsorbed background gas molecules such as water that might have accumulated on the nanotube material left for extended periods of time in vacuum.

Experiments were performed in an ultrahigh vacuum (UHV) chamber described in Chapter 2, which also discusses the procedure for automated exposure to the adsorbate and acquisition the TPD data. A collimated molecular beam doser with a limiting pinhole conductance [89, 90] was used to deliver the adsorbates to the surface. The delivery rate at the sample surface was 9.6×10^{12} molecules $\mathrm{Torr}^{-1}\ \mathrm{s}^{-1}\ \mathrm{cm}^{-2}$ for n-C_9H_{20} and 8.8×10^{12} molecules $\mathrm{Torr}^{-1}\ \mathrm{s}^{-1}\ \mathrm{cm}^{-2}$ for CCl_4. The limiting doser conductance was absolutely calibrated with CCl_4 and Xe using careful measurements of the rate of depletion of a standard volume.

4.3 RESULTS.

Two types of experiments were carried out. One group of experiments involved probing the desorption kinetics of individual adsorbates as a function of exposure to the gas of interest, while the other focused on coadsorption of n-C_9H_{20} and CCl_4 to observe displacement effects.

Temperature programmed desorption spectra obtained for increasing exposures of both n-C_9H_{20} and CCl_4 are given in Figure 23 and Figure 24 respectively. Here, only one adsorbate is dosed onto the SWNTs.

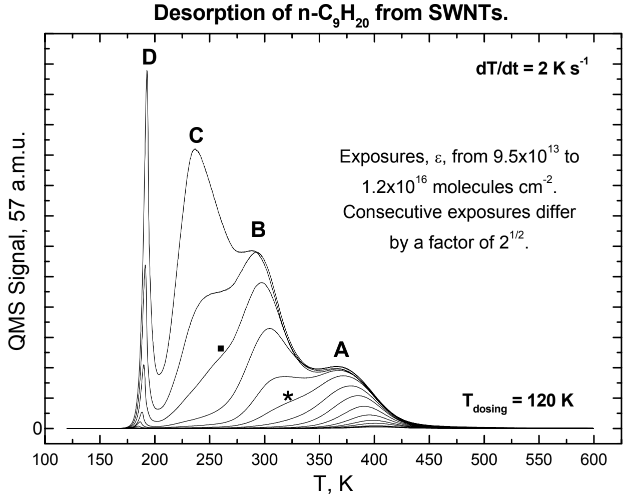

Figure 23. Desorption of n-nonane from nanotubes for a range of exposures. Four resolved spectral features are evident, labeled A, B, C and D. The *- and ▪-labeled traces correspond approximately to the completion of filling of sites which contribute respectively to the A and B desorption processes.

Four overlapping spectral peaks (labeled with letters A to D) can be seen in the nonane desorption spectra, indicating the presence of four accessible environments for adsorbed n-nonane molecules, each desorption process having different characteristic desorption temperatures. As is often the case, at low exposures only the sites with high desorption temperatures are occupied. At higher exposures a sequence of desorption peaks at monotonically decreasing temperatures is observed.

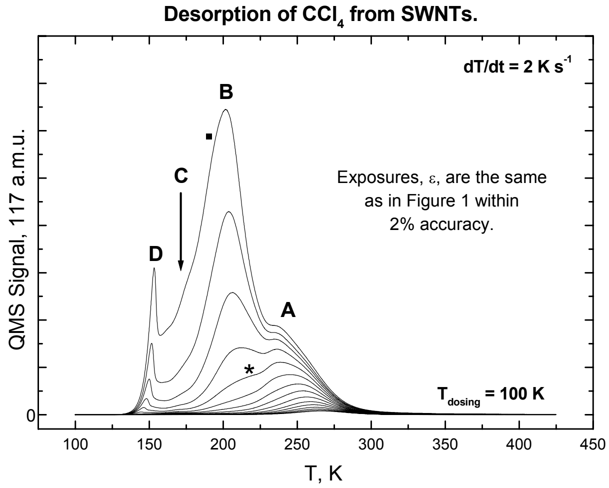

Figure 24. TPD spectra of CCl_4 adsorbed on nanotubes. Three overlapping spectral features can be associated with those observed in nonane desorption, while the fourth, labeled C, only starts to develop at the highest exposure. The *- and ▪-labeled traces correspond approximately to the completion of filling of sites which contribute respectively to the A and B desorption processes.

When the adsorbed molecule is CCl_4 instead of n-C_9H_{20}, three features are visible for the same exposures as in the n-C_9H_{20} experiment. The fourth feature, C, only starts to develop at the highest exposure. All the features from CCl_4 desorption are shifted to lower temperature compared to those from n-C_9H_{20}, probably due to the lower polarizability of the CCl_4 molecule (α = 11.2 Å^3 for CCl_4 compared to 17.4 Å^3 for n-nonane) [103] and consequently lower binding energy on the same adsorption site. The traces for CCl_4 are also less well resolved compared to those of n-C_9H_{20}.

In both cases the feature labeled D is the multilayer, or bulk adsorbate, desorption peak. It is easily identifiable by the characteristic overlap of the leading edges for various coverages, indicative of zero-order kinetics. Since the D feature is caused by the desorption of molecules lying on another layer of identical molecules, it is not characteristic of the adsorption sites present on the nanotubes.

It is worth mentioning that the adsorbate molecules can be expected to eventually find the most energetically favorable unoccupied sites on the surface and desorb from them during the TPD process, even if initially they are adsorbed in a non-equilibrium fashion because of low dosing temperatures. This is due to the fact that the barriers for diffusion between the different sites on the nanotubes are smaller than the barrier to desorption from the surface, and thus the equilibrium on the sample is achieved before the desorption begins. A closely related effect is seen in the coadsorption experiments described below, where it was found that the TPD spectra are identical no matter what the order of dosing of the two adsorbates was. In that case, the equilibrium between two molecules on the surface was reached before the desorption of either molecule could begin.

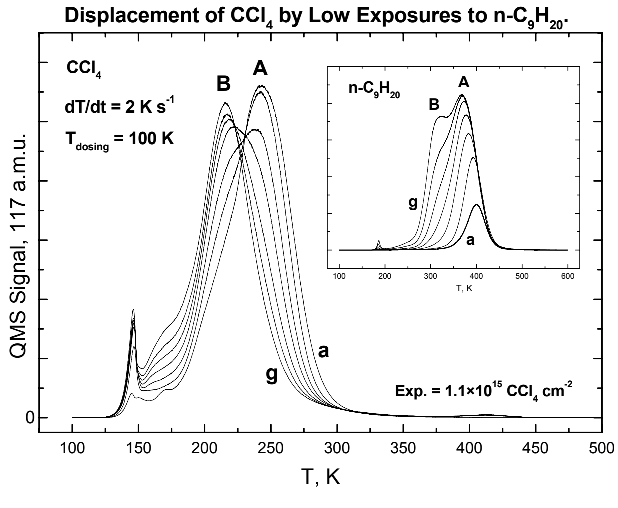

Figure 25. Displacement of CCl_4 (by n-C_9H_{20}) to sites with lower binding energy. Displacement occurs mainly from sites A to B. Inset: corresponding TPD traces of n-nonane. The n-C_9H_{20} exposures are: (a) $\varepsilon = 3.84\times10^{14}$, (b) $\varepsilon = 7.68\times10^{14}$, (c) $\varepsilon = 1.15\times10^{15}$, (d) $\varepsilon = 1.54\times10^{15}$, (e) $\varepsilon = 1.92\times10^{15}$, (f) $\varepsilon = 2.30\times10^{15}$, (g) $\varepsilon = 2.69\times10^{15}$ (all units are molecules cm^{-2}).

The coadsorption experiments allowed us to assign the features A and B in the n-C_9H_{20} and CCl_4 TPD traces to the same types of adsorption sites present on SWNTs. In these experiments the nanotubes were exposed to different amounts of n-C_9H_{20}. Then a constant dose of CCl_4 molecules (1.1×10^{15} molecules cm^{-2}) was delivered to the surface. It was found that as the amount of the more strongly binding n-C_9H_{20} was increased, occupying more and more type A sites, subsequently adsorbed CCl_4 was progressively directed into B type sites, with A type sites remaining filled with n-C_9H_{20}. The displacement of CCl_4 by n-nonane is independent of the order of addition of the adsorbate molecules. This sequential displacement of CCl_4 to B and C desorption processes by n-C_9H_{20} strongly suggests that features A and B correspond to the same nanotube adsorption sites for both CCl_4 and n-C_9H_{20}. The desorption process labeled C for CCl_4 is seen to consist of two close-lying features, while for n-nonane only one feature is present, which likely indicates that the C process for the two molecules originates from different adsorption environments.

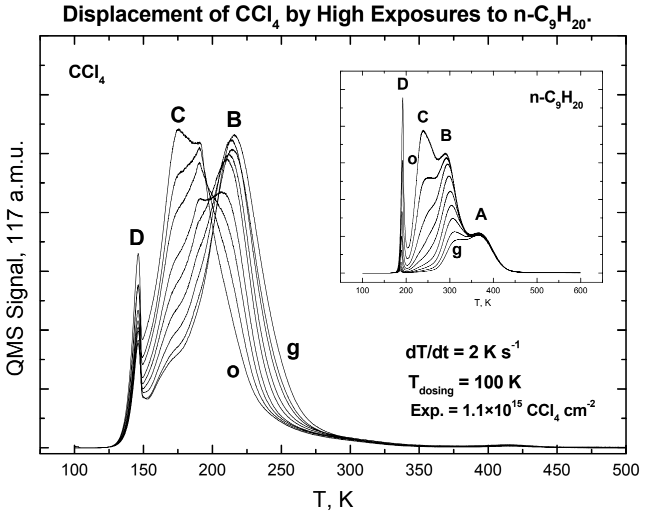

Figure 26. Displacement of CCl_4 with higher exposures of nonane. Sites A are now completely occupied by C_9H_{20}. Displacement occurs from B to C and D. Inset: corresponding TPD traces of nonane. The n-C_9H_{20} exposures are: (g) $\varepsilon = 2.69\times10^{15}$, (h) $\varepsilon = 3.07\times10^{15}$, (i) $\varepsilon = 3.65\times10^{15}$, (j) $\varepsilon = 4.22\times10^{15}$, (k) $\varepsilon = 4.99\times10^{15}$, (l) $\varepsilon = 5.95\times10^{15}$, (m) $\varepsilon = 7.10\times10^{15}$, (n) $\varepsilon = 8.64\times10^{15}$, (o) $\varepsilon = 1.06\times10^{16}$ (all units are molecules cm^{-2}).

TPD spectra of CCl_4 showing the displacement are given in Figures 25 and 26. The insets show TPD traces of nonane for identical dosing conditions. The displacement process in which nonane sequentially pushes CCl_4 from A sites to B sites to C sites continues, even to the stage where multilayer CCl_4 sites are occupied as may be seen by comparing Figure 25 (little D occupancy by CCl_4) to Figure 26 (large D occupancy by CCl_4).

A schematic diagram illustrating the adsorption process observed in this work is given in Figure 27, where the displacement of weakly-bound CCl_4 by more strongly bound n-C_9H_{20} is also shown.

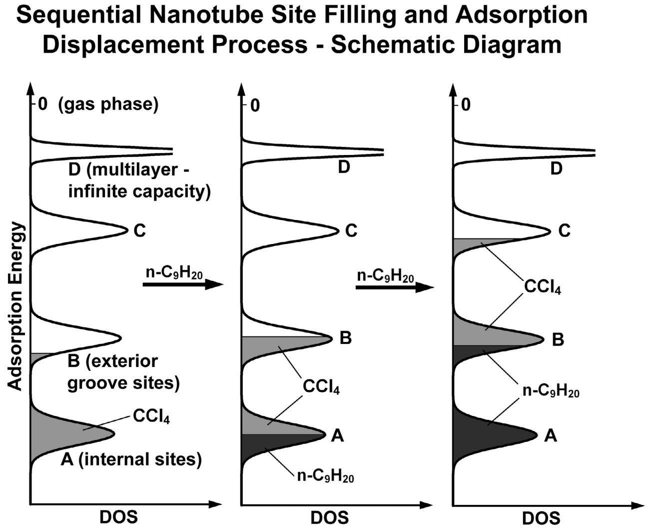

Figure 27. Schematic density of adsorption states (DOS) diagram for o-SWNTs. Addition of n-C_9H_{20} leads to displacement of CCl_4 adsorbed on internal sites to other types of sites (cf. Figures 25, 26).

4.4 DISCUSSION.

A comparison of adsorption traces for CCl_4 and n-C_9H_{20} (Figures 23 and 24) allows an assignment of the sites associated with two highest temperature features A and B in the spectra. Based on relative capacities of the A and B sites toward the two molecules that differ strongly in molecular shapes (to be discussed in more detail below), we assign the feature with the highest desorption temperature, A, to the molecules that are adsorbed inside of nanotubes, and feature B – to the molecules adsorbed in the external groove sites. The groove sites on the outer surface of SWNT bundles are formed by two adjacent nanotubes lying parallel to each other. These sites are known to have a high binding energy [104].

The molar volumes of liquid CCl_4 and n-C_9H_{20} at standard conditions are 0.096 L/mol and 0.178 L/mol respectively [103]. Thus, a n-C_9H_{20} molecule occupies 1.85 times more volume than a CCl_4 molecule in the liquid.

However, when the molecules are adsorbed on site A, the ratio of molar volumes is significantly different from its liquid phase value. We determined this ratio from the exposures to CCl_4 and n-C_9H_{20} needed to completely saturate site A (TPD spectra labeled with asterisks in Figures 23 and 24), assuming a unity sticking coefficient. The corresponding exposures are 2.98×10^{15} CCl_4 cm^{-2} and 2.15×10^{15} n-C_9H_{20} cm^{-2}, giving a ratio of 1.39. This deviation from the value for liquids, 1.85, means that the adsorbed CCl_4 molecules occupy adsorption space *less efficiently* than in the liquid phase, relative to the corresponding values for n-C_9H_{20}.

This less efficient occupation of space by CCl_4 can be explained from considerations of molecular packing if the A site is assigned as the interior nanotube volume. It is known [105, 106] that even the most efficient packing of spheres in a hollow cylinder only fills a small percentage of space when the diameter of the spheres is ~50-70% of the cylinder diameter. This situation corresponds closely to the packing of CCl_4, that has van der Waals diameter of 6.08 Å, in nanotubes, which in our case have an accessible interior diameter of ~10.2 Å. However, relatively thin nonane molecules, with a cross-section of around 3.4 Å, can occupy even the confined interior space relatively efficiently.

A similar analysis can be performed for the filling of sites B by the two molecules. The dark squares in Figures 23 and 24 indicate TPD traces assigned to the completion of filling of sites B for n-C_9H_{20} and CCl_4. For each molecule, the *difference* in exposures between the complete filling of sites A and complete filling of sites B is proportional to the number of molecules adsorbed on sites B. The difference in the exposures for CCl_4 and n-C_9H_{20} needed to completely fill site B be can also be qualitatively observed by comparing the areas under the B features in Figures 23 and 24 where the mass spectrometer sensitivity scale has been adjusted to make the areas of the A adsorption traces approximately the same for n-C_9H_{20} and CCl_4. The ratio of the number of CCl_4 molecules required to fill sites B to the required number of nonane molecules is 8.85×10^{15} CCl_4 cm^{-2} / 3.83×10^{15} C_9H_{20} cm^{-2} = 2.31. This means that n-C_9H_{20} molecules take up significantly ***more*** adsorption space on site B, opposite to the case of internal sites A. This suggests that the ***length*** of the molecule is the determining factor in the population of the B site by molecules, as the linear lengths of the molecules are significantly different, 12.4 Å for nonane versus 6.08 Å for CCl_4. This indicates that site B is a one-dimensional structure where molecules are arranged along the length of the site. A logical choice for such an adsorption site is the groove site on the outer surface of the nanotube bundle.

We ascribe feature C to the adsorption on the exterior nanotube surface. The molecular simulations that served as a basis for this assignment are described in Chapter 5.

4.5 SUMMARY.

In conclusion, the following features for the adsorption of two dissimilar molecules, n-nonane and CCl_4, on opened-SWNTs have been discovered:

1. Internal single walled nanotube adsorption sites, having the highest binding energy for adsorbates, fill first for both n-nonane and CCl_4.
2. Groove sites fill in the second stage of adsorption of n-nonane and CCl_4.
3. The n-nonane molecule quantitatively displaces CCl_4 from internal sites to groove sites due to its higher polarizability (and enthalpy of adsorption), compared to CCl_4.

4. It has been shown that a logical filling of the various adsorption sites present on SWNTs in accordance with adsorption energies is observed in the sequence of desorption kinetic processes found at increasing coverages. This ladder of adsorption energy levels is also seen in the displacement of a weakly-bound molecule by a more strongly-bound molecule.
5. Molecular packing effects have been observed to directly influence the adsorption capacities of the nanotube interior and groove sites.

5.0 MOLECULAR PACKING OF ADSORBATES IN THE NANOTUBE INTERIOR AND GROOVE SITES[6]

Three well defined adsorption sites have been found on opened single wall carbon nanotubes by temperature programmed desorption measurements for several alkanes. A series of linear chain alkanes from pentane to nonane, as well as a branched alkane molecule, 2,2,4-trimethylpentane, were used to elucidate the effect of molecular length on the capacity of the adsorption sites. The two highest energy adsorption sites were assigned as the nanotube interior sites and groove sites on the outside of the nanotube bundles. Hybrid Monte Carlo simulations were performed to probe the molecular-level details of adsorption. Both in experiments and in the simulation, the groove sites were seen to behave as one-dimensional adsorption space, demonstrating an inverse dependence of capacity on the length of the adsorbed molecule. In contrast, the capacity of the internal sites was found to depend inversely on the volume occupied by the molecule.

---

[6] This chapter is reproduced with modifications from: P. Kondratyuk, Y. Wang, J.K. Johnson, J.T. Yates, Jr.; Observation of a one-dimensional adsorption site on carbon nanotubes: adsorption of alkanes of different molecular lengths. J. Phys. Chem. B (2005), 109, 20999-21005. The theoretical calculations of adsorption on SWNTs were carried out by Y. Wang and J.K. Johnson.

5.1 INTRODUCTION.

Single wall carbon nanotubes (SWNTs) have attracted significant scientific interest as adsorption media since their discovery. They are known to have high binding energy adsorption sites in the interior as well as in the grooves between adjacent nanotubes on the outside surface of SWNT bundles [45, 50]. The high binding energies for physically adsorbed molecules inside of nanotubes and on groove sites, as compared to planar graphene sheets, stem from strong van der Waals interactions caused by the proximity of the curved nanotube walls to the adsorbate molecules in those adsorption sites.

Molecular adsorption in the interior, in the groove sites, and on the exterior surface of the nanotubes has been observed in a number of studies employing various experimental techniques [54, 61, 63, 66, 96, 100, 107, 108]. In the case of interior sites, an oxidative treatment followed by annealing in vacuum is usually required to produce entry ports that allow the adsorbate molecules to access the nanotube interior [56]. Such entry ports can be created during the oxidative-acid purification of the nanotubes to remove graphitic impurities after synthesis. Oxidative treatment with gaseous O_3 followed by annealing at 1073 K has also been shown to strongly enhance adsorption kinetics into the nanotube interior by introducing additional entry ports on the nanotube walls [57, 60].

Here we present a combined experimental and simulational study of the adsorption of five linear alkanes, n-pentane to n-nonane, and a branched alkane molecule, 2,2,4-trimethylpentane, on SWNT adsorption sites.

Adsorption of alkane molecules of different molecular length and shape on zeolites has been extensively studied [109-113]. It was found that generally the adsorption capacity depended inversely on the size of the molecule. However this effect was masked by the structural peculiarities of zeolite adsorption sites, especially for shorter alkanes. In the case of carbon nanotubes the adsorption space contains no charge centers and is more uniform at the atomic scale. Thus a smoother dependence of adsorption capacity on molecular length was to be expected for the molecules we studied, as was observed.

In this work, temperature programmed desorption (TPD) is the experimental tool used to characterize the adsorption of these six alkanes. Hybrid Monte Carlo simulations were also used to theoretically probe the molecular-level details of alkanes adsorbed on different sites on the SWNT bundles. As these molecules are chemically very similar and differ only in carbon chain length (linear alkanes) or chain connectivity (2,2,4-trimethylpentane), observing the capacities of different SWNT adsorption sites toward them allowed us to extract information about the density of molecular packing in these sites as well as effects of the adsorption site geometry.

5.2 EXPERIMENTAL METHODS.

Temperature programmed desorption experiments were performed in an ultrahigh vacuum (UHV) chamber described in Chapter 2. The system achieved a base pressure of 2.5×10^{-10} Torr after bakeout.

The SWNTs used in the current experiments were produced by R. Smalley and collaborators using pulsed laser vaporization of graphite with a Ni-Co catalyst [21, 22]. Section 2.3 deals with the synthesis and purification of the SWNTs in more detail. The nanotube sample employed here has been extensively studied before [100, 101, 102, 114].

The sample weighing approximately 36 μg was deposited in air from a suspension in dimethyl formamide onto a gold plate.

An identical gold plate containing no nanotubes was used as a reference to observe the adsorption on the support plate itself. Due to the much larger surface area that SWNTs provide for the adsorbate, the maximum non-multilayer adsorption on the support plate comprised less than 1% of the amount of molecules adsorbed on the SWNTs.

The sample was annealed at 1073 K for 10 minutes before every set of experiments in order to decompose oxygen-containing functionalities that might have been present on the nanotubes. Functional groups at SWNT entry ports have earlier been found to prevent molecular access into the interior of the nanotubes [56].

Adsorbate delivery to the surface was accomplished by means of a collimated molecular beam doser with a limiting pinhole conductance [89, 115]. The limiting conductance was absolutely calibrated using Xe and CCl_4 effusion and found to scale inversely as the square root of molecular weight, as predicted by the classical effusion equation which describes effusion leak rate for an ideal gas. The effusion rates for all alkanes were thus recalculated using the inverse square root of mass law from the CCl_4 value. For n-pentane the dosing rate at the sample surface was calculated to be 1.27×10^{13} C_5H_{12} molecule $Torr^{-1}$ s^{-1} cm^{-2}.

All the data in this work was acquired with a semi-automatic computer controlled system built earlier specifically for large numbers of closely controlled temperature programmed desorption experiments. This system integrates the functions of sample translation between doser and QMS positions, temperature control and QMS signal recording. Its construction and operation are explained in detail in Chapter 2.

After each temperature programmed desorption experiment an additional experiment that served to calibrate the sensitivity scale was carried out with the same adsorbate molecule. In the calibration a TPD desorption profile of a standard amount of the adsorbate (exposure=2.0×10^{15}

molecules cm^{-2}) was taken. The preceding TPD profile was then divided by the integrated intensity of the calibration measurement and multiplied by the number of molecules in the calibration exposure. This calibration procedure served a double purpose. First, it corrected for the slow sensitivity drift in the mass spectrometer due to sensitivity changes in the electron multiplier. Secondly, it allowed a direct comparison of TPD spectra between different adsorbate molecules to be made, because after this procedure the TPD profile reflected a physically relevant measure of the desorption rate, in molecules cm^{-2} K^{-1}.

This desorption rate is connected to the conventional kinetic rate, in molecules cm^{-2} s^{-1}, by the temperature increase rate, dT/dt, during the desorption experiment. The temperature of the calibration exposure was always chosen to be low enough to ensure a unity sticking coefficient.

5.3 THEORETICAL METHODS.

We used the hybrid Monte Carlo (HMC) method [116] to perform the simulations on the nanotubes/alkane system. The HMC technique is reported to be more efficient than either MD or simple MC for simulating long-chain molecules [117, 118]. The multiple-time-step method [119] was used to integrate the intra-molecular degrees of freedom. The nanotube bundle used in the simulations consisted of two (10,10) nanotubes, each containing 20 unit cells (length 49 Å). The gap between the walls of the adjacent tubes was set to 3.2 Å. We chose this “minimal” SWNT bundle to reduce computational demands. The nanotube bundle was placed in the center of a cubic simulation cell 200 Å on a side. Periodic boundary conditions were applied in all three directions. Adsorption of alkanes on the interior, groove, and outside sites was studied. Real SWNT bundles will also have interstitial sites [46]; we have not considered these sites in this work, since we expect that the contribution due to interstitial adsorption to be negligible due to the large size of the alkane molecules. We used an atom-explicit model for nanotubes, taking the Lennard-Jones parameters for graphite (σ = 3.4 Å, ε = 28.0 K) [120] for the nanotube carbons. We used the transferable potentials for the phase equilibria (TraPPE) [121, 122] united atom model for alkane molecules. The alkane-alkane potential is divided into non-bonded (eq 1), bond stretching (eq 2), bond bending (eq 3) and torsion terms (eq 4) as follows

$$u(r_{ij}) = 4\varepsilon_{ij}\left[\left(\frac{\sigma_{ij}}{r_{ij}}\right)^{12} - \left(\frac{\sigma_{ij}}{r_{ij}}\right)^{6}\right] \qquad \textbf{(1)}$$

$$u_{stretch} = \frac{1}{2}k_r\left(r - r_0\right)^2 \qquad \textbf{(2)}$$

$$u_{bend} = \frac{1}{2}k_\theta\left(\theta - \theta_0\right)^2 \qquad \textbf{(3)}$$

$$u_{tors} = c_0 + c_1\left[1 + \cos\phi\right] + c_2\left[1 - \cos(2\phi)\right] + c_3\left[1 + \cos(3\phi)\right] \qquad \textbf{(4)}$$

We used standard Lorentz-Berthlot combining rules to calculate σ_{ij} and ε_{ij},

$$\sigma_{ij} = \frac{1}{2}\left(\sigma_{ii} + \sigma_{jj}\right) \qquad \textbf{(5)}$$

$$\varepsilon_{ij} = \sqrt{\varepsilon_{ii}\varepsilon_{jj}} \qquad \textbf{(6)}$$

The potential parameters used are given in Table 1 and Table 2. The TraPPE model defines a united atom segment as a single CH_3, CH_2, CH, or C group.

Table 1. Lennard-Jones Parameters for TraPPE-UA Field for normal alkanes.

Pseudo-atom	ε/k$_B$ [K]	σ [Å]
CH_4	148	3.73
CH_3	98	3.75
CH_2	46	3.95
CH	10	4.68
C	0.5	6.4

We have calculated the number of segments of molecules adsorbed on the inside, groove, and outside sites. A segment is identified as being inside a nanotube if its (*x,y*) coordinates lie within the radius of either of the nanotubes (the area inside the solid circles representing the nanotubes in Figure 28) and the *z* coordinate lies in the range covered by the extent of the nanotubes in the simulation box. The *z* axis coincides with the nanotube axis in our simulation cell. Segments are identified as being in the groove site if they lie within a cylinder of radius 2.90 Å centered in the nanotube groove sites (dashed circles in Figure 28). The center of the groove site cylinders are located a distance of 9.68 Å from the center of the nanotubes, on a vector directed 30º above and below the plane containing the nanotubes (see Figure 28). A segment is identified as adsorbed on the exterior sites of the nanotubes if it lies within an annular region defined by the radii 6.78 and 11.88 Å from the nanotube centers, and if the segment is not within the groove sites. The outside adsorption sites are schematically shown as the gray shaded region in Figure 28. All other segments that do not lie within one of these three sites are identified as being in the multilayer or the gas phase.

Table 2. Bonded Parameters for the TraPPE-UA Force Field for normal alkanes.

Stretch	**r_0 [Å]**		**k_r/k_B [K]**	
CH_x-CH_y	1.54		130924.4893[*]	
bend	**θ_0**		**k_θ/k_B [K]**	
CH_x-(CH_2)-CH_y	114		62 500	
CH_x-(CH)-CH_y	112		62 500	
CH_x-(C)-CH_y	109.47		62 500	
torsion	**c_0/k_B [K]**	**c_1/k_B [K]**	**c_2/k_B [K]**	**c_3/k_B [K]**
CH_x-(CH_2)-(CH_2)-CH_y	0	335.03	-68.19	791.32
CH_x-(CH_2)-(CH)-CH_y	-251.06	428.73	-111.85	441.27
CH_x-(CH_2)-(C)-CH_y	0	0	0	461.29
CH_x-(CH)-(CH)-CH_y	-251.06	428.73	-111.85	441.27

[*] **This parameter is from OPLS-UA force field**

We have performed two types of simulations, namely NVT and modified grand canonical Monte Carlo simulations for various nanotubes/alkane systems. The NVT simulations were used to find the coverages of molecules in the different bundle sites for each of the alkanes. The initial states for the NVT simulations were prepared by exposing the nanotube bundle to two liquid-like drops of alkane molecules, one at each end of the bundle. The molecules then occupied the interior, groove, external, multilayer sites, depending on the total number of molecules and the temperature. The liquid droplets were prepared from an isobaric-isothermal simulation of pure alkane molecules at 313.15 K and 60.0 MPa, where the starting configuration was a gas phase; the very high pressure was used to quickly reach a liquid-like density. The equilibration period was typically 200,000-400,000 HMC steps, where each step consisted of five MD long time steps followed by a HMC acceptance or rejection move. A typical value for the long time step in the MD run was around 15 fs. Five inner (short) time steps were taken for each long time step. The modified grand canonical ensemble simulations were designed to mimic the process of the TPD experiments and therefore we did not simulate a proper grand canonical ensemble. A typical TPD experiment is carried out by first dosing a system with a known amount of alkane. Then the system is heated and material desorbs into the vacuum with pressures on the order of 10^{-4} Pa; molecules that desorb are pumped away so fast that no readsorption can take place. We have mimicked this process by starting from a pentane-saturated nanotube bundle, obtained through the first type of simulation, followed by grand canonical-type moves to delete the pentane at a pressure of 10^{-4} Pa. No attempt to create adsorbed molecules was made. Obviously, the equilibrium state for this type of simulation is a system with no adsorbed molecules. We are therefore not interested in the limiting distribution of this type of simulation. We use these modified grand canonical simulations to probe, in an approximate way, the rate of desorption for pentane from each of the different sites on a SWNT bundle.

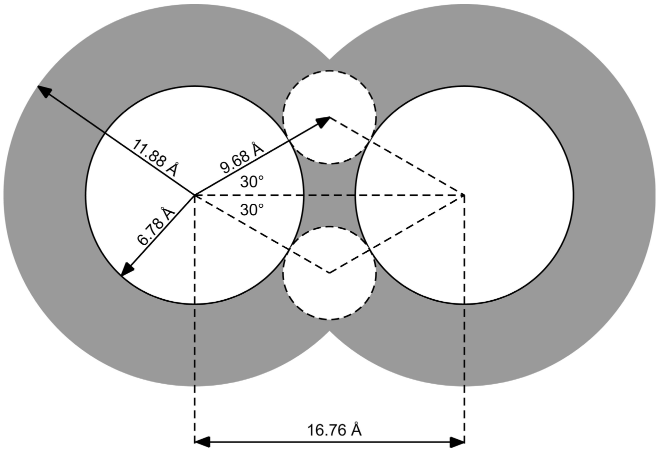

Figure 28. Schematic showing interior, groove and exterior sites of a nanotube bundle.

5.4 RESULTS AND DISCUSSION.

5.4.1 Temperature programmed desorption experiments.

As has been shown before [114], alkane molecules can be adsorbed in four distinct environments on single wall carbon nanotubes, resulting in four resolved features in temperature desorption spectra. Figure 29 shows the representative temperature programmed desorption (TPD) traces from three alkanes – pentane, n-nonane and 2,2,4-trimethylpentane.

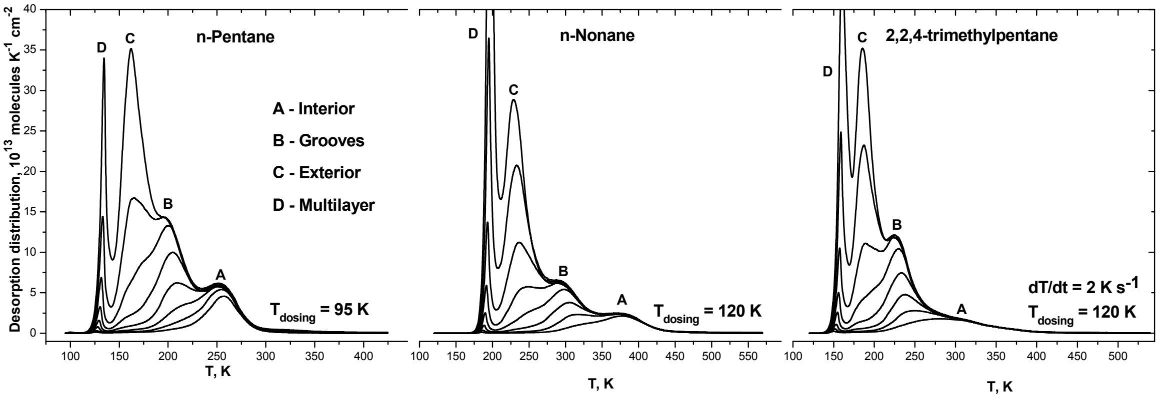

Figure 29. TPD spectra of n-pentane, n-nonane and 2,2,4-trimethylpentane on SWNTs. Exposures are the same for all three compounds. They start at 2.16×10^{15} molecules cm^{-2} and increase in steps by a factor of $2^{1/2}$.

The n-pentane and n-nonane spectra look qualitatively very similar, displaying four prominent features, labeled with letters A to D, that correspond to four different adsorption environments with certain adsorption energies and entropies. TPD spectra of other linear alkanes (n-hexane, n-heptane and n-octane, not shown) present similar spectra, with the difference being the position and relative intensities of the four peaks as is seen also for n-pentane and n-nonane.

Peak D can be easily identified. The overlapping leading edges of the D peaks in these spectra facilitate their assignment as multilayer peaks. They result from the desorption of bulk-like adsorbate that forms on the SWNTs at high exposures to the hydrocarbon molecules and are not characteristic of nanotube adsorption sites. At the same time, none of the A, B or C features are present on the blank gold reference, meaning that these features originate from the adsorbate bound on the nanotubes. Thus, in the following we will limit our discussion to the A, B and C desorption features.

It can be seen that for all three adsorbates features A and B are saturated at the highest exposures shown in Figure 29, while C continues to grow. Consequently, this exposure range should allow the determination of the capacities for sites A and B.

Based on the results of the molecular simulations of the TPD process, as well as capacities of sites A and B toward molecules with different molecular lengths, we assign process A as desorption from the nanotube interior site. We assign process B as desorption from the grooves on the outside of SWNT bundles. We assign process C as desorption from the exterior nanotube surface.

5.4.2 Simulation of the TPD process.

Modified grand canonical simulations for the pentane/nanotube system were carried out at various temperatures, from 125 K to 350 K. The data after 5000 attempted Monte Carlo moves for each temperature are plotted in Figure 30. The starting state was chosen from the HMC simulations of the nanotube/pentane system at 125 K. The relationship between the number of pentane molecules deleted from the system for a fixed number of MC steps and temperature is related to the desorption rates deduced from TPD experiments. Both the experiments and simulations are driven by entropic and energetic considerations. Therefore, we believe the simulations provide information that can be useful for comparing with the TPD experiments. However, the simulations do not have a real time scale. If the simulations were run for a very large number of attempted moves then all the molecules would be deleted at any temperature.

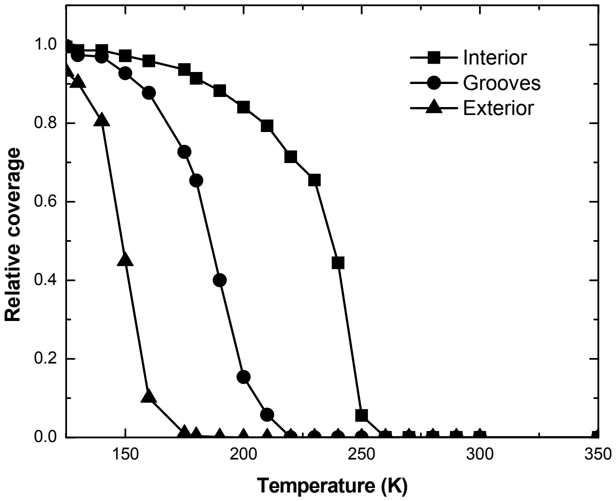

Figure 30. Simulated TPD-like spectra (pseudo-desorption-rates) computed from molecular modeling.

The relative changes in coverage on each of the three sites (interior, groove and exterior) as a function of temperature are plotted in Figure 30. The coverages are normalized by the initial number of molecules on each of the sites. From Figure 30 we see that n-pentane molecules on the exterior sites desorb more readily than molecules on the groove and interior sites. This is true for all temperatures. Moreover, n-pentane is completely depleted on the external sites at the lowest temperature (~175 K), the groove site is depleted at the next lowest temperature (~220 K) and the internal sites are depleted at the highest temperature (~270 K). These temperature trends are in qualitative agreement with the TPD data and corroborate that peak A corresponds to the internal sites, peak B to the groove sites, and peak C to the external sites of the nanotube bundles. Derivatives of the curves in Figure 30 would lead to TPD-like plots from the simulations. However, the statistical noise in the data does not justify taking the derivatives. Moreover, because there is no actual time scale, the MC data only give "pseudo-TPD" data.

The choice of plotting the results after 5000 MC steps is arbitrary. We have also examined the simulations at 1500 and 10000 steps. The lines shift to the right (to higher temperatures) for 1500 steps and to the left (to lower temperatures) at 10000 steps. However, in both cases the same general shape as seen in Figure 30 is observed. Thus, the temperature scale is somewhat arbitrary, since it depends on the number of MC steps chosen. Hence, the simulation data cannot be directly mapped onto experimental TPD data and are best termed “pseudo-TPD” data, as noted above.

5.4.3 Measuring adsorption site capacities.

We have shown earlier [114] that in the case of a CCl_4 molecule, rather dissimilar from a normal alkane, A, B, and C desorption processes are also observed. Displacement experiments involving simultaneous adsorption of CCl_4 and n-nonane showed that the features A and B, and possibly C, correspond to the same adsorption sites on nanotubes in the case of these two very dissimilar molecules. As the alkanes, which are the focus of the current study, are much more similar to each other in their adsorptive properties than n-nonane and CCl_4, it can be concluded with a very high degree of certainty that different alkanes occupy the same three adsorption sites on the SWNT surface, and that desorption processes A, B and C are sampling the same sites for different hydrocarbons.

Due to the use of the normalization procedure described in the experimental section, the areas under individual features accurately reflect the amount of adsorbate found on that site. Additionally, the areas under the TPD features can be compared directly for different molecules. In order to estimate the number of adsorbate molecules on adsorption sites A and B, the areas under these two peaks must be found. This task presents challenges, as a significant overlap of different peaks prohibits separation and straightforward integration. Modeling of the spectra as a sum of first order desorption processes is also problematic due to the apparent shift of the peak positions to lower temperatures with increasing coverage, an effect not accounted for by the first-order kinetics.

In order to circumvent this difficulty in measuring the areas of desorption features A and B, we conducted a series of experiments where the dosing temperature of the alkanes was varied around the onset temperature of the two peaks instead of dosing at a low temperature where all molecules would be adsorbed either on nanotubes or into a multilayer. Such a procedure effectively prevents the adsorption on surface sites that desorb the adsorbate around or below the temperature of dosing. In these experiments the exposure was chosen to be large enough so that a stationary state on the surface was reached and no further accumulation of the molecules on the SWNTs occurred.

Figure 31 demonstrates the n-pentane TPD spectra that result from five exposures near the onset temperature of the A peak and five exposures near the onset temperature of the B peak. The difference between two consecutive dosing temperatures within each set of five TPD spectra is 5 K. It can be seen that as the dosing temperature decreases, the A peak initially grows but the rate of growth slows down with each exposure and eventually a shoulder of the B peak starts to develop on the low temperature side of A. We take the area of the TPD trace No.3, where the rate of growth of A is suddenly slowed down and no B shoulder is visible, to be the area of the A peak. We believe that this method of removing the overlapping TPD intensity should correctly identify the initial coverage when the adsorption state in question is saturated. The main error in such an estimate comes from the inability to exactly identify the dosing temperature where the adsorption state being saturated stops growing.

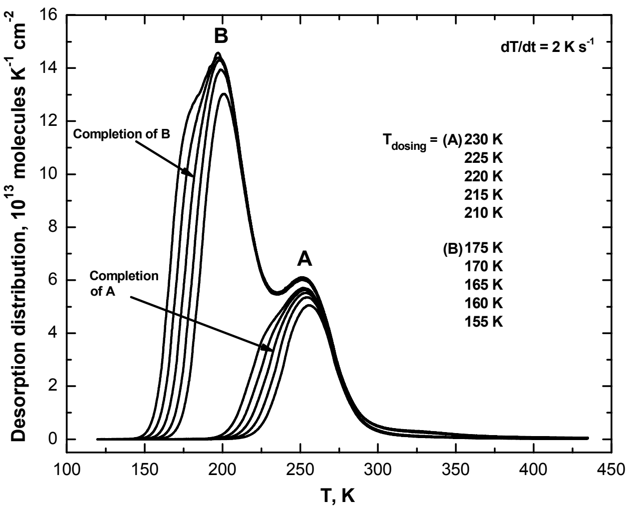

Figure 31. Finding the capacity of adsorption sites A and B by varying the dosing temperature in the TPD experiments. n-Pentane is given as an example of the procedure that was also used for other alkanes in the study.

A similar analysis can be conducted for site B. For n-pentane TPD spectra in Figure 31, spectrum No. 8 is then the sum of features A and B. The area of B can be found by subtraction.

In only the case of 2,2,4-trimethylpentane, peak A splits into several broad overlapping features and starts to overlap more significantly with peak B. Due to this fact the area of the peak A could not be determined with the varying dosing temperature method. This method could still be used to determine the area of A plus B. Figure 32 shows the TPD spectrum of 2,2,4-trimethylpentane on SWNTs at a dosing temperature where sites A and B are both saturated.

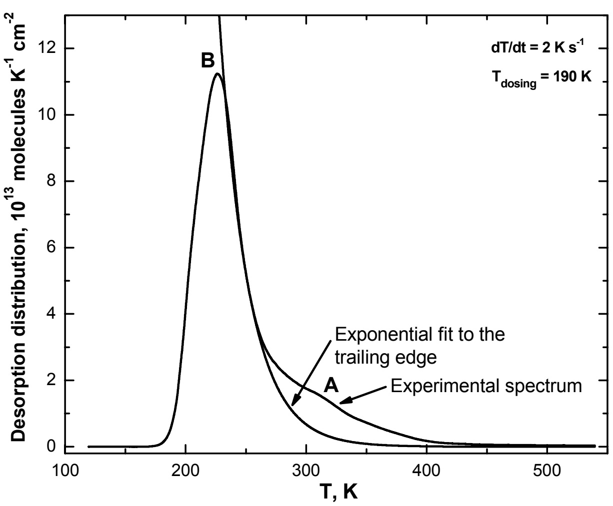

Figure 32. Finding the area of peak B in the case of 2,2,4-trimethylpentane. Extensive overlap of A and B can be seen. The trailing edge of B was fitted to a decaying exponential and all TPD intensity above the fit was assumed to belong to feature A.

We estimated the area of A and B for 2,2,4-trimethylpentane by fitting a decaying exponential to the trailing edge of the B peak where the overlap with A is expected to be small. It appears likely that this way of separating A and B will have some error associated with it. The resulting relative error in the case of B should not be particularly large because of the large total value of the B area, but is very likely significant in the case of A. For this reason we do not include the area of A for 2,2,4-trimethylpentane in our further analysis.

5.4.4 Groove site capacities.

Figure 33 summarizes the capacities of site B toward linear alkanes and 2,2,4-trimethylpentane. For convenience it is represented not as a capacity plot but rather as an inverse capacity, thereby representing the relative space occupied by a molecule on site B. The space occupied in the B site by an n-pentane molecule is taken to be 1. The error bars in Figure 33 represent the relative values that correspond to choosing two neighboring spectra in plots analogous to those in Figure 31. It is likely that the actual errors are less than those given by the error bars.

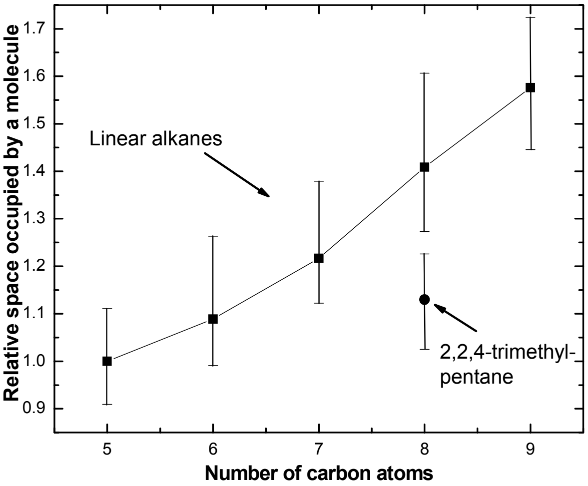

Figure 33. Experimentally determined relative amounts of space occupied in the groove sites, B, by five linear alkanes and by branched 2,2,4-trimethylpentane.

It is evident that an approximately linear relationship is observed for n-alkanes from C_5 to C_9, while the 2,2,4-trimethylpentane point clearly does not follow the trend expected for a C_8 molecule. A 2,2,4-trimethylpentane molecule occupies approximately as much space on site B as a hexane molecule, in accordance with its shorter carbon skeleton.

The linearity of the plot shown in Figure 33 and the lack of fit of 2,2,4-trimethylpentane at the C_8 position can be logically explained if site B is a one-dimensional adsorption site, where the length of the molecule determines the site's capacity toward the molecule. A natural choice for such a one dimensional site is the groove site between individual nanotubes in the bundle.

A 2,2,4-trimethylpentane molecule is significantly shorter than a n-octane molecule due to three branchings along the chain. Its main carbon chain is five atoms long, and this causes it to occupy less space in the groove site than a normal octane molecule.

We performed NVT simulations to investigate relationship between the capacities of the groove and interior sites of the nanotube bundle and the number of carbon atoms of the alkanes. We counted the number of segments on the interior sites and groove sites of the nanotube bundle during the course of the simulation. We then estimated the number of molecules in each of the sites by dividing the average number of segments in a site by the number of segments (carbon atoms) in the alkane molecule. The reciprocal of number of molecules per site is related to the capacities of these bundle sites. The relationship between the relative capacities of the groove site and number of carbon atoms for the different alkanes is shown in Figure 34. Note that data for the n-alkanes, shown as squares, lie on a nearly straight line, consistent with the experimental data in Figure 33. The circle point is for 2,2,4-trimethylpentane. The calculation of the number of molecules of 2,2,4-trimethylpentane in the groove site is based not on the number of carbon atoms in the chain, but on the number of carbon atoms in the backbone, i.e., five. This is because for 2,2,4-trimethylpentane, our definition of groove sites does not count the branched segments of a 2,2,4-trimethylpentane molecule as being in the groove sites since the branched segments lie outside the radius of the small dashed defining circle shown in Figure 28. We have confirmed this by analyzing snapshots from the 2,2,4-trimethylpentane simulations.

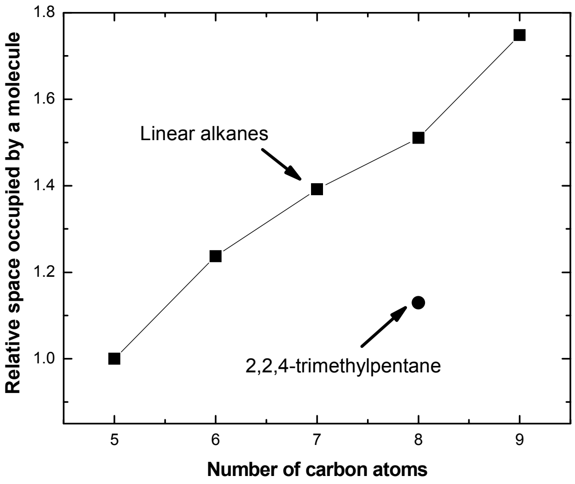

Figure 34. Relative space occupied in the groove sites for alkanes from molecular simulations.

Representative snapshots from simulations for both n-octane and 2,2,4-trimethylpentane in the groove sites are shown in Figure 35. The n-octane molecules lie roughly parallel in the groove site, packed end-to-end. The 2,2,4-trimethylpentane molecules each occupy less space than the n-octane molecules, as can be observed from the snapshots. Also, the 2,2,4-trimethylpentane molecules are more likely to rotate out of the groove site.

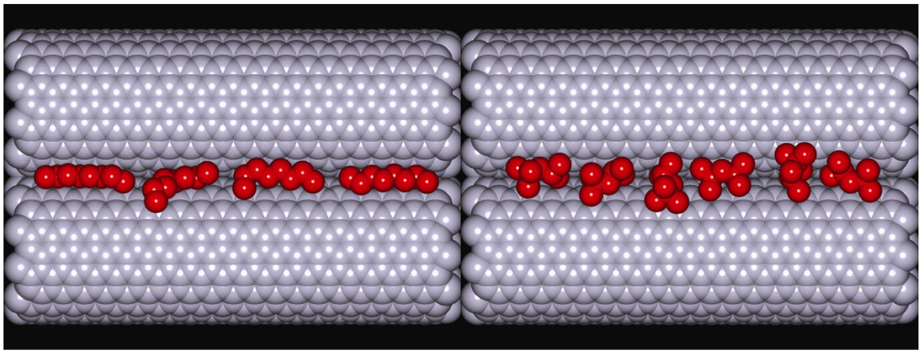

Figure 35. Simulation snapshots of n-octane and 2,2,4-trimethylpentane adsorbed on the groove site.

5.4.5 Interior site capacities.

The experimental data can be used to construct a plot similar to that shown in Figure 33 for the occupancy of the A site; this is shown in Figure 36. The 2,2,4-trimethylpentane point is not included because of significant uncertainty in its measurement. The uncertainty comes from a strong overlap of the A and B desorption peaks of 2,2,4-trimethylpentane, as explained in more detail in Section 5.4.3.

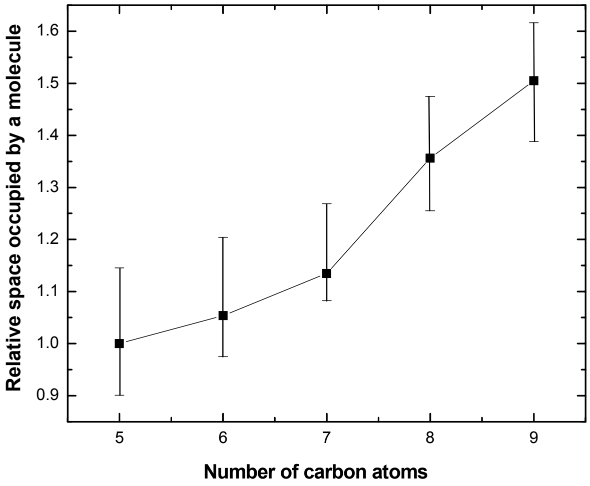

Figure 36. Experimentally determined relative occupation of space by alkane molecules in the interior of the nanotubes.

Simulation data for the inverse capacity of the interior site as a function of number of carbon atoms of an alkane are plotted in Figure 37. The squares are for the n-alkanes and the circle point again represents 2,2,4-trimethylpentane. We again observe a roughly linear relationship between the inverse capacity of the interior site and the number of carbon atoms in a molecule, in agreement with the experimental data of Figure 36. We find that 2,2,4-trimethylpentane lies on the same line as the n-alkanes and overlaps with n-octane, in contrast with the groove site data shown in Figures 33 and 34. This is because the capacity of the interior sites is governed by the volume, not the length of the site. Each segment in a molecule occupies about the same volume, whether the molecule is linear or branched. Therefore, n-octane and an 2,2,4-trimethylpentane occupy roughly the same amount of volume inside a nanotube. This is consistent with the observation that n-octane and 2,2,4-trimethylpentane have the same liquid molar volume to within 2% [123].

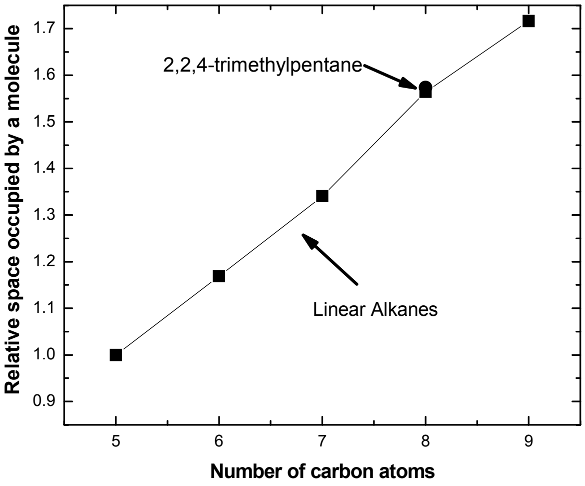

Figure 37. Relative space occupied in the interior sites for alkanes determined from molecular simulations.

5.4.6 Summary.

The following conclusions about alkane adsorption on single walled carbon nanotubes have been reached:

1) Three distinct adsorption sites are observed on single wall carbon nanotubes for alkane adsorption using temperature programmed desorption.
2) On the basis of molecular simulations (and earlier displacement experiments), the highest binding energy adsorption site (site A) corresponds to adsorption inside nanotubes.

3) The second highest binding energy site (site B) corresponds to groove sites between adjacent nanotubes in bundles.
4) Simulations find that desorption from the exterior surface of the nanotubes occurs at the lowest temperature, followed by desorption from the grooves and desorption from nanotube interior, which occurs at the highest temperature.
5) The adsorbed molecules are packed in a one-dimensional manner in the grooves. The length of the molecule determines the capacity of the groove site. Both experiments and simulations find that a branched C_8 molecule, 2,2,4-trimethylpentane, occupies less space in the groove than a linear C_8 molecule and approximately as much space as a linear C_6 molecule. This is due to the shorter main chain of 2,2,4-trimethylpentane as compared to n-C_8H_{18}.
6) Simulations show that in the interior of the nanotubes, a branched C_8 molecule, 2,2,4-trimethylpentane, occupies as much space as a linear n-C_8H_{18} molecule. This is because the capacity of the interior site is governed by the molecular volume of the alkanes, either linear or branched.

6.0 EFFECTS OF MOLECULAR CONFINEMENT INSIDE NANOTUBES ON CHEMICAL REACTIVITY – ATOMIC H + 1-HEPTENE[7]

It has been demonstrated that the confinement of physisorbed 1-heptene molecules inside of carbon single walled nanotubes (SWNTs) results in lowering of their reactivity to atomic hydrogen compared to 1-heptene molecules adsorbed on external SWNT sites.

6.1 INTRODUCTION

For a variety of molecules, the most energetically favorable adsorption site on carbon single walled nanotubes is the nanotube interior [45, 50, 93]. Such internally bound molecules may be discriminated from outside-bound molecules by several experimental methods [61, 63, 96, 100, 107, 124-126]. In contrast to some other high area adsorption substrates (such as activated carbon), the adsorption sites on SWNTs are well defined and possess relatively narrow ranges of adsorption energies. This allows the selective population of particular nanotube adsorption sites to be accomplished by appropriately choosing the adsorption temperature. The nanotubes also have the advantage of being largely chemically inert, exposing unreactive graphite-like surfaces and binding molecules only by van der Waals forces.

---

[7] This chapter is reproduced with modifications from a manuscript by P. Kondratyuk and J.T. Yates, Jr. with the same title which has been accepted for publication in the Journal of the American Chemical Society.

Since confined molecules adsorbed in the interior are more sterically shielded than those adsorbed on external adsorption sites, it can be expected that they will be less reactive toward reactants arriving from the outside. Here we study the relative rates of reaction of interior- and exterior-adsorbed 1-heptene undergoing hydrogenation by hydrogen radicals arriving from the gas phase. Extending the results described here to reactions in solutions may potentially open up uses for carbon nanotubes as a means of controlling molecular reactivity in synthetic chemistry.

The area of supramolecular chemistry offers conceptually analogous cases of the shielding of molecules from chemical reactions. As reported by Körner et al. [127], a nanoscopic self-assembled cylindrical capsule derived from resorcinarenes was able to enclose dibenzoyl peroxide molecules preventing a reaction with reducing agents present in the ambient solution. Nanotubes consisting of amphiphilic molecules [128, 129], zeolites [130], as well as dendritic supramolecular assemblies [131] and ligand-created cavities [132, 133] have all been studied with a view to molecular encapsulation.

6.2 RESULTS AND DISCUSSION

The experiment was conducted in the UHV chamber described in Chapter 2, with the addition of a tungsten filament for the production of atomic H. Figure 38 shows the principal components of the system and their relative locations.

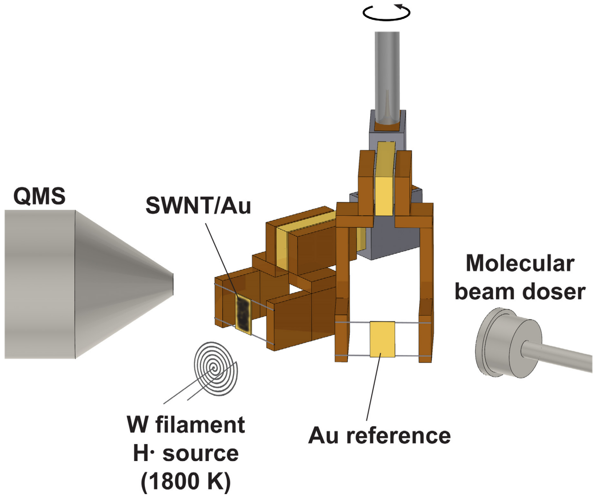

Figure 38. UHV apparatus for study of the adsorption and desorption of molecules on single walled carbon nanotubes, and for reactivity studies with atomic H, made from H_2 (g) using a heated W filament. A blank gold plate serves as a reference.

A sample of ~13.6 Å diameter SWNTs (mass = 24 μg) supported on a gold plate may be reproducibly positioned in front of a collimated and calibrated effusive beam doser for quantitative dosing of 1-heptene onto the nanotube sample [90, 134]. Before the temperature programmed desorption (TPD) experiments, the SWNTs are heated in vacuum to 1073 K, a procedure which removes carbonyl and ether groups which are initially present on SWNTs [56, 58]. Adsorption on SWNTs, followed by TPD, reveals that a hierarchy of adsorption sites, having different binding energies, is present [52, 114]. Four sequential desorption processes are observed as the temperature is raised, as shown in Figure 39 for adsorbed 1-heptene. Increasing coverage leads to thermal desorption processes occurring at progressively lower temperatures as sites with lower adsorption energies become occupied.

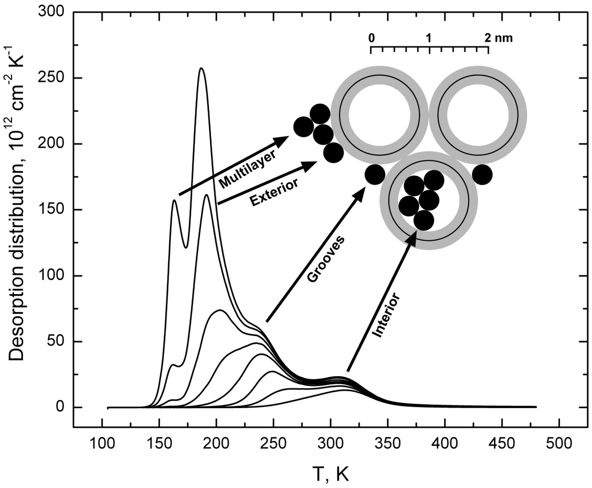

Figure 39. Temperature programmed desorption of 1-heptene from single walled carbon nanotubes for increasing initial coverages. The adsorption site locations corresponding to each desorption process are indicated on the schematic of a nanotube bundle [52, 114], where the SWNT diameter and the end-on van der Waals diameter of the 1-heptene molecules are drawn approximately to scale.

The highest temperature process corresponds to desorption from the nanotube interior, with the maximum rate of desorption at about 315 K. The next highest temperature process with rate maximum at about 230 K, corresponds to 1-heptene adsorbed in the exterior groove sites which exist between nanotubes held together in bundles by van der Waals forces [28]. The third from highest state corresponds to 1-heptene bound to the convex exterior SWNT wall sites [50], and the lowest temperature state corresponds to multilayer 1-heptene which forms on all exterior surfaces. The latter can be easily identified by the characteristic zero-order desorption kinetics that produces overlapping leading edges as the multilayer coverage is increased (not shown). Previous experiments have shown that this sequence of desorption states is observed for a number of hydrocarbons (linear and branched) [52], as well as for non-hydrocarbon molecules such as CCl_4 [114]. In the case of hydrocarbons, the saturated occupation of the interior sites is controlled by the volume occupied by the adsorbing molecule, whereas the occupation of the groove sites is governed by the molecule's length [52], as would be expected for a one-dimensional adsorption site. Control experiments from the clean gold reference were also carried out, to verify that all effects reported are due to 1-heptene adsorbed on the SWNTs.

We have selected an aggressive chemical reaction to study the effects of molecular confinement of 1-heptene on the reaction rate. The reaction of atomic H with the terminal double bond in alkenes is nearly non-activated [135, 136]. The reaction occurs readily on condensed alkene films even below 100 K, preferentially producing secondary alkyl free radicals [137]. The free radicals then undergo disproportionation by abstracting a hydrogen atom from a neighbor radical species [138, 139], producing the alkane and regenerating the alkene, as shown in equations (1) and (2) for the case of 1-heptene.

$$C_5H_{11}CH = CH_2 + \overset{\bullet}{H} \Rightarrow C_5H_{11}\overset{\bullet}{C}H - CH_3 \qquad (1)$$

$$2C_5H_{11}\overset{\bullet}{C}H - CH_3 \Rightarrow C_5H_{11}CH_2 - CH_3 + C_5H_{11}CH = CH_2 \qquad (2)$$

Thus, the production of heptane from 1-heptene may be used to monitor the reactivity of atomic hydrogen with the 1-heptene, and to measure the relative reactivity of interior-bound 1-heptene compared to exterior-bound 1-heptene.

For the comparison to be carried out between the reactivities of the interior- and exterior-bound 1-heptene, selective population of the adsorption sites in question must be accomplished. In the experiments described here, exclusive population of the nanotube interior was achieved by choosing the SWNT temperature to be 270 K during 1-heptene dosing. At this temperature only the interior sites were capable of retaining the adsorbate. Alternatively, when the 1-heptene adsorption temperature is set at 215 K, both the nanotube interior sites and the exterior groove sites become populated. Following such controlled adsorption, the SWNT samples containing 1-heptene were then subjected to atomic H irradiation at 150 K.

Figure 40 shows a sequence of TPD measurements of the relative desorption rates (proportional to the amplitude of the mass spectrometer signal in a fast-pumped vacuum system as used here [86]) as increasing irradiation by atomic H occurs, for the case when both interior and groove sites are filled with 1-heptene. The atomic H is produced by a W filament at 1800 K which operates in 4.4×10^{-5} Torr (using a relative ion gauge sensitivity factor of 0.46 compared to N_2) of continuously flowing H_2 [140]. The rate of bombardment by atomic hydrogen at the sample position is estimated to be $\sim2\times10^{13}$ H atoms cm^{-2} s^{-1}. The sample temperature is automatically controlled by resistive heating of the Au support plate to maintain a constant temperature of 150 K during irradiation [141].

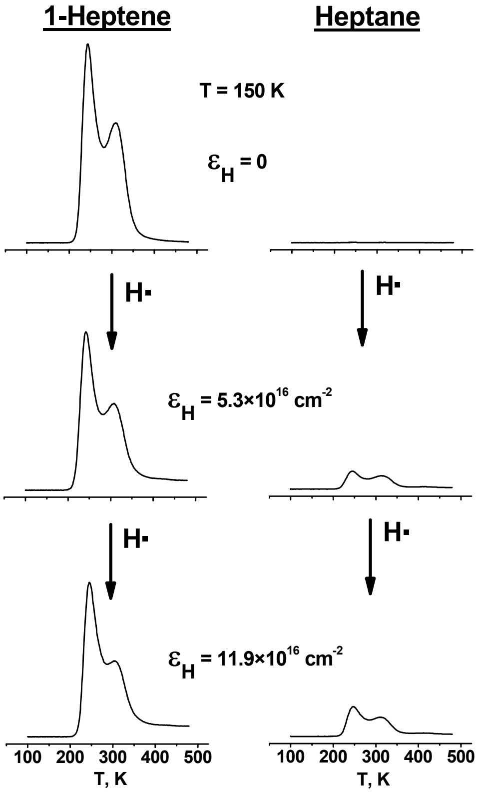

Figure 40. Series of experiments in which an identical coverage of 1-heptene, present in the interior sites and on external groove sites, is irradiated with atomic H for varying exposures, ε_H. The consumption of 1-heptene (m/e=98 a.m.u.) and the production of heptane (m/e=100 a.m.u.) is observed. Corrections have been made for the mass spectrometer sensitivity for the two molecules, so that the relative molecular population of 1-heptene and heptane may be measured from the area of the TPD spectra shown. To compare the hydrogenation rates, an identical series of experiments was also conducted for the SWNT sample with 1-heptene adsorbed only in the interior sites (corresponding to the high-temperature peak in the figure). dT/dt = 2 K s^{-1}.

As 1-heptene is consumed, heptane is produced. Since hydrocarbon molecule migration between different sites occurs readily when the temperature is increased during the TPD measurement, the distribution between the groove sites and the interior for the two molecules will not reflect the relative rates of hydrogenation in the two sites. Thus, it is only the amount of heptane produced that is of interest in this experiment, not the distribution between the groove sites and the interior.

When the 1-heptene is exclusively contained in the interior sites of the SWNTs, a lower rate of reaction is observed, compared to experiments in which both interior and groove sites are occupied, as shown in Figure 41.

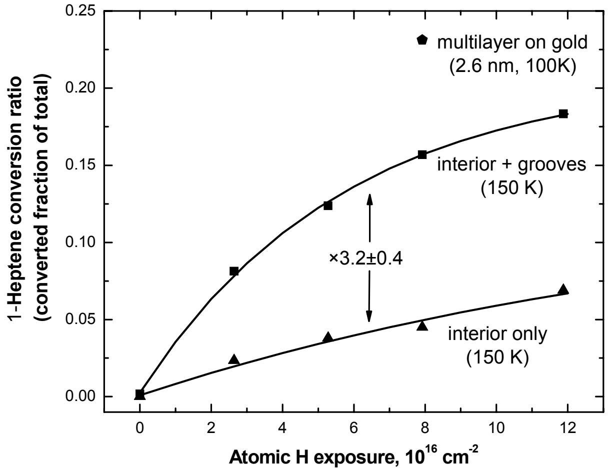

Figure 41. Fraction of 1-heptene converted to heptane by atomic H, using SWNTs containing 1-heptene in interior sites, compared to experiments involving the occupancy of interior and external groove sites.

Figure 41 shows that the reactivity of molecules exclusively in interior sites is a factor of 3.2±0.4 lower than that found for nanotubes exposing 1-heptene in both interior and exterior groove sites. The single point shown in Figure 41, corresponding to a study of multilayer 1-heptene reactivity with atomic H on the Au reference surface, shows that the conversion ratio for the reaction is even higher for the unconfined 1-heptene multilayer.

These results show that confinement of a reactant molecule inside a single wall nanotube results in a substantial reduction of its reactivity with an aggressive gas phase reactant. The observation of ***some*** reactivity for the confined molecules is probably due to the chemical opening of the tubes needed for molecular adsorption into the interior [56, 60, 63]. These openings provide the pathways for the H radicals to access the interior-adsorbed molecules.

It is known that the nanotubes can themselves react with atomic H [142, 143]. Indeed, after exposures to H comparable to those in the experiments described above, but without any 1-heptene adsorbed on the SWNTs, we find that chemisorbed hydrogen was present on the SWNT sample. When the SWNTs were heated to 800 K, H_2 as well as hydrocarbons with between 1 and 5 carbon atoms in the chain were evolved. Using the mass spectra of the evolved hydrocarbons and the experimentally measured QMS sensitivities towards hydrocarbons with different chain lengths, we estimated the amount of carbon lost per one cycle of hydrogenation at only 0.07% of the total number of carbon atoms in the SWNTs, meaning that nanotube hydrogenation can be neglected under these conditions. This amount of reacted carbon was about two orders of magnitude smaller than the amount of carbon in the adsorbed 1-heptene molecules.

6.3 CONCLUSIONS

It was found that nanotube walls prevent atomic H species from entering and undergoing reaction with the double bonds of confined alkene molecules. This observation suggests a new use for nanotubes in which molecular confinement is used to control the chemical reactivity of a molecule.

7.0 INTER- AND INTRA-TUBE SELF-DIFFUSION IN N-HEPTANE ADSORBED ON NANOTUBES[8]

We have experimentally measured long-range self-diffusivity of normal heptane adsorbed on single walled carbon nanotubes at 275 K. This was done by observing the displacement kinetics of heptane by a deuterium-labeled molecule, 1-deuteroheptane. We also performed MD simulations of heptane self-diffusion inside an individual nanotube under full loading. The experimentally measured diffusion coefficient (D = 7.7×10^{-12} cm^2 s^{-1}) was about 8 orders of magnitude lower than the diffusion coefficient inside an individual nanotube from the simulation (D = 8.2×10^{-4} cm^2 s^{-1}). Since heptane only adsorbs in the nanotube interior at 275 K, we conclude that the experimentally observed long-range transport is rate-limited by a very slow exchange of heptane between different nanotubes in the bulk SWNT sample. At the same time, the mixing of heptane inside individual nanotubes is fast. The reasons for slow diffusion between different tubes could be the potential energy barriers at the entry points into the nanotubes, as well as desorption-adsorption barriers for molecules migrating through the bulk.

---

[8] This chapter is reproduced with modifications from: P. Kondratyuk, Y. Wang, J. Liu, J.K. Johnson and J.T. Yates, Jr.; Inter- and intra-tube self-diffusion in n-heptane adsorbed on carbon nanotubes. J. of Phys. Chem. C (2007), 111, 4578-4584. The computer simulations presented in this work were carried out by Y. Wang, J. Liu and J.K. Johnson.

7.1 INTRODUCTION

From a practical standpoint, the transport properties of adsorbed molecules play an important role in determining the applicability of single wall carbon nanotubes (SWNTs) as adsorbents, as they control the rates of molecular uptake and release. While a number of studies have focused on molecular transport along the nanotube channels [144-149], few [150] have addressed the diffusion dynamics of the molecules in the bulk of the nanotube samples and none investigated the self-diffusion of adsorbates. On the other hand, self-diffusion in such well-studied media as zeolites has received a significant amount of attention [151-161].

Here we study experimentally the self-diffusion of heptane through a bulk SWNT sample. We compare the results to a molecular dynamics (MD) simulation of heptane diffusion inside an individual nanotube under the conditions of full heptane loading. Heptane was chosen due to the earlier findings that normal alkanes allow the different adsorption sites on SWNTs to be resolved by temperature programmed desorption (TPD) [52].

The temperature in the experiment was chosen such that only the interior adsorption sites could be populated while other types of sites remained unoccupied [52]. This allowed us to experimentally probe the dynamics of heptane exchange between different tubes.

Several techniques have been used to determine the self-diffusion coefficients of adsorbed molecules in microporous solids, among them field-gradient NMR [151, 154, 155, 157, 160], inelastic neutron scattering [161] and the use of isotopically labeled molecules [158, 159]. The latter is employed here. It is based on the displacement of the adsorbed molecules by isotopically labeled but otherwise identical molecules. The slower the diffusion, the more slowly will the displacement occur because of the accumulation of the labeled molecules in the outer layers of the microporous solid.

The SWNTs are a nanostructured material, and consequently, at the nanoscale the propagation of molecules does not obey the normal Gaussian law. This effect is well known for zeolites [151-153]. In particular, a molecule confined inside a zeolite cavity may experience rapid diffusion within the confining boundaries while hopping between different cavities may be very rare. The case of heptane on SWNTs is highly analogous. Under our experimental conditions the molecules were adsorbed only inside nanotubes. Thus two transport regimes were present, inside individual nanotubes and between different nanotubes. The experimentally measured diffusion coefficient corresponds to long-range transport and, consequently, diffusion between different nanotubes. This diffusion was found to be vastly slower than the diffusion inside individual nanotubes seen in the MD simulation.

Various groups have simulated the diffusion of molecules adsorbed in the interior channels of SWNTs [144, 147, 162-168]. Previous simulation studies have shown that transport of small molecules can be much more rapid inside individual SWNTs than in other nanoporous materials [162, 169-171]. The transport of alkanes inside SWNTs has also been noted to be rapid [165, 166, 168].

7.2 EXPERIMENTAL

7.2.1 System and Materials

The experiments were performed in a stainless steel ultrahigh vacuum (UHV) system with a base pressure of 2×10^{-10} Torr after bakeout. A detailed description of the system is given in Chapter 2 of this Dissertation.

The SWNTs were produced by R. Smalley and coauthors by pulsed laser vaporization of graphite impregnated with a Ni-Co catalyst [21, 22]. Production and purification of the SWNTs used here are discussed in Section 2.3. The average diameter and length of the nanotubes in the sample was 13.6 Å and 320 nm respectively.

The nanotubes were deposited in air onto a gold support plate measuring 10×14 mm. The solvent was allowed to evaporate, leaving a nanotube deposit of ~36 μg. On the basis of the approximate density of compressed SWNTs of 1.33 g/mL [172] we estimate that the average thickness of the deposit was ~0.2 μm.

Dosing of heptane and 1-deuteroheptane was accomplished with two calibrated pinhole conductance molecular beam dosers [89, 115].

Heptane was purchased from commercial sources and purified by two freeze-pump-thaw cycles. 1-deuteroheptane was synthesized from 1-iodoheptane and $LiAlD_4$ and had a measured purity of 99%. Freeze-pump-thaw purification was likewise performed.

7.2.2 Experimental procedures

The displacement experiment involved first exposing the sample to a large amount of heptane at 275 K. This exposure was large enough to completely saturate all available interior sites. We earlier showed that other types of sites remain unoccupied at this temperature [52].

Following the exposure to heptane the sample was immediately rotated to a second doser producing a required flux of 1-deuteroheptane. As there are no unoccupied sites remaining on the surface that could be filled at this temperature, a 1-deuteroheptane molecule could only adsorb if it displaced a heptane molecule. The gradual displacement of heptane was then allowed to occur for a required period of time after which the sample was rotated away from the 1-deuteroheptane doser and its temperature was immediately dropped to avoid any desorption from the surface.

The two molecular beam dosers were operated continuously during the experiments in order to minimize the delay between exposures to heptane and 1-deuteroheptane. When the sample was not directly in front of a doser, it only intercepted a small fraction of the molecular flux (~3%) due to the very fast pumping of heptane by the UHV system and by the cold parts of the sample holder at 77 K. The ~3% value was measured by positioning the sample away from the doser and measuring the amount of heptane (or 1-deuteroheptane) adsorbed on it after a certain time.

After the exposures to heptane and 1-deuteroheptane the sample was positioned in front of a 3 mm diameter aperture of a shielded quadrupole mass spectrometer (QMS). The temperature was then linearly increased at a rate of 2 K s^{-1} and the signal of the QMS caused by the desorbing molecules was recorded simultaneously at m/e = 100 (almost exclusively due to heptane) and 101 (mostly 1-deuteroheptane, some contribution from heptane if it is present in the desorbing flux). The QMS shield was biased to -100 V to prevent the electrons from the QMS ionization chamber from impacting the sample [173].

By knowing the QMS signal intensities at masses 100 and 101 a.m.u. during the TPD, one can calculate the fluxes of desorbing heptane and 1-deuteroheptane. To enable such a calculation, we experimentally measured the ratios of sensitivities of the QMS toward heptane and 1-deuteroheptane at the two masses. The ratios of sensitivities were found to be I_D^{101} / I_D^{100} = 50.8, I_H^{100} / I_H^{101} = 12.7, and I_H^{100} / I_D^{101} = 1.0, where the subscripts H and D denote the sensitivities toward heptane and 1-deuteroheptane respectively, and superscripts 100 and 101 denote the mass fragment in question. By also knowing the absolute sensitivity from calibration for one of the molecules (heptane), a linear system of two equations can be solved for the two unknown fluxes.

Integration of the TPD spectra for heptane and 1-deuteroheptane allows the amounts of each molecule present on the surface at the time of the TPD measurement to be determined. These values were used for further analysis.

It was found that because both heptane and 1-deuteroheptane dosers were on during exposure to either gas, the sample saw a small amount of exposure to the molecules from the doser in front of which it was *not* positioned. For instance, in one of the experiments it was found the sample was exposed to 96.6% of heptane and 3.4% of 1-deuteroheptane ("H mixture") when it was positioned in front of the heptane doser, and 94.7% of 1-deuteroheptane and 5.3% of heptane ("D mixture") when in front of the 1-deuteroheptane doser. Thus it is not the displacement of heptane by 1-deuteroheptane that occurs in this experiment, but rather the displacement of "H mixture" by "D mixture". Because of the linearity of the diffusion equations, the displacement kinetics of both processes are identical. All that needs to be done to correct for the non-100% composition is to convert the amounts of heptane and 1-deuteroheptane into the amounts of the appropriate "H" and "D" mixtures. Such a correction was always made for the displacement data presented here and the results are given for simplicity as the displacement of heptane by 1-deuteroheptane. The derivation of the formulas for the conversion from the amounts of 1-deuteroheptane and heptane to the amounts of "H mixture" and "D mixture" are given in Appendix A.

During the displacement experiments, a drift in the sensitivity of the QMS was seen over the course of hours and days. In order to correct for this slow drift, the sum of the amounts of heptane and 1-deuteroheptane was normalized to 2070×10^{12} molecules cm^{-2}, the capacity of the sample from a calibrated measurement. These changes in the QMS detector sensitivity were the dominant source of uncertainty in these measurements.

The interpretation of the results in terms of self-diffusion is based on the premise that the system cannot distinguish between the two molecules, in other words, that all the thermodynamic properties for the adsorption of heptane and 1-deuteroheptane are identical. We tested this hypothesis by TPD and could not observe any measurable differences in the desorption kinetics of the two molecules.

All the measurements presented here were performed using an automatic system described in Chapter 2. Short delays between the dosing operations and the TPD spectra acquisition helped ensure that the sample is exposed to the background flux of the adsorbates as little as possible.

Before each series of experiments the nanotube sample was annealed at 1073 K for 10 minutes to decompose the traces of oxygen functionalities that might be present on the nanotubes [56].

7.3 SIMULATION METHODS

We have used molecular dynamics (MD) to study the diffusion and mobility of heptane molecules in both the bulk and adsorbed phases. The intra-molecular degrees of freedom were integrated using the multiple-time-step reversible reference system propagation algorithm [119]. The value of the long time step was 5 fs. Each long time step consisted of five inner (short) time steps. We used the transferable potentials for phase equilibria (TraPPE) [121] united atom model for heptane molecules, in which the CH_3 and CH_2 groups are defined as single united atom segments. The total potential is a sum over four types of potentials, namely: non-bonded, bond stretching, bond bending, and dihedral torsion. Equations 1 to 4 give the functional form for each type of potential.

$$u(r_{ij}) = 4\varepsilon_{ij}\left[\left(\frac{\sigma_{ij}}{r_{ij}}\right)^{12} - \left(\frac{\sigma_{ij}}{r_{ij}}\right)^{6}\right] \tag{1}$$

$$u_{stretch} = \frac{1}{2}k_r\left(r - r_0\right)^2 \tag{2}$$

$$u_{bend} = \frac{1}{2}k_\theta\left(\theta - \theta_0\right)^2 \tag{3}$$

$$u_{tors} = c_0 + c_1\left[1 + \cos\phi\right] + c_2\left[1 - \cos(2\phi)\right] + c_3\left[1 + \cos(3\phi)\right] \tag{4}$$

The bond stretching term was adopted from the OPLS-UA force field.

Standard Lorentz-Berthlot combining rules were applied to calculate the cross terms, σ_{ij} and ε_{ij},

$$\sigma_{ij} = \frac{1}{2}\left(\sigma_{ii} + \sigma_{jj}\right) \tag{5}$$

$$\varepsilon_{ij} = \sqrt{\varepsilon_{ii}\varepsilon_{jj}} \tag{6}$$

Potentials parameters used in the equations are shown in Tables 3 and 4.

Table 3. Lennard-Jones Parameters for TraPPE-UA Field for heptane.

Pseudo-atom	ε/k_B [K]	σ [Å]
CH_3	98	3.75
CH_2	46	3.95

Table 4. Bonded Parameters for the TraPPE-UA Force Field for heptane.

Stretch	r_0 [Å]		k_r/k_B [K]	
CH_x-CH_y	1.54		130924.4893*	
bend	θ_0		k_θ/k_B [K]	
CH_x-(CH_2)-CH_y	114		62 500	
torsion	c_0/kB [K]	c_1/kB [K]	c_2/kB [K]	c_3/kB [K]
CH_x-(CH_2)-(CH_2)-CH_y	0	335.03	-68.19	791.32

*This parameter is from OPLS-UA force field.

Equilibrium molecular dynamics (EMD) [174, 175] was used to calculate the heptane diffusion coefficients for both bulk and nanotube confined heptane molecules. We used the Nosé-Hoover thermostat [176] to correctly sample the canonical (constant temperature) ensemble. The bulk heptane phase consisted of 100 heptane molecules at a density of 0.7 g/ml. The nanotube system used to compute the self-diffusion coefficient of heptane within a SWNT consisted of a single (10, 10) nanotube, 295.14 **Å** (120 unit cells) long. The nanotube contained 93 heptane molecules; this loading corresponds to a bulk phase pressure of 1.5×10^{-3} Torr. The density of heptane inside the SWNTs is not well defined, because it depends on how one calculates the volume of the nanotube. If we just take the nanotube radius and length to calculate the volume ($\pi r^2 l$) of the nanotube, the density we get is 0.36 g/ml, which is rather low for a liquid like phase. However, if we include the volume of the carbon atoms on the nanotube (through their van der Waals radius) and calculate the nanotube volume as the accessible volume ($\pi(r-\sigma/2)^2 l$), the density of the heptane increases to 0.65 g/ml, which is close to the bulk liquid density. The system was periodic in the *z*-direction (along the nanotube axis). The self-diffusivity measures the mobility of a single tagged molecule moving through the system. The self-diffusion coefficient can be calculated from molecular simulations by using the Einstein relation [177]

$$D_s(c) = \lim_{t\to\infty} \frac{1}{2dNt} \left\langle \sum_{i=1}^{N} \left| \vec{r}_i(t) - \vec{r}_i(0) \right|^2 \right\rangle , \tag{7}$$

where c is the concentration of the molecules, d is the dimensionality of the system, N is the number of the molecules, t is the simulation time, and $\vec{r}_i$ is the vector of the center of mass of the ith molecule. For bulk phase systems, $2d = 6$. For molecules adsorbed inside a nanotube, diffusion occurs only in one dimension (along the nanotube axis) in the limit of long time, so $2d$

= 2. In addition, we consider only the displacement along the axis of the nanotube so that $\vec{r}_i$ is replaced by z_i in eq 7.

Nanotubes in our simulations are atom explicit and are held rigid. The Lennard-Jones parameters used for the carbon atoms in the nanotube were taken to be those for graphite ($\sigma = 3.4$ Å, $\varepsilon = 28.0$ K) [120].

The MD simulations described above were carried out with fixed number of molecules in the simulation cell. The pressure of heptane in the bulk phase in equilibrium with the heptane adsorbed on the nanotubes is unknown in the MD simulations. We have therefore carried out a series of grand canonical Monte Carlo (GCMC) simulations [177] to find the equilibrium loading of heptane on the external and internal sites of a model SWNT bundle as a function of the gas phase pressure. We used the Towhee simulation package [122, 178], which is an implementation of the continuum configurational bias method [179], in our calculations. The chemical potential, rather than the pressure, is specified in GCMC simulations. We therefore performed additional bulk phase simulations to relate the chemical potentials to the bulk phase pressures.

Simulations for adsorption of heptane on the external surface of a nanotube bundle used two parallel SWNTs, separated by 3.4 **Å.** Each nanotube had a length of 49.19 **Å** (20 unit cells). The bundle was placed in the center of a cubic simulation cell, 100 Å on a side. Molecules were not allowed to adsorb in the interior of the SWNTs in this case. Adsorption inside a SWNT was modeled by using an array of SWNTs and allowing adsorption only inside the nanotubes. A total of 6×10^6 configurations were used, with each configuration consisting of an attempted move, where a move is one of the following: insertion, deletion, translation, rotation, or molecule regrowth. The type of move was chosen with equal probability.

7.4 RESULTS AND DISCUSSION

7.4.1 Efficient adsorption into internal sites

We have reported earlier that linear alkanes afford an unexpected resolution of adsorption sites on SWNTs [52]. Figure 42 contains TPD spectra of heptane showing peaks for internal sites, groove sites on the outside of the bundles, and exterior sites according to our previous assignment. Multilayer heptane adsorption/desorption is observed at the highest exposures.

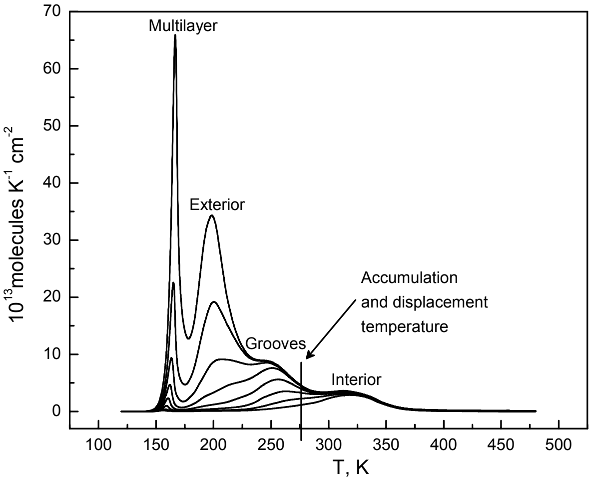

Figure 42. Heptane TPD spectra showing resolved peaks for interior, groove and exterior SWNT adsorption sites. The temperature used in the displacement experiment only allows the interior sites to be populated. The exposures to heptane ranged from 2.2×10^{15} to 24.3×10^{15} molecules/cm^2. Consecutive exposures differed by a factor of 1.41.

The sites identified as interior have the highest adsorption energy. They are the only sites that could adsorb heptane at the temperature in the experiments, 275 K.

The first step in measuring the diffusion coefficient is filling the nanotube interior with the unlabeled molecule, heptane. The approach to equilibrium surface coverage versus the exposure to heptane is illustrated in Figure 43. The curve saturates at exposure of approx.

5000×10^{12} molecules cm^{-2}. The saturation exposure used in further experiments was chosen to be slightly higher, 5800×10^{12} molecules cm^{-2}, to guarantee that all interior sites were filled.

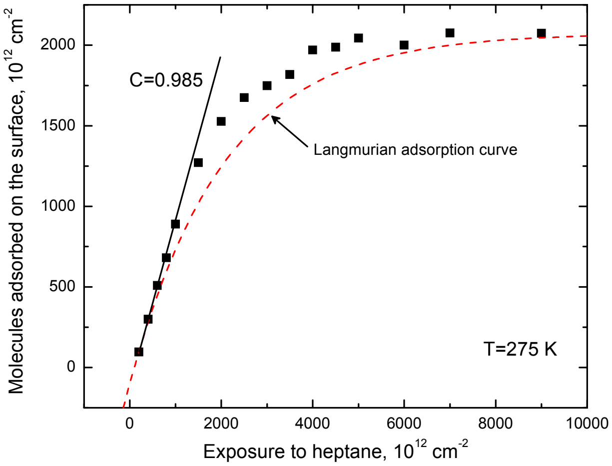

Figure 43. Approach to equilibrium surface coverage with increasing exposure to heptane at 275 K. The initial sticking coefficient is very close to unity. The solid line is the linear fit to the initial data points, the dashed line is the Langmuir-type approach to saturation.

The initial sticking coefficient, *C*, is very close to 1 as measured by the initial slope of the saturation curve. The near unity value seen here can be rationalized in the following way. Even though the groove sites cannot retain heptane at 275 K over a long period of time (see Figure 42), the residence time of heptane there is still more than sufficient to allow the molecules to migrate and find the more strongly-binding internal sites. We estimate this residence time at 0.2 s from the groove site peak temperature (252 K) assuming the first-order desorption model and a preexponential factor of 10^{15} s^{-1} [180]. This pre-exponential factor is a logarithmic average of values for n-hexane and n-octane, which were calculated in an MD simulation of alkane desorption from Au(111) [180]. The pre-exponential factor and the peak desorption temperature can be used to find the adsorption energy. In turn, the adsorption energy, in combination with the pre-exponential factor, produces the abovementioned residence time on the surface of approximately 0.2 s. Thus the incoming heptane molecules first adsorb in the groove sites before migrating to the interior sites that are inaccessible directly from the gas phase. A pre-adsorption migration stage in the grooves helps explain both the unity sticking coefficient and the fact that the adsorption proceeds faster than dictated by the Langmurian localized adsorption kinetics (dashed line in Figure 43), where the probability of adsorption for the incoming molecule would be (1-θ), θ being the fractional coverage.

7.4.2 Self-diffusion through the 0.2 μm thick sample

Once the saturation coverage has been reached, further addition of heptane (or 1-deuteroheptane) causes the displacement of previously adsorbed molecules. A typical result of an experiment where heptane is displaced with 1-deuteroheptane is shown in Figure 44. If the diffusion were infinitely fast, the displacement would follow the perfectly stirred reactor (PSR) model and the concentration of heptane would decay exponentially with exposure to 1-deuteroheptane. However, a finite rate of diffusion causes the 1-deuteroheptane to accumulate in the outer layers of the sample and the displacement proceeds more slowly because more incoming 1-deuteroheptane molecules displace molecules of the same type, 1-deuteroheptane.

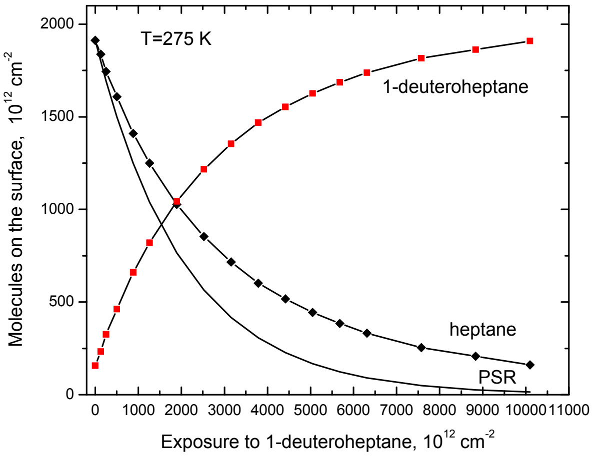

Figure 44. Displacement of heptane with 1-deuteroheptane at 275 K. Finite rate of diffusion causes the deviation from the first-order exponential decay dictated by the perfectly stirred reactor model (PSR).

Increasing the delivery rate of 1-deuteroheptane makes the displacement less efficient per unit exposure as less time is available for the concentrations to equilibrate throughout the sample. Figure 45 provides experimental results that illustrate this point. Here, a more convenient semilogarithmic format is adopted. The y axis is the natural logarithm of the fraction of the total capacity occupied by heptane. The x axis is the exposure to 1-deuteroheptane in units of total capacity (1 c.u. = 2070×10^{12} molecules cm^{-2}). On such a plot, the PSR model results in a line with a slope of -1 passing through the origin. This slope corresponds to the highest rate of displacement. Less efficient mixing causes the positive deviation of the slope from the PSR model.

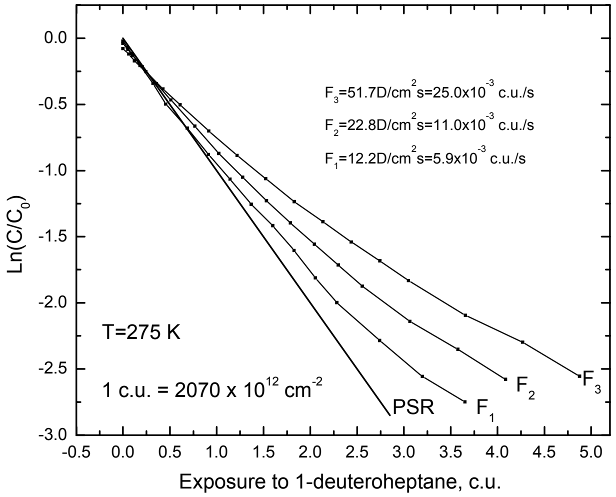

Figure 45. Displacement of heptane with 1-deuteroheptane at three different dosing rates, F_i. Faster dosing rates result in less efficient displacement per unit exposure to 1-deuteroheptane. The line labeled PSR corresponds to perfectly stirred reactor model (*F*=0). The initial slopes, used to calculate the diffusion coefficient through the SWNT bulk, were found to be -1.0, -0.83, -0.70 for 1-deuteroheptane fluxes F_1, F_2, F_3 respectively.

We will show later that slight non-linearity noticeable at higher exposures in Figure 45 is likely caused by the inhomogeneities in the thickness of the SWNT deposit. We will use the initial linear regions of the curves to determine the self-diffusion coefficient under these conditions.

A straightforward physical model of the displacement process can be constructed in the following way. We will consider the SWNT deposit to have a uniform thickness of 0.2 μm and the transport of the molecules inside the deposit be governed by Fick's law of diffusion. The incoming 1-deuteroheptane molecules displace the molecules in the outer layer of the deposit with 100% efficiency. The displaced molecules will be a mix of heptane and 1-deuteroheptane in the same fractional ratio as in the outer layer of the nanotube deposit.

Physically, this means that the lifetime of the incoming molecules on the surface is large enough for them to mix perfectly with the molecules in the outer layer. Another consequence of long initial residence time on the surface is the unity sticking coefficient, as mentioned before (Figure 43).

In order to follow displacement kinetics in a system corresponding to such a model, a differential equation for diffusion with two appropriate boundary conditions must be solved. The boundary condition for the outer layer is that heptane flux through the boundary is proportional the concentration of heptane. The other boundary condition stipulates that there is no flux of heptane through the surface of the nanotube deposit adjacent to the gold plate. An analytical solution for this particular problem exists [181], however, it has a drawback of being non-algebraic. For this reason we used a fairly straightforward finite differences approach, as described by Bard and Faulkner [182].

There are three parameters in this model: diffusion coefficient D, deposit thickness L, and the fraction of molecules replaced in the outer layer in unit time, α. The dimensionless ratio $D/(\alpha L^2)$ fully defines the displacement kinetics. Several displacement curves produced by the model are shown in Figure 46 using the same coordinates as on the experimental plot in Figure 45. The displacement curves in Figure 46 are nonlinear at low exposures. They become linear after exposures greater than approximately 1 c.u. Decreasing $D/(\alpha L^2)$ leads to lower negative values of slope.

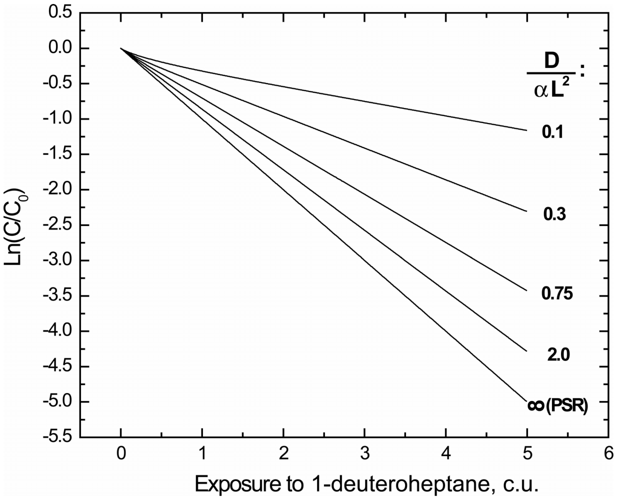

Figure 46. Displacement of heptane by 1-deuteroheptane as given by the coupled diffusion-displacement model. After an initial non-linearity, the amount of heptane remaining in the SWNTs decays exponentially with the addition of 1-deuteroheptane. The dimensionless ratio $D/(\alpha L^2)$ (defined in the text) controls the kinetics of the process.

The model allowed us to determine the diffusion coefficient. Knowing L (0.2 μm) and α (F_i's from Figure 45 expressed in c.u.), we solve for the value of D such that the slope of the displacement curve given by the model in the linear region matches the initial slope of the experimental displacement curves. Two experimental curves from Figure 45 were employed in this analysis, F_2 and F_3. The value of $D=7.7\times10^{-12}$ cm^2/s gave a good agreement with initial slopes of both experimental curves. This value compares to the bulk-phase D value for liquid heptane of 2.4×10^{-5} cm^2/s at 275 K [183].

This value of diffusion coefficient is about eight orders of magnitude lower than that obtained for heptane inside a filled nanotube found from MD simulations, 8.2×10^{-4} cm^2/s (see below). This indicates that the diffusion inside nanotubes is not the rate-limiting step in heptane mixing throughout the nanotube sample. As the heptane in the sample is partitioned into separate populations inside open nanotubes, it is logical to conclude that the slow diffusion observed in the experiment is caused by slow exchange of heptane between different nanotubes.

We speculate that this slow inter-tube exchange is caused by the relatively deep potential well for molecules residing in the interior of the nanotubes, as well as potential barriers for entry and exit from the nanotubes. Similar energy barriers were seen by Calbi and Riccardo [184] in the simulations of molecular hydrogen adsorption in the interstitial channels of closed (10,10) tubes. The authors observed that the effect of the barrier presence was a dramatic slowing in the kinetics of interstitial adsorption.

In addition to the potential barriers for nanotube entry and exit, desorption-adsorption barriers must exist in our SWNT sample for molecular transport between different nanotube bundles.

The α=F_1 curve was not used in the analysis because of the insensitivity of slope to the value of D at high $D/(\alpha L^2)$. We expected, however, the initial slope of this curve to be higher than the observed value of -1.0.

The non-linearity at higher exposures in the experimental data can be explained by thickness inhomogeneities in the nanotube deposit. Thicker areas have a lower $D/(\alpha L^2)$ and thus are more slowly depleted of heptane. Desorption from these thicker areas starts to dominate when the amount of remaining heptane becomes low. In the determination of the self-diffusion coefficient we used the slope at low exposures from the experimental curves where it is fairly constant.

7.4.3 Adsorption of heptane on a model SWNT bundle

We have computed adsorption isotherms for heptane adsorbing on the external and internal surfaces of a model SWNT bundle in order to estimate the external bulk phase pressure that corresponds to different loadings. The computed isotherms are plotted in Figure 47. The solid circles represent adsorption on the external surface of the nanotubes; this would occur if the internal sites were blocked or if diffusion into the nanotube interior was kinetically limited. The graphic insets in Figure 47 are snapshots from the simulations, showing a typical coverage of heptane on the SWNT bundle. Considering only external adsorption, molecules first adsorb in the groove site and the density is seen to increase smoothly with increasing pressure. There is no evidence for a layering transition as might be expected on graphite [185, 186]. The first plateau-like region from about 10^{-2} to 10^{-1} Torr corresponds roughly to groove site filling. The next rise in the isotherm is indicative of adsorption taking place on the external surface of the nanotubes. This is followed by a steep rise in coverage that marks the beginning of the multilayer.

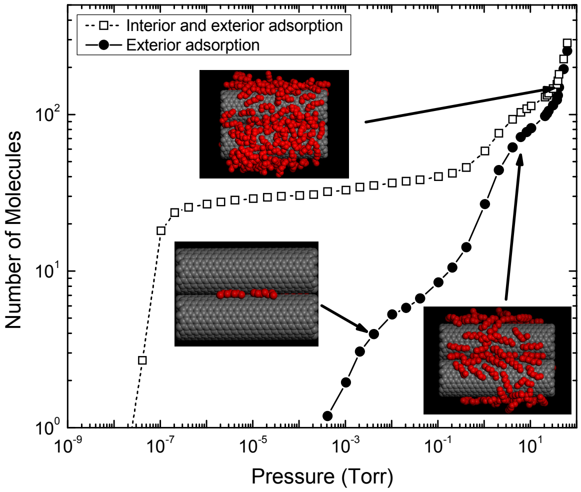

Figure 47. Adsorption of heptane at 275 K on a model SWNT bundle containing two nanotubes. The filled circles are for adsorption only on the external surface of the nanotubes and the open squares indicate adsorption both on the internal and external sites. Representative snapshots from the simulations are shown as insets.

The simulations indicate that at the experimental pressures of heptane (below 10^{-9} Torr) the interior sites can only be populated in a quasi-equilibrium fashion. However, one has to remember that during the dosing of the adsorbates the sample is exposed to far higher local pressures which permit the filling of the nanotube interior. The kinetics of desorption from the interior is sufficiently slow (occurring on the timescale of tens of seconds) as compared to the rates of adsorbate delivery in these experiments.

7.4.4 Self-diffusion inside individual SWNTs from MD simulations

We have calculated the self-diffusion coefficient for bulk liquid heptane from EMD simulations at 275 and 298 K. The results from our calculations are given in Table 5. The experimental value of the liquid self-diffusivity at 298 K is also reported in Table 5. The simulation and the experimental values at 298 K are in excellent agreement, giving us confidence that the potential models used in the simulations for heptane are physically reasonable. The liquid self-diffusivity at 275 K calculated from our simulations is physically reasonable, being slightly smaller than the value at 298 K. We have estimated an experimental value for the self-diffusivity at 275 K from interpolation of existing experimental data [183]. Our simulation result is in reasonable agreement with the interpolated value, given the errors involved in the interpolation process.

Table 5. Calculated and experimental [183] self-diffusion coefficients for bulk liquid heptane.

Temperature (K)	Self-diffusion coefficient ($D_s \times 10^5$ cm^2/s)	
	Simulations	Experiments
275	2.7 (0.1)*	2.4**
298	2.9 (0.3) *	3.1

***The numbers in the parenthesis are the estimated standard deviations, i.e., 2.7 (0.1) means 2.7±0.1.**
****interpolation value from experimental data.**

The self-diffusion coefficient for heptane inside a (10, 10) SWNT at liquid-like loadings has been computed from EMD simulations. The loading used in the simulations corresponds to a pressure of about 1.5×10^{-3} Torr, as indicated in Figure 47. The calculated value is $8.2\pm1.0\times10^{-4}$

cm^2/s, which is about a factor of 28 larger than D_s for bulk liquid heptane at the same temperature. The fast diffusion of heptane in SWNTs is consistent with results from simulations of other molecules [165, 166, 168] and can be attributed in part to the smooth nature of the surface of SWNT internal channels. In addition, the heptane molecules are more ordered inside a nanotube due to the confinement than in bulk phase. We note that the self-diffusivity of molecules in nanotubes has been shown to dramatically decrease with increasing loading in going from very dilute to liquid-like loadings [147, 162].

Previous simulations have demonstrated that the self-diffusivity of simple molecules in SWNTs in the limit of dilute loadings is dramatically affected by nanotube flexibility [144, 167]. This may also be the case for alkanes. However, self-diffusivities of small molecules at high, liquid-like loadings in flexible and rigid nanotubes are virtually identical, owing to the fact that self-diffusion becomes dominated by adsorbate-adsorbate collisions at high loading [144, 147, 162, 167, 171].

7.5 SUMMARY

At 275 K heptane molecules adsorbed on SWNTs form isolated islands inside open nanotubes. Experimentally measured long-range self-diffusion coefficient for heptane was found to be $D_s = 7.7\times10^{-12}$ cm^2/s in the 0.2 μm thick nanotube sample. Molecular dynamics simulations show that self-diffusion of heptane inside individual nanotubes (*intra-tube* diffusion) is about 8 orders of magnitude faster ($D_s=8.2\times10^{-4}$ cm^2/s). This indicates that the experimentally observed slow diffusion is rate-limited by the exchange of heptane between different nanotubes (*inter-tube* diffusion). The diffusion inside individual nanotubes is also faster than the bulk diffusion at the same temperature (D_s=2.4×10^{-5} cm^2/s), which is likely the result of molecular ordering inside nanotubes due to confinement.

We explain the slow inter-tube diffusion by the presence of significant potential barriers for the molecules migrating between different tubes. They are most likely the barriers at the points of entry into the nanotube interior, and the desorption-adsorption barriers for the transport of molecules between different bundles in the nanotube bulk.

8.0 A VIBRATIONAL SPECTROSCOPIC STUDY OF CF_4 ADSORPTION ON THE EXTENAL AND INTERNAL SURFACES OF OPENED CARBON NANOTUBES[9]

Infrared spectroscopy has been used to make the first experimental discrimination between molecules bound by physisorption on the exterior surface of carbon single-walled nanotubes (SWNTs) and molecules bound in the interior. In addition, the selective displacement of the internally bound molecules has been observed as a second adsorbate is added. SWNTs were opened by oxidative treatment with O_3 at room temperature, followed by heating in a vacuum to 873 K. It was found that, at 133 K and 0.033 Torr, CF_4 adsorbs on closed SWNTs, exhibiting its ν_3 asymmetric stretching mode at 1267 cm^{-1} (red shift relative to the gas phase, 15 cm^{-1}). Adsorption on the nanotube exterior is accompanied by adsorption in the interior in the case of opened SWNTs. Internally bound CF_4 exhibits its ν_3 mode at 1247 cm^{-1} (red shift relative to the gas phase, 35 cm^{-1}). It was shown that, at 133 K, Xe preferentially displaces internally bound CF_4 species, and this counterintuitive observation was confirmed by molecular simulations. The confinement of CF_4 inside single-walled carbon nanotubes does not result in the production of lattice modes that are observed in large 3D ensembles of CF_4.

---

[9] This chapter is reproduced with modifications from: O. Byl, P. Kondratyuk, S.T. Forth, S.A. FitzGerald, L. Chen, J.K. Johnson, J.T. Yates, Jr.; Adsorption of CF_4 on the internal and external surfaces of opened single-walled carbon nanotubes: a vibrational spectroscopy study. J. Am. Chem. Soc. (2003), 125, 5889-5896. The author's contribution centered on the interpretation and modeling of the IR spectrum of CF_4 on SWNTs in terms of two sets of Fermi resonance-split peaks.

8.1 INTRODUCTION

The synthesis of SWNTs normally produces closed structures where each tube is terminated by an end cap, which prevents adsorption within the interior [7, 187]. Oxidative chemical treatments [59, 188] must be applied to the closed SWNTs to open the end caps to access the interior of the nanotubes [56]. While oxidation in solution [HNO_3 + H_2O_2 + H_2SO_4] has been found to be effective for opening closed SWNTs, we have developed a gas-phase ozone oxidation process, which is more easily controlled. This O_3 oxidation procedure has been extensively investigated by IR spectroscopy in previous studies [60, 189]. Oxidation can remove the end caps of individual SWNTs as well as produce or enlarge vacancy defects on the nanotube walls. Both carbonyl groups and C-O-C functional groups are known to form at the rims and at defective wall sites by oxidation [56, 58, 60]. Heating to 773-1073 K removes these blocking groups (by evolution of CO and CO_2 [54]), leaving open entry ports for gas adsorption into the interior [57].

Adsorption in the interior of a nanotube may also be accompanied by adsorption on the exterior surface under appropriate conditions of temperature and pressure [45, 47, 93, 190-193]. The study described in this chapter provides the first experimental detection of adsorbed molecules on both the interior and exterior sites on opened SWNTs as well as a method for selective displacement of the internally bound adsorbed molecules. This has been done by working at cryogenic temperatures and observing the adsorbed probe molecule by transmission infrared spectroscopy. It has been found that the vibrational mode observed is red shifted due to interaction with the nanotube surface. The red shift for interior molecules is larger than the shift for exterior adsorbed molecules.

Confinement of CF_4 in pseudo-one-dimensional condensed structures inside the nanotubes used here does not result in the production of longitudinal optical (LO) and transverse optical (TO) lattice modes observed in 3D clusters of CF_4.

We have employed $CF_4(g)$ as a probe molecule for adsorption on opened single-walled nanotubes [93, 190]. CF_4 exhibits an intense triply degenerate asymmetric stretching mode at 1282 cm^{-1} [194]. Its almost spherical shape and polarizability (3.84 $Å^3$) are similar to that of Xe (4.04 $Å^3$), which was used in earlier experiments [50, 54, 56, 57]. The similar properties of CF_4 and Xe make them ideal for interesting adsorbed CF_4 displacement experiments [195] to be reported in this work.

8.2 EXPERIMENTAL SECTION

A. Single-Walled Carbon Nanotubes. The SWNTs obtained from Professor R. Smalley's group, Rice University, Houston, TX, were produced by means of the pulsed laser vaporization technique. The synthesis and purification of the SWNTs used here are dealt with in more detail in Section 2.3. About 25 μg of SWNTs was deposited onto CaF_2 powder pressed into a tungsten grid. The surface density on the sample was ~65 $\mu g/cm^2$.

B. Vacuum System and IR Cell. This experiment was performed in a high vacuum system equipped with an infrared spectrometer. The stainless steel system is pumped by a 60 L/s turbomolecular pump and a 20 L/s ion pump. The pressure was measured with an ionization gauge (10^{-10}-10^{-4} Torr range) and a capacitance manometer (10^{-3}-10^{3} Torr range). The system base pressure was 10^{-7} Torr after 20 h of baking out at 430-455 K. A UTI 100C quadrupole mass spectrometer was used for leak checking and monitoring the gas composition in the system.

Figure 48 shows the vacuum cell used for transmission IR studies. The cell is connected directly to the gas line. The SWNT sample is supported on the surface of a CaF_2 spot produced from CaF_2 powder hydraulically pressed at 15000 psi into a tungsten sample support grid. A second CaF_2 spot is used as the reference. The grid is stretched between nickel clamps, which are electrically and thermally connected to copper power leads that enter the cell through a liquid N_2 cooled re-entrant dewar. The grid temperature range is 90 to ~1500 K. Temperature is measured with a type K thermocouple spot-welded to the top of the grid. Thermal control is accomplished electronically using LabView software, permitting accurate temperature programming as well as temperature stability to ~0.1 K at the temperature of 133 K, the adsorption temperature employed in this work.

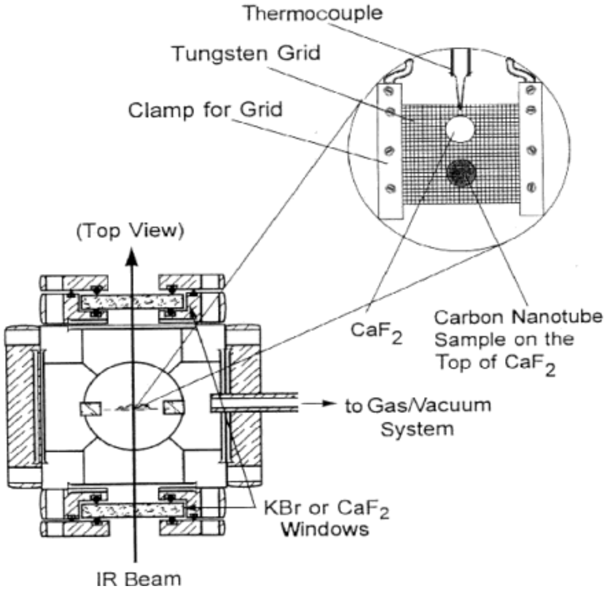

Figure 48. Transmission IR cell-cross-section. The cell is moved by means of horizontal and vertical Newport linear activators allowing precise alignment of the IR beam onto desired section of the sample grid.

When there is an equilibrium pressure of CF_4 in the cell (millitorr range), slight warming of the sample by thermal conduction through the gas phase occurs. This warming effect is automatically compensated by a slight reduction in heating power to the grid, achieving excellent temperature regulation. A temperature gradient in the gas phase results in a slight gas density gradient as one moves vertically along the sample support grid. Thus, subtraction of the gas-phase spectrum (in comparing sample and reference spectra) is not perfect, and a small gas-phase CF_4 IR peak at 1282 cm^{-1} results as well as a small contribution at 1297 cm^{-1} (shoulder) and at 1224 cm^{-1} (shoulder) from CF_4 adsorption on CaF_2.

Condensation of CF_4 occurs on the re-entrant dewar (dewar temperature 77 K) resulting in an equilibrium vapor pressure of CF_4 of 3.3×10^{-2} Torr. This is therefore an upper limit of the gas pressure in this experiment. Lower CF_4 adsorption pressures may be achieved by controlled dosing of small quantities of CF_4 gas into the cooled cell.

C. FTIR Measurements. Transmission IR spectra were measured with a Mattson Research Series FTIR spectrometer controlled from a PC. The spectrometer operates in the mid-infrared spectral region from 500 to 4000 cm^{-1} and uses a wide-band MCT detector. All spectra were recorded at 4 cm^{-1} resolution with 500 scans for averaging. The support grid holding the SWNT sample in the adsorption cell could be accurately positioned horizontally and vertically (to 5 μm) in the IR sample compartment using computer-controlled drivers. IR spectra were recorded as follows: (1) SWNTs on a CaF_2 support; (2) CaF_2 support; (3) gas phase through the empty grid. In each case the spectra were ratioed to background spectra taken without CF_4 in the system.

Prior to each adsorption experiment a background set of spectra were measured. Upon adsorption of CF_4 a second set of spectra were measured and ratioed to the background. Then appropriate differences were taken to obtain the spectrum of CF_4 adsorbed on the SWNT sample.

D. Controlled Oxidation Using Ozone. The SWNT sample was heated in a vacuum to 873 K to remove the majority of the oxidized surface functionalities produced by the

HNO_3/H_2SO_4 purification process and was then subjected to a series of O_3 exposures, followed by annealing to 873 K in vacuum. This cyclic oxidation/annealing procedure has previously been found to open the SWNT caps completely and to enhance the adsorption kinetics into the nanotube interior by opening sites on the nanotube walls and rims [54, 56, 57, 59, 60]. The cyclic procedure causes etching of the SWNT sample, and samples so treated are designated as etched.

High-purity O_3 was prepared and purified in an all-glass generator described previously [196]. We have found that O_3 prepared in this manner will partially decompose upon admission to a stainless steel vacuum system. This effect may be minimized by prolonged passivation of the stainless steel surface with O_3 at ~10 Torr pressure. For the experiment shown here, the O_3 treatment was carried out at room temperature in three stages: (stage 1) 30 min at 8 Torr and 298 K; (stage 2) 19 h at 14.3 Torr and 298 K; (stage 3) 18 h at 15.5 Torr and 298 K. As we will show, initial ozonization produced functional groups at the entrance to the tubes, thus blocking adsorption of CF_4 into the interior of SWNTs in agreement with previous Xe adsorption studies [54, 56]. The SWNTs were then opened by removal of the blocking functional groups through heating to 873 K in a vacuum for 30 min. This greatly enhanced the ability of the SWNTs to adsorb CF_4.

E. Xe Displacement Experiment. We employed Xe to preferentially displace adsorbed CF_4 from the nanotube interior. This was done by filling the nanotubes with CF_4 at 3.3×10^{-2} Torr and 133 K. Xe was then added in sequential doses, and the IR spectra of the adsorbed CF_4 were recorded.

F. Gases. CF_4 (99.9% purity) was obtained in a cylinder from Aldrich Chemical Co. and was used without further purification. Xe (99.995%) was obtained from Matheson in a cylinder and was used without further purification.

8.3 SIMULATION METHODS

A. Vibrational Calculations. The vibrational shifts due to adsorption have been investigated theoretically through quantum calculations using the Gaussian 98 software package [197]. Gas-phase spectra of CF_4 were computed at the levels of LDA theory with the 6-31G basis set. The calculated ν_3 asymmetric stretching mode and ν_4 deformation mode frequencies are 1264 and 573 cm^{-1}, respectively. Quantitative agreement between spectra calculated from LDA and experiment is not expected since LDA does not accurately account for electron correlation, which would account for much of the binding energy. We are also limited in accuracy by the size of the model nanotube and the size of the basis set we were able to use. The LDA calculations of CF_4 adsorbed in the model nanotube gave average frequencies for the ν_3 mode and ν_4 mode of 1246 and 571 cm^{-1}, respectively. We have chosen to use a relatively small basis set (6-31G) to make the CF_4-nanotube calculations tractable. The CF_4-nanotube system was modeled by using a small cluster to represent the nanotube. We used three unit cells of a (9,9) SWNT, split the nanotube in half (along the plane of the nanotube axis), and terminated the dangling bonds with hydrogen atoms. The model nanotube fragment contained 40 carbon and 20 hydrogen atoms. The CF_4 molecule was placed a distance of several angstroms from the concave (inside) surface of the nanotube, and the position of the CF_4 molecule was optimized, holding the atoms in the nanotube fixed. Once the optimized geometry was found, we computed the vibrational spectrum. The optimization and frequency calculations were performed at the LDA/6-31G level of theory.

B. Adsorption Calculations. We have computed the equilibrium amounts of CF_4 and Xe adsorbed on carbon nanotube bundles as a function of Xe partial pressure from molecular simulations. The Grand canonical ensemble (constant μVT) Monte Carlo (GCMC) method [198] was used to calculate adsorption isotherms. The GCMC algorithm consists of three types of moves, namely, translation of a single molecule, creation of a new molecule in the simulation cell, and deletion of a molecule. Moves were attempted randomly with probability 0.2 for translation and 0.4 each for creation and deletion. Simulations were typically equilibrated for two million moves, followed by data taken for one million moves. The maximum displacement step size was adjusted during equilibration to achieve approximately a 40% acceptance ratio for translations. We have used the Lennard-Jones (LJ) potential to account for all fluid-fluid and fluid-solid interactions. Parameters for Xe were taken from the literature [199]. The CF_4 molecule was treated as a single spherical particle. The LJ parameters were derived from viscosity data [123] and were previously used in molecular simulations of diffusion in zeolites [200]. The carbon parameters were taken from Steele [120, 201]. Lorentz-Berthelot combining rules were used for the cross-interactions. The LJ potential parameters are given in Table 6, where σ is the molecule diameter in angstroms and ε is the potential well depth such that ε/k is in units of kelvin, where k is the Boltzmann constant. The use of classical potentials to model the nanotube-fluid interactions precludes the modeling of electronic effects, such as the differences between metallic and nonmetallic nanotubes.

Table 6. Lennard-Jones potential parameters used in the simulations.

	Xe-Xe	**CF_4 - CF_4**	**C-C**
σ (Å)	4.1	4.66	3.4
ε/k (K)	222.32	134.0	28.0

Three different nanotube bundles were considered in this work. Two bundles were constructed by randomly placing nanotubes of various diameters in a box and then optimizing the spacing between the nanotubes as described by Simonyan and Johnson [202]. Each of these two bundles contained 18 nanotubes. The third bundle was a perfect 3×3 array of (10,10) nanotubes. The numbers of each type of nanotube in each bundle are given in Table 7. Using the nomenclature of Table 7, bundles 1 and 2 are representative of heterogeneous bundles, i.e., bundles with a heterogeneous distribution of nanotube diameters. Bundle 3 is a homogeneous bundle since all nanotubes have the same diameter. Experimentally produced nanotubes are heterogeneous. Comparison of simulations on these two classes of bundles will serve to characterize any qualitative differences between adsorption on homogeneous and heterogeneous bundles. Smoothed potentials were used for the nanotubes in the bundles to increase the simulation efficiency. We have found that smoothing the potential has no effect on the adsorption isotherms [50]. The nanotubes in the simulation cell were all aligned in the z direction, and the lengths of the nanotubes were about 60 Å. The bundle was placed in a parallelepiped simulation cell that was 200 Å on a side in the x and y directions. Periodic boundary conditions were applied in all directions, and the potential cutoff was set to 25 Å. The size of the cell in the x and y directions was large enough so that the bundle was isolated (no periodic image interactions).

Table 7. Number and types of nanotubes used in the three different bundles.

Bundle	**Number of (8,8) tubes**	**Number of (9,9) tubes**	**Number of (10,10) tubes**	**Number of (11,11) tubes**	**Number of (12,12) tubes**	**Average Nanotube Diameter (Å)**
1	2	2	10	2	2	13.56
2	4	10	2	2	0	12.35
3	0	0	9	0	0	13.56

8.4 RESULTS

A. Development of the CF_4 IR Spectrum upon SWNT Etching by O_3. Figure 49 shows a typical set of IR spectra obtained in these measurements and the results of taking appropriate differences to derive the IR spectrum of CF_4 adsorbed on the SWNT sample. The CaF_2 support exhibits a significant contribution to the composite IR spectrum due to CF_4 adsorption on its surface, as seen in spectrum (b). Additional IR absorbance due to CF_4 is observed for the SWNT sample, supported on CaF_2, as shown in spectrum (a). Subtraction leads to spectrum (c), where contributions from adsorbed CF_4 on the SWNT sample are observed, along with small features due to incompletely compensated gas-phase CF_4. The prominent uncompensated gas-phase spectral feature is shown as a dashed peak centered at 1282 cm^{-1}.

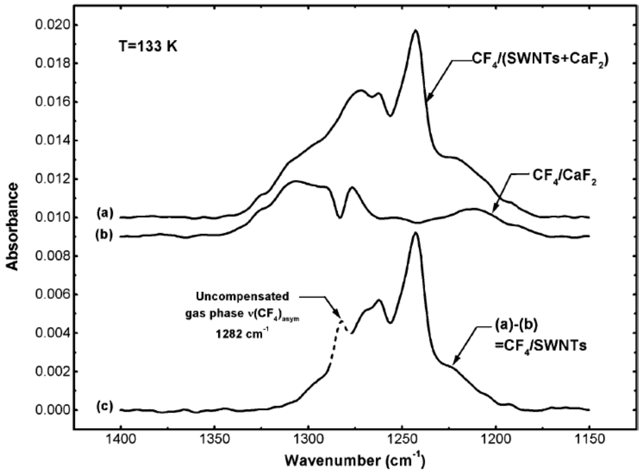

Figure 49. Procedure for spectral subtraction for CF_4 adsorbed at 133 K and 3.3×10^{-2} Torr.

Figure 50 shows the infrared spectrum of adsorbed CF_4 as increasing amounts of etching take place through repeated exposures to O_3, followed by heating. Three etch cycles are presented. As the etching proceeds, enhanced IR intensity due to adsorbed CF_4 is observed to occur at frequencies below 1275 cm^{-1}.

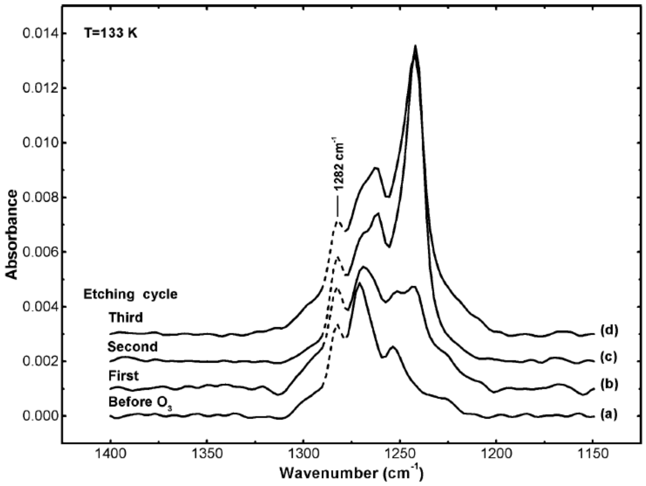

Figure 50. Development of CF_4 IR spectra during cycles of O_3-induced oxidation followed by heating to 873 K for 30 min. in vacuum. Pressure of CF_4 equaled 3.3×10^{-2} Torr.

Figure 51 shows a comparison of the development of the IR spectrum of CF_4 for increasing coverage on the SWNT sample before etching by O_3 and after three cycles of etching. Note that the absorbance scales differ by a factor of 2 for the spectral presentations. The spectra show the effects of increasing equilibrium pressures of CF_4, established at a sample temperature of 133 K. The spectra shown in Figure 51A for the unetched SWNTs contain only two prominent spectral features for adsorbed CF_4 at 1272 and 1253 cm^{-1}. For the etched SWNT sample (Figure 51B), in addition to the spectral features observed in Figure 51A, an additional pair of absorption bands are observed at 1262 and 1242 cm^{-1}. As will be discussed later, the pairs of bands observed at different frequencies for the unetched and etched nanotubes are due to the Fermi resonance of the strong infrared-active ν_3 mode and the first overtone of the ν_4 mode, designated $2\nu_4$.

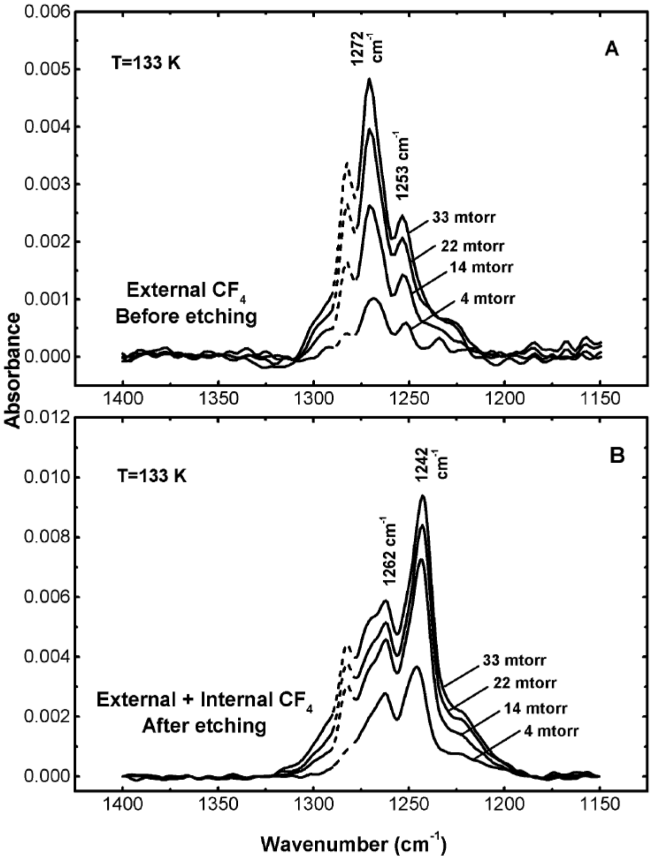

Figure 51. Development of the CF_4 IR spectra for (A) external sites; and (B) for external plus internal sites.

B. Displacement of Adsorbed CF_4 by Xe. The resolution of the overlapping CF_4 spectral features has been experimentally confirmed through the displacement of CF_4 by Xe. Figure 52 shows a high-coverage spectrum of CF_4 obtained for the etched SWNT sample. Exposure to Xe at 133 K results in the selective disappearance of two IR bands together at 1262 and 1242 cm_{-1}. In contrast, the species responsible for the two bands at 1272 and 1253 cm^{-1} either are not displaced or are more slowly displaced compared to the former band pair. We assign the two bands at 1262 and 1242 cm^{-1} to CF_4 adsorbed in the interior of the etched SWNT sample, and the two bands at 1272 and 1253 cm^{-1} to CF_4 species adsorbed externally on the outer SWNT surface. By varying the sequence of Xe and CF_4 adsorption, it was found that the spectra represent identical equilibrium conditions achieved by gas adsorption in either sequence.

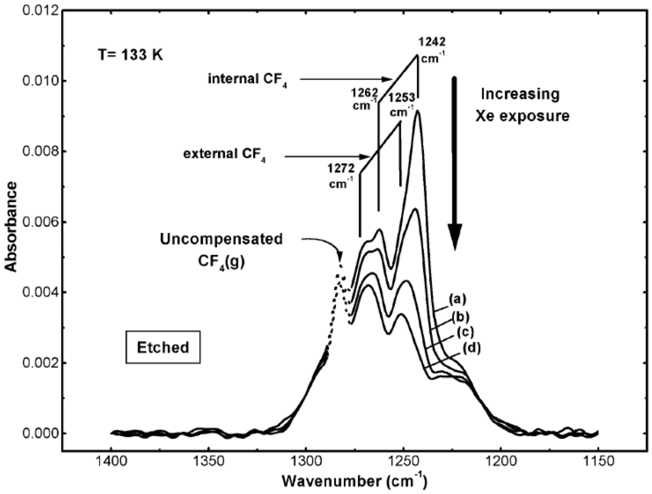

Figure 52. Xenon displacement of adsorbed CF_4. Equilibrium Xe pressure was less than 1×10^{-3} Torr for (a)-(d). The equilibrium pressure of CF_4 was 3.3×10^{-2} Torr for all spectra.

8.5 DISCUSSION

A. Absence of LO-TO Splitting in IR Spectra of CF_4 on SWNTs. The ν_3 mode in CF_4 has an exceptionally high infrared intensity [194]. This gives rise to a strong transition dipole-transition dipole coupling between ν_3 modes of different CF_4 molecules. As a result LO-TO splitting appears in the infrared spectra at high volumetric concentrations of oscillators. The splitting is strongly dependent on the arrangement of the oscillators. We have not observed LO-TO splitting in this work, implying that the concentration of CF_4 molecules inside and on the exterior of the SWNT sample is not sufficiently bulklike to promote lattice mode production.

Figure 53A shows the LO-TO mode splitting evolution in the Raman spectra of CF_4 in an Ar matrix at 84.5 K taken as an example from the work of P. Nextoux et al. [203]. More examples of LO-TO splitting in the vibrational spectra of CF_4 in the condensed phase can be found elsewhere [204-209]. At a very low concentration of CF_4, spectrum (a), two peaks at 1272 and 1257 cm^{-1} caused by the Fermi resonance interaction of ν_3 and 2 ν_4 are observed. The LO-

TO splitting is very small in this case and reported to be 1.4 cm^{-1}. In pure condensed CF_4, spectrum (f), LO-TO splitting reaches 75.0 cm^{-1} with the LO band at 1320 cm^{-1} and TO band at 1245 cm^{-1}.

Figure 53B shows the spectrum of CF_4 adsorbed on unetched and etched nanotubes. The close similarity of the IR spectrum of CF_4 adsorbed on SWNTs before etching to the Raman spectra of CF_4 in an Ar matrix at the lowest concentration (see the inset in Figure 53B) implies that there is a similarly negligible amount of LO-TO splitting in the spectra of CF_4 adsorbed on the external surface of nanotubes at these conditions. No evidence for LO or TO modes can be seen. As the nanotubes are etched the internal surface becomes accessible for adsorption. The IR spectra of CF_4 adsorbed on the etched SWNTs (Figure 53B, upper spectrum) contain features from both the external and the internal CF_4. Although the amount of CF_4 adsorbed has increased somewhat compared to that of unetched nanotubes, the LO mode is not seen and the peak at 1242 cm^{-1} cannot be considered to be the TO band because of its sharpness.

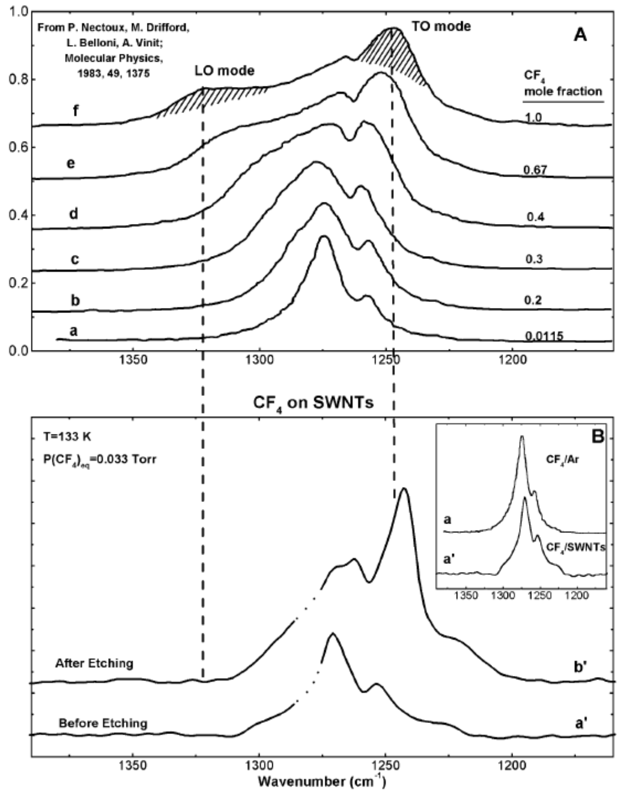

Figure 53. (A) LO-TO splitting evolution in Raman spectra of CF_4 in an Ar matrix at 84.5 K with increasing concentration. (B) Infrared spectra of CF_4 adsorbed at 133 K and 0.033 Torr on unetched and etched SWNTs.

Thus, the mean size of adsorbed CF_4 ensembles on the inner and outer surfaces of the SWNTs must be too small to produce the LO-TO modes characteristic of the condensed phase.

B. Spectra of CF_4 Adsorbed on SWNTs. In vibrational spectroscopy, perturbations between a fundamental and an overtone are frequently encountered, and are known as Fermi resonances [210]. In the case of the CF_4 molecule, the Fermi resonance between the ν_3 mode and the first overtone of the ν_4 mode (2 ν_4) has been observed in a number of studies [211-215]. As a result of the interaction the overtone, usually very weak, borrows intensity from the fundamental band and becomes visible, and at the same time the two bands are shifted further apart. Thus, the presence of a Fermi resonance complicates the appearance of the spectrum, so it is often useful to extract the "unperturbed" positions and intensities of the peaks. This was done in the present study in a way similar to that employed in ref [210]. For the spectra of CF_4 on etched and unetched nanotubes, Lorentzian-shaped profiles of ν_3 and $2\nu_4$ were found that upon numerically calculating the Fermi resonance interaction gave the best fits to the spectra observed.

Figure 54A shows the spectrum of CF_4 on unetched nanotubes, which corresponds to CF_4 adsorbed on the outer surface of nanotubes, and the Lorentzian profiles found for the ν_3 and $2\ \nu_4$ energy level distributions. The fit calculated from these two distributions approximates the experimental data well. The presence of the $2\nu_4$ energy level redistributes the intensity of ν_3 in the spectrum, creating an additional feature at 1253 cm^{-1} and a “hole” (sometimes referred to as the Evans hole in the literature) at 1257 cm^{-1}. Note that, for CF_4 molecules bound to the SWNTs exterior, the ν_3 level is located to the higher frequency side of $2\nu_4$.

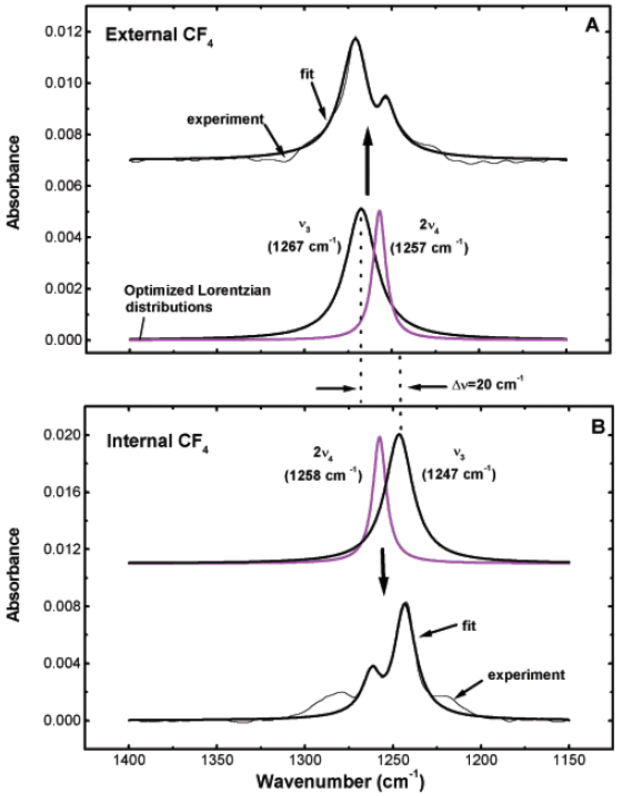

Figure 54. Fermi resonance interaction of the fundamental ν_3 mode with the $2\nu_4$ mode for external and internal CF$_4$ species on SWNTs. The fit was numerically calculated from the Lorentzian distributions, which were iteratively optimized for the fit to match the experimental spectrum. The interaction strength parameter was allowed to vary slightly to fit the data. It is 6.3 and 7.6 cm^{-1} for unetched (A) and etched (B) samples, respectively.

CF$_4$ on etched nanotubes should be adsorbed on both the outer surface and the inner surface, made accessible by the etching, whereas the spectrum for unetched nanotubes only contains the contribution from the outer CF$_4$. To find the spectrum of only the inner CF$_4$, one thus needs to subtract the spectrum for the unetched nanotubes from the spectrum for the etched nanotubes. As some of the SWNT surface is destroyed in the process of etching with ozone, the spectrum from the unetched nanotubes has to be multiplied by a coefficient smaller than 1 before the subtraction is carried out. We used a value of 0.75, chosen on the basis of the goodness of the fit to the resulting spectrum. It corresponds to the destruction of 25% of the outer surface during ozonation. Figure 54B shows the spectrum of CF_4 adsorbed on the inner surface of nanotubes resulting from this subtraction and the Lorentzian distributions of ν_3 and $2\nu_4$ that give the best fit to the data. The most striking difference when compared to the external CF_4 distributions (Figure 54A, bottom) is that ν_3 shifts by 20 cm^{-1} to the red (now ν_3 is to the lower energy side of $2\nu_4$), whereas $2\nu_4$ does not change its position. The reason for the shift of ν_3 is the stronger interaction of the molecule with the surface when it is adsorbed in the interior of the nanotube. The LDA calculation also shows that the ν_3 band is much more prone to shift when the molecule's environment changes than the $2\nu_4$ mode (as judged from the ν_4 fundamental). The calculation indicates that, for the CF_4 molecule adsorbed in the interior of the nanotube, the ν_3 mode shifts by about -20 cm^{-1} compared to that in the gas phase, whereas the shift for ν_4 is only -2 cm^{-1} corresponding to a $2\nu_4$ shift of about -4 cm^{-1}.

This analysis of the experimental spectra shows that the shift for the ν_3 mode of CF_4 compared to gas-phase CF_4 is -15 cm^{-1} for CF_4 molecules bound to the nanotube outer surface and -35 cm^{-1} for CF_4 molecules bound in the interior.

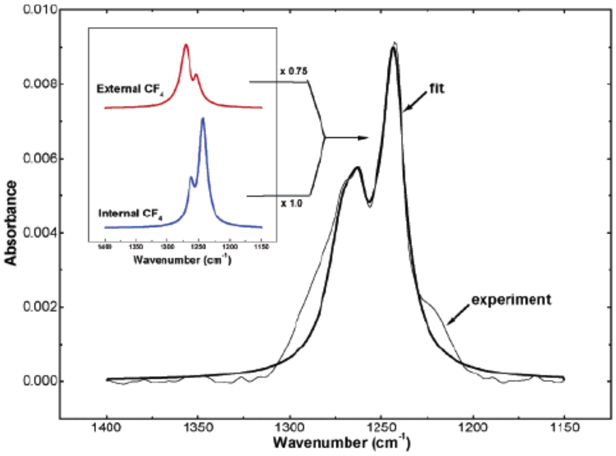

Figure 55. Simulation of combined external and internal CF_4 spectra on SWNTs.

Figure 55 shows the addition of the fits for the external and internal CF_4 spectra, resulting in a fit for the total composite spectrum of CF_4 adsorbed on etched nanotubes. The coefficient of

0.75 is employed during addition. The shift of the ν_3 mode to lower wavenumbers is in accordance with the red shift often observed for physically adsorbed species and for species bound inside inert matrixes. The band associated with the smaller ν_3 red shift is assigned to externally bound CF_4 molecules on this basis as well as on the basis of comparison of CF_4 spectra on etched and unetched nanotubes, and the band associated with the larger wavenumber shift is assigned to internally bound CF_4, where a stronger interaction would be expected.

C. Modeling of Xe Displacement of Adsorbed CF_4 from SWNTs. The displacement of CF_4 by Xe confirms the presence of four IR bands for the adsorbed CF_4 species present on both the exterior and interior sites. It is seen in Figure 52 that Xe preferentially displaces internal CF_4 species, causing the bands at 1262 and 1242 cm^{-1} to disappear first as the Xe coverage is increased. The displacement experiments probe the thermodynamic factors responsible for Xe-CF_4 site exchange under equilibrium conditions, since similar infrared spectra are observed for either order of adsorption of CF_4 and Xe. We know that Xe is thermodynamically favored as an internally bound species compared to CF_4, causing preferential CF_4 displacement by Xe from the SWNT interior. We have performed molecular modeling of CF_4 and Xe coadsorption to observe whether preferential CF_4 displacement occurs for the internally bound CF_4 compared to externally bound CF_4. Classical GCMC simulations were performed at 133 K, a constant partial pressure of CF_4 of 3.3×10^{-2} Torr, and various values of Xe partial pressure. Simulations were performed on each of the three model bundles described in Table 7. The results from two simulations on heterogeneous and homogeneous bundles are shown in Figures 56 and 57, respectively. Simulations on the three different types of bundles are qualitatively similar. In each case Xe begins to adsorb inside the nanotubes, displacing CF_4, at pressures below where there is appreciable Xe adsorption in the grooves on the external surface of the nanotubes. The partial pressure at which Xe begins to displace internal CF_4 is about 10^{-5} Torr. Xenon starts to adsorb on the outside of the nanotubes at about 10^{-4} Torr for the heterogeneous bundle and about 10^{-3} Torr for the homogeneous bundle. It is interesting to note that, even after Xe begins to adsorb on the outside of the nanotubes, very little CF_4 is displaced by the Xe, even at the highest Xe partial pressure simulated (10^{-2} Torr). This observation agrees with the experimental results showing that the CF_4 modes associated with adsorption inside the nanotube disappear in a facile manner, while the IR peaks for external adsorption are not substantially attenuated by Xe adsorption. The reason for this can be easily seen by observing snapshots of the simulation. Figure 58 shows snapshots for adsorption on exterior sites of bundle 3 at Xe partial pressures of 10^{-3} (left) and 5×10^{-3} (right) Torr, both with a CF_4 partial pressure of 3.3×10^{-2} Torr. Note that at the lower Xe partial pressure there are a number of CF_4 molecules (shown in red) but only one Xe atom (blue). Note also that CF_4 does not fill all the available external sites at this pressure. Hence, at the higher pressure (right) we observe a dramatic increase in the concentration of Xe atoms in the groove sites, while the number of CF_4 molecules remains almost constant. The first Xe atoms to adsorb onto the external sites simply occupy empty sites rather than replacing CF_4 molecules. At pressures higher than those sampled experimentally, Xe does displace CF_4 on the external sites. This explains why external CF_4 species responsible for the bands at 1272 and 1253 cm^{-1} persist at all experimental Xe doses.

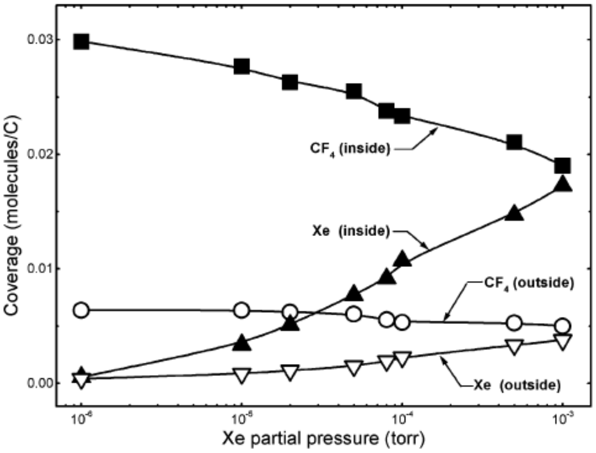

Figure 56. Simulated equilibrium adsorption uptake of CF$_4$ and Xe (per carbon atom) on heterogeneous nanotube bundle 1 (see Table 7) at 133 K as a function of Xe partial pressure. The CF$_4$ pressure is held constant at 3.3×10^{-2} Torr. Squares (circles) represent the loading of CF$_4$ molecules inside (outside) the nanotubes and up triangles (down triangles) represent Xe adsorption inside (outside) the nanotubes. Lines are drawn to guide the eye. The estimated statistical errors are on the order of the symbol sizes.

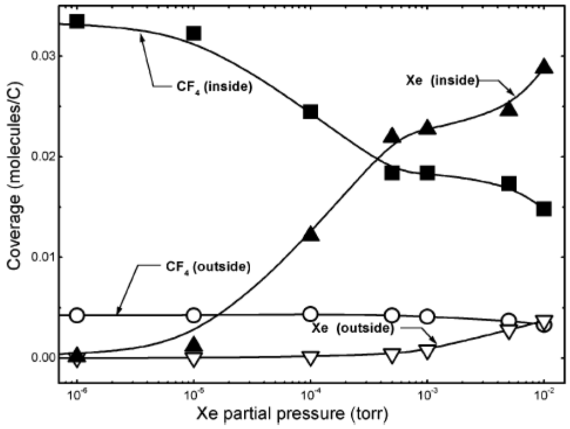

Figure 57. Simulated equilibrium coverage of CF$_4$ and Xe (expressed per carbon atom) on homogeneous nanotube bundle 3 (see Table 7) at 133 K as a function of Xe partial pressure. The CF$_4$ pressure is held constant at 3.3×10^{-2} Torr. The symbols are the same as in Figure 56. The lines are drawn to guide the eye.

Molecular simulations show that Xe and CF$_4$ only adsorb inside the nanotubes and on the external groove of the perfectly packed homogeneous bundles (bundle 3). The interstitial channels in homogeneous bundles of (10,10) nanotubes are too small to allow adsorption of either gas. However, the heterogeneous bundles do not pack perfectly and hence have a few larger interstitial sites for gas adsorption. Simulation snapshots from homogeneous and heterogeneous bundles are shown in Figure 59. Most of the interstitial channels in the heterogeneous bundle (right) are too small to accommodate adsorption of either Xe or CF_4. However, there are a few interstices that are large enough to facilitate Xe, but not CF_4, adsorption and other channels that are large enough to accommodate either molecule. This explains why the heterogeneous bundles (Figure 56) exhibit external Xe adsorption at lower pressures than the homogeneous bundles (Figure 57). Adsorption in the interstitial channels is counted as external site adsorption so that the upturn in external Xe site adsorption shown in Figure 57 is a result of Xe inside the interstitial channels. We expect that the nanotube bundles studied experimentally behave more like the heterogeneous bundles than the perfectly packed bundles, giving rise to some interstitial adsorption.

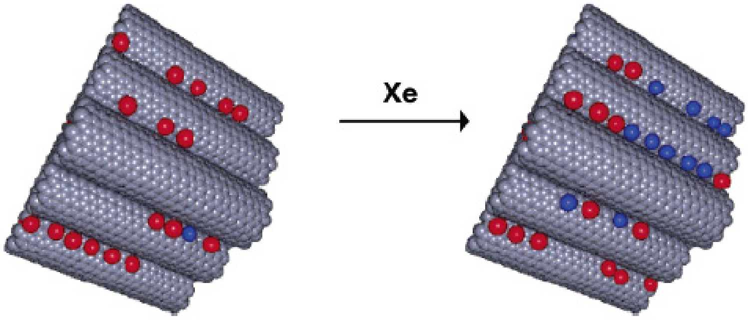

Figure 58. Simulation snapshots for CF_4-Xe coadsorption on the external groove sites at a Xe partial pressure of 10^{-3} Torr (left) and 5×10^{-3} Torr (right). In both cases the CF_4 pressure is 3.3×10^{-2} Torr. Note that the number of Xe atoms (blue) increases dramatically with increasing Xe partial pressure, while the number of CF_4 molecules (red) decreases only slightly.

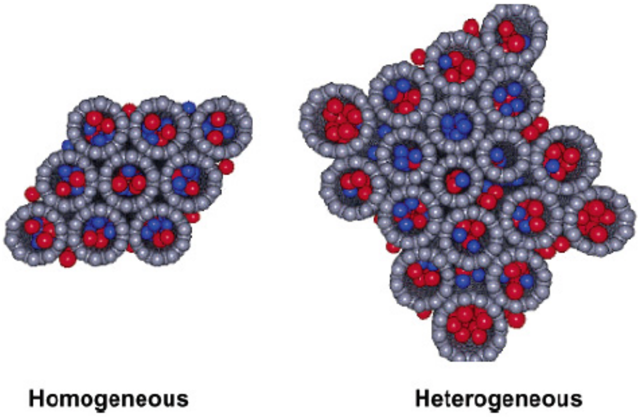

Figure 59. Simulation snapshots for CF_4-Xe coadsorption on homogeneous bundles (left) and on heterogeneous bundles (right). Note that the interstitial channels in the homogeneous bundle are too small to allow adsorption of either Xe or CF_4. The interstitial channels in heterogeneous bundles, such as bundle 1 from Table 7 shown here (right), have some larger interstitial channels that allow adsorption of Xe and CF_4.

8.6 SUMMARY

The following results have been obtained in our study of CF_4 adsorption on unetched SWNTs and etched SWNTs.

(1) The adsorption of CF_4 on SWNTs at 133 K occurs on two adsorption sites: internal and external. On closed SWNTs, CF_4 adsorbs only on the external sites, whereas on opened SWNTs, CF_4 adsorbs on both external and internal sites.

(2) Adsorbed CF_4 on external sites of SWNTs manifests itself by two IR bands, at 1272 and 1253 cm^{-1}. CF_4 adsorbed on internal sites exhibits two bands at 1262 and 1242 cm^{-1}. The presence of two bands in both cases results from the Fermi resonance of the strong infrared-active ν_3 fundamental with the first overtone of the ν_4 mode.

(3) The larger shift from the gas-phase frequency of the ν_3 mode of internal CF_4 (shift -35 cm^{-1}, -2.7%) compared to the external CF_4 (shift -15 cm^{-1}, -1.2%) is due to the stronger interaction of CF_4 with the interior walls of SWNTs.

(4) Xe preferentially displaces CF_4 adsorbed inside SWNTs as observed both experimentally and in equilibrium simulations.

(5) The confinement of CF_4 inside the single-walled nanotubes in pseudo-one-dimensional structures does not result in production of LO and TO lattice modes characteristic of large 3D ensembles of CF_4 in crystallized CF_4.

9.0 ANALYTICAL FORMULAS FOR FERMI RESONANCE INTERACTIONS IN CONTINUOUS DISTRIBUTIONS OF STATES[10]

Fermi resonance interaction between a distributed fundamental vibrational level and a distributed overtone is considered. The overtone is assumed to be spectrally inactive. Simple analytical expressions are derived for the resulting spectral profile in terms of the distribution functions for the fundamental and overtone. The formulas enable straightforward modeling of spectra with Fermi resonances.

9.1 INTRODUCTION

Fermi resonances occur frequently in vibrational spectra. The perturbation of the spectral bands caused by the Fermi resonance between two vibrational levels is well understood and can be satisfactorily modeled in instances when the levels are well localized as far as their energies are concerned [216]. However, in many practical situations bands have non-negligible widths, that is, vibrational levels are distributed over a finite energy range. This broadening can be caused by intermolecular interaction (especially for H-bonding molecules), short excited state lifetimes,

---

[10] This chapter is reproduced with modifications from: P. Kondratyuk; Analytical formulas for Fermi resonance interactions in continuous distributions of states. Spectrochimica Acta (2005), 61A, 589-593.

interaction of vibrational modes with phonons, etc. [217]. In cases like these the equations governing the perturbation for the localized levels cannot be used. Aside from the full quantum-mechanical approach (e.g. [218]), the solution, as described by Scherer [210], is to approximate the distributions of the interacting vibrational states as collections of discrete levels, and then calculate the contribution of each pair of levels from the two distributions. The end spectrum is then the sum of all such contributions. While workable, this approach normally requires the use of a programming language, as well as an understanding of the particular implementation that underlies the algorithm.

The current paper presents analytical formulas that can be used to calculate the resulting spectrum from given distributions of the two levels. The advantages are the usual ones associated with the use of analytical forms. Practically any available multi-purpose mathematics software can be employed with these formulas (such as MathCad®, Mathematica® etc.).

9.2 THEORY

Fermi resonances appear whenever a fundamental vibrational level lies closely in energy to an overtone (or combination) level with the same wavefunction symmetry [216, 219]. The two levels are allowed to interact due to the presence of anharmonic terms in the Hamiltonian, and, consequently, the strength of such an interaction will depend on the magnitude of the normal modes' anharmonicity constants [220]. The two original levels mix as a result of the resonance, producing two new levels with spectral intensity of the fundamental distributed between them. Since the overtone is spectrally inactive (or extremely weak) by itself, the resonance leads to the appearance of an additional peak in the spectrum. This is sometimes viewed as the overtone "borrowing" intensity from the fundamental and becoming visible. A well-known example of Fermi resonance is the presence of two bands in the N-H stretching region of polyamides [221, 222], where the two interacting modes are the N-H stretch fundamental and the first overtone of the N-H deformation mode. Vibrational spectrum of CF_4 in the asymmetric stretch region (Figure 60) also shows a Fermi resonance. It comes from the interaction of the asymmetric stretching mode and the overtone of a deformation mode [100, 203].

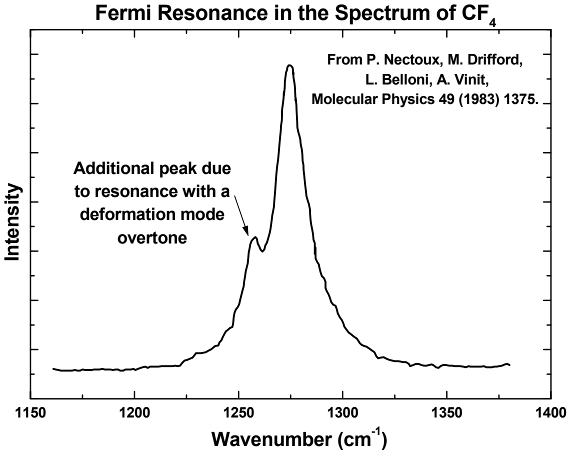

Figure 60. Fermi resonance in the Raman spectrum of CF_4 in liquid Ar at 84.5 K (from [203]). The weaker band on the low-frequency side of the asymmetric stretch fundamental is due to the resonance with the overtone of the deformation mode at 632 cm^{-1}.

A large amount of experimental and theoretical work has been devoted to Fermi resonances in the vibrational spectra of hydrogen-bonded compounds, especially water and hydrates [210, 215, 218, 223, 224], where such resonances are both common and pronounced.

The interaction between the fundamental and the overtone can be viewed as a perturbation of the original non-interacting system [216]. According to the standard first order perturbation treatment, the new eigenstates of the system can be expressed as linear combinations of the old states:

$$\Psi_1 = \beta\varphi_1 + \sqrt{1-\beta^2}\varphi_2 , \ \Psi_2 = \sqrt{1-\beta^2}\varphi_1 - \beta\varphi_2 , \qquad (1)$$

where φ_1 and φ_2 are the original wavefunctions, Ψ_1 and Ψ_2 are the new wavefunctions, and β is the mixing coefficient. The new energy eigenvalues of the system can be found by solving the secular equation

$$\begin{vmatrix} E_1 - E & w \\ w & E_2 - E \end{vmatrix} = 0 , \qquad (2)$$

where E_1 and E_2 are the energies of states φ_1 and φ_2, E represents the new energy levels of the system, and the off-diagonal element w is the cross-interaction energy that determines the interaction strength between the two original levels. The solution for (2) is

$$E = \frac{1}{2}(E_1 + E_2) \pm \frac{1}{2}\sqrt{(E_1 - E_2)^2 + 4w^2} \ . \qquad (3)$$

Figure 61 schematically shows the effect of the resonance on two infinitely narrow vibrational modes in a spectrum. State **a** is a fundamental possessing spectral intensity, while state **b** is a spectrally inactive overtone. This is shown in the figure by the dark shading of state **a**.

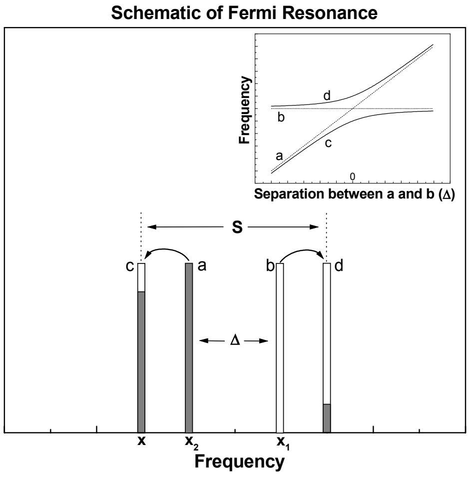

Figure 61. Effect of Fermi resonance on two interacting vibrational states, a and b. a is spectroscopically visible, b is not. Resonance results in two new eigenstates of the system, c and d, that are linear combinations of a and b. Both c and d are spectroscopically visible. Inset: relative location of states as a function of separation between a and b.

Fermi resonance results in the creation of two new eigenstates of the system, states **c** and **d** which, according to (3), are symmetrically displaced with respect to **a** and **b** to a new, larger separation ***S***. From (3), ***S*** is given by

$$S = \sqrt{\Delta^2 + 4w^2}\ , \qquad (4)$$

where **Δ** is the separation between levels **a** and **b**.

The admixture coefficient of **a** in **c** and **d** is [cf. with (1)]

$$f^{a}_{c,d} = \sqrt{\frac{1}{2} \pm \frac{\Delta}{2S}}\ , \qquad (5)$$

with (+) for **c** and (-) for **d**. Both of the new states are spectroscopically active due to admixture of **a**, with spectral intensity proportional to $\left(f^{a}_{c,d}\right)^2$. As can be seen from (5), no spectral intensity is lost or gained when Fermi resonance is taken into account.

Thus, it is straightforward to use expressions (4) and (5) to model Fermi resonances in the case of localized vibrational levels. However, if the levels in question are distributed, the notion of "frequency" of a vibrational band looses its meaning, prohibiting the use of (4) and (5). The next section contains a derivation of analytical expressions that can be employed if one or both of the interacting levels are distributed. Eq. (4) and (5) are the limiting case of those expressions when the width of the interacting distributions approaches zero.

9.3 RESULTS AND DISCUSSION

We assume that the distribution functions of the fundamental (spectroscopically visible) and overtone (invisible) levels are given. We will denote them ***Vis(x)*** and ***Inv(x)*** respectively.

If in Figure 61 state **c** is located at energy x, state **b** – at x_1, then from Eq. (4) we can determine where state **a** must lie in order to contribute to the density of states at x. Equation 4 becomes:

$$2(\frac{x_1 + x_2}{2} - x) = \sqrt{(x_2 - x_1)^2 + 4w^2} , \qquad (6)$$

hence,

$$x_2 = x - \frac{w^2}{x - x_1} . \qquad (7)$$

Equation (7) is quadratic in x. Thus for given x_1 and x_2 there are two values of x that satisfy (7), corresponding to states **c** and **d** in Figure 61, as expected. Now knowing that every point of the resulting spectrum will contain a contribution from every possible x_1, x_2 being determined from Eq. (7), we put together an expression for the resulting spectrum as a sum of all such contributions. Denoting the resulting spectrum $I(x)$, we obtain:

$$I(x) = \int_{-\infty}^{\infty} Vis\left(x - \frac{w^2}{x - x_1} \right) Inv(x_1) dx_1 . \quad (8)$$

The above equation is the expression we seek. Derived from Eq. (4), it automatically satisfies another condition, Eq. (5). This will be shown in the following.

Any function can be thought of as consisting of a large number of delta-functions, in the sense that if this collection of delta-functions is viewed with a finite resolution, it will approach the real function (and all of its properties) as the number of delta-functions in the approximation is increased. Thus, it is sufficient to show that (8) operates in accordance with Eq. (5) for distributions consisting of delta-functions. We will assume that the two distributions, ***Vis(x)*** and ***Inv(x)***, each contain only one delta-function. It can be concluded that the result will apply to distributions containing any number of delta-functions.

We note that if ***Inv(x)*** is a delta-function centered at x_1 (state **b** in Figure 61), then the integral in Eq. (8) can be replaced with just one member of the sum,

$$I(x) = Vis\left(x - \frac{w^2}{x - x_1}\right). \qquad (9)$$

Remembering that ***Vis(x)*** is also a delta-function, positioned, for instance, at x_2 (state **a**), from (9) we obtain that ***I(x)*** consists of two delta-functions, states **c** (at x_c) and **d** (at x_d) in accordance with (4). Although **c** and **d** are both infinitely narrow, the areas under **c** and **d** are different. If the area under ***Inv(x)*** is normalized to unity, then it can be shown that the areas under **c** and **d** are equal to the area under **a** times $\left[\frac{d}{dx}\left(x - \frac{w^2}{x - x_1}\right)\right]^{-1}$, taken at x_c and x_d respectively. Let $\mathbf{A_a}$ be the area under ***Vis(x)***, then

$$A_c = \frac{A_a}{1 + \dfrac{w^2}{(x_c - x_1)^2}} = A_a \cdot \left(\frac{1}{2} + \frac{\Delta}{2S}\right) \text{ and}$$

$$A_d = \frac{A_a}{1 + \dfrac{w^2}{(x_d - x_1)^2}} = A_a \cdot \left(\frac{1}{2} - \frac{\Delta}{2S}\right), \qquad (10)$$

which demonstrates that Eq. (8) agrees with condition (5).

Expression (8) has been verified against the method of Scherer [210]. In all cases the end spectra produced matched exactly when the resolution in the discrete method of [210] was sufficient.

As mentioned in the preceding discussion, a simplified form of Eq. (8), Eq. (9), can be used in the case when the invisible level is localized rather than distributed. Fermi resonances of this type are frequently encountered in spectroscopy and known as Evans holes, because they appears in spectra as characteristic narrow transmission windows in broad peaks [211, 212, 224]. Expression (9) is quite simple in that it only defines a mapping of the frequency axis onto itself.

A form analogous to (9) can be obtained from (8) for the case when the overtone is distributed while the visible level is localized (a situation that is less significant practically). By making the substitution $x_1 \rightarrow x - \frac{w^2}{x - x_2}$ [from Eq. (7)], one obtains another form of (8),

$$I(x) = \int_{-\infty}^{\infty} Vis(x_2) Inv\left(x - \frac{w^2}{x - x_2}\right) \frac{w^2}{(x - x_2)^2} dx_2 . \qquad (11)$$

Then if ***Vis(x)*** is localized at $\boldsymbol{x_2}$ (is a delta-function centered at $\boldsymbol{x_2}$),

$$I(x) = Inv\left(x - \frac{w^2}{x - x_2}\right) \frac{w^2}{(x - x_2)^2} . \qquad (12)$$

Table 8 lists these formulas along with conditions for their use.

Table 8. Expressions for spectral profiles with Fermi resonances in terms of unperturbed distributions *Vis(x)* and *Inv(x)*.

Applicability criteria	Formula	Notes
Both levels are distributed (most general)	$I(x) = \int_{-\infty}^{\infty} Vis\left(x - \frac{w^2}{x - x_1}\right) Inv(x_1) dx_1$	Eq. (8). Same as Eq. (11).
Fundamental level is distributed, overtone is localized	$I(x) = Vis\left(x - \frac{w^2}{x - x_1}\right)$	Eq. (9). x_1 is the position of the overtone.
Overtone is distributed, fundamental is localized	$I(x) = Inv\left(x - \frac{w^2}{x - x_2}\right) \frac{w^2}{(x - x_2)^2}$	Eq. (12). x_2 is the position of the fundamental
Vis(x) and ***Inv(x)*** are the original distributions of the fundamental and the overtone levels respectively. The area under ***Inv(x)*** has to be normalized to 1 for the spectral intensity to be conserved.		

Figure 62 shows two examples of spectra calculated with Eq. (8) and (9). 61(A) is the case when both levels are distributed. The bold line, calculated with (8), is a fit to the experimental spectrum of CF_4 from Figure 60 (shown in the background). The two unperturbed distributions (not to scale with the main graph for clarity) are Lorentzians with positions and widths optimized to give the best fit to the experimental line.

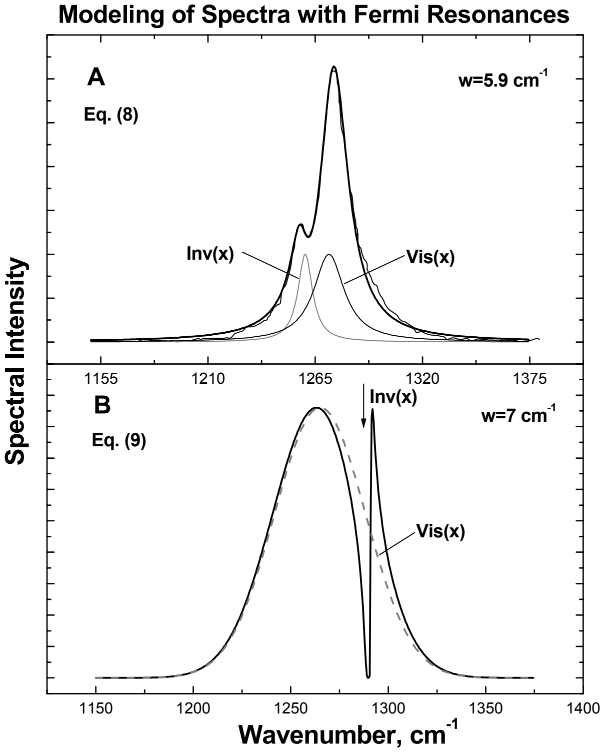

Figure 62. (A) Spectral profile (bold line) calculated with Eq. (8) from two unperturbed Lorentzian distributions (below main graph, not to scale). The positions and widths of the Lorentzians were chosen for the spectrum to fit the experimental profile of CF_4 from Figure 60 (noisy line). (B) Spectrum (bold line) resulting from a Gaussian-shaped fundamental (dashed line) resonating with a localized overtone level at the position indicated by the arrow (1290 cm^{-1}).

Figure 62(B) shows a situation when a visible Gaussian distribution (dashed line) is perturbed by a localized overtone state at x=1290 cm^{-1} (the position indicated by the arrow). Eq. (9) was used. The additional feature due to resonance is much sharper than in the case of a distributed overtone. It should be noted, however, that in practice, the finite resolution of spectrometers smoothens the sharp peaks and dips associated with such a Fermi resonance.

A few remarks can be made regarding the formulas in Table 8. Firstly, it is easy to notice that spectral profiles given by Eq. (9) and (12) are always analytical if the initial distributions of levels can be expressed analytically. Eq. (8) may or may not give an analytical result.

Secondly, if the distributions are given as data points rather than analytical profiles, all of the formulas in Table 8 will work with a suitable interpolation procedure. The integration limits in (8) then can be replaced by the range where the function of the integration variable is defined and non-zero.

9.4 SUMMARY OF RESULTS

In conclusion, analytical formulas are presented that allow easy modeling of Fermi resonances in spectra when either the fundamental level or the overtone or both are distributions rather than localized levels. The formulas are especially simple when only one of the levels is distributed, always producing an analytical spectral profile if the initial distribution can be expressed analytically. Table 8 summarizes the results.

APPENDIX A

CONVERSION EXPRESSIONS FOR QUANTITIES OF PURE AND MIXED 1-HEPTANE AND 1-DEUTEROHEPTANE

This appendix section deals with the conversion formulas needed to calculate the amounts of two mixtures of heptane and deuteroheptane (here referred to as H-mixture and D-mixture) that correspond to certain amounts of heptane and deuteroheptane measured in the experiment (see Chapter 7). The percentage composition of the two mixtures is also known from the experiment. It is determined by analyzing the composition of the adsorbed gas when the sample is positioned either in front of the effusive doser delivering heptane or the doser delivering deuteroheptane.

The experimentally determined amounts of heptane and deuteroheptane will be denoted H_a and D_a respectively. The fraction of heptane in heptane-rich mixture (H-mixture) will be denoted H_{mr}, while the fraction of deuteroheptane in the deuteroheptane-rich mixture (D-mixture) will be denoted D_{mr}. The amounts of H-mixture and D-mixture sought will be denoted H_{ma} and D_{ma}.

As no molecules are lost when we mentally regroup them form pure heptane and deuteroheptane into H-mixture and D-mixture, we can write,

$$H_a + D_a = H_{ma} + D_{ma} \qquad (1)$$

Also, by the above definition of fractions,

$$H_a = H_{ma} \cdot H_{mr} + D_{ma}(1 - D_{mr}) \qquad (2)$$

$$D_a = D_{ma} \cdot D_{mr} + H_{ma}(1 - H_{mr}) \qquad (3)$$

Eqns. (2) and (3) yield

$$D_{ma} \cdot (1 - 2D_{mr}) + D_a = H_a + H_{ma} \cdot (1 - 2H_{mr}) \qquad (4)$$

By substituting in the D_{ma} from Eqn. (1), we obtain the expression for H_{ma}:

$$H_{ma} = H_a \cdot \frac{D_{mr}}{H_{mr} + D_{mr} - 1} + D_a \cdot \frac{D_{mr} - 1}{H_{mr} + D_{mr} - 1} \qquad (5)$$

In an analogous fashion,

$$D_{ma} = D_a \cdot \frac{H_{mr}}{H_{mr} + D_{mr} - 1} + H_a \cdot \frac{H_{mr} - 1}{H_{mr} + D_{mr} - 1} \qquad (6).$$

Eqns. (5) and (6) are the conversion expressions sought.

APPENDIX B

PROPORTIONAL-INTEGRAL-DERIVATIVE TEMPERATURE CONTROL

Proportional-integral-derivative (PID) algorithm [92] was employed in the TPD system to control the temperature of the sample by controlling the ohmic power produced on the tungsten wires supporting the sample (see Chapter 2 for the schematic of the TPD apparatus). The control output of the PID algorithm depends on the deviation of the temperature of the sample T_c from the setpoint temperature T_s and the temporal history of this deviation. Three terms contribute to the control output $S_{out}(t)$:

$$S_{out}(t) = P(t) + I(t) + D(t) \qquad (1)$$

The three terms are called proportional, integral and derivative terms. The first term, P(t), is merely proportional to the temperature deviation, $\Delta T = T_s - T_c$:

$$P(t) = K_p \cdot \Delta T(t) \qquad (2)$$

where K_p is the proportionality constant. The I(t) is the integral term and is given by

$$I(t) = K_i \cdot \int_0^t \Delta T(\tau) d\tau \quad (3)$$

where K_i is the proportionality constant and the integration is carried out over time up to the moment the control output is set. The integral term will keep adjusting the total output as long as there is a deviation from the temperature setpoint. When the integral term is the only term contributing to the control output in the PID algorithm, the temperature of the sample will oscillate around the setpoint. However, if a proportional term is present, for some values of the constants K_i and K_p it will dampen the oscillations and the system will achieve temperature stability at the setpoint. Therefore, the algorithm can potentially work with only these two terms. However, the introduction of the derivative term results in more efficient dampening of the oscillations. The derivative term is given by

$$D(t) = K_d \cdot \frac{\partial(\Delta T)}{\partial t} \qquad (4)$$

where K_d is the proportionality constant. The derivative term counteracts rapid change in the temperature deviation, thereby reducing the time needed to stabilize the temperature.

APPENDIX C

ION BOMBARDMENT MODIFICATION OF SWNT ADSORPTIVE PROPERTIES

We have studied experimentally the effect of high-energy ion irradiation on the adsorption properties of SWNTs. This was done by comparing the TPD spectra of CCl_4 adsorbed on SWNTs before and after ion irradiation.

A number of studies of ion bombardment of fullerenes and carbon nanotubes [225-229] have show that ion irradiation results in significant change of structure in the material at the atomic level. Auger electron spectroscopy indicated that the π-bonding conjugation decreases after irradiation [226].

Figure 63 shows TPD spectra of CCl_4 on untreated material for increasing exposures.

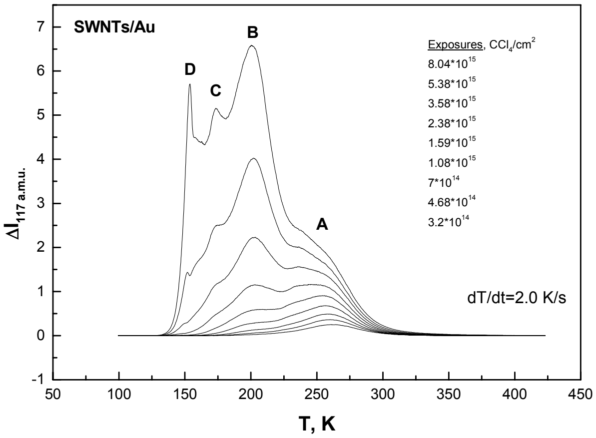

Figure 63. TPD traces for CCl_4 adsorbed on annealed, untreated nanotubes for a range of exposures.

As the exposure increases, the sites with progressively lower binding energy are populated by the adsorbate. We associate sites A with interior nanotube sites, sites B with groove sites and sites C with exterior nanotube surface. The D feature corresponds to multilayer desorption and is not associated with any SWNT adsorption sites.

The comparison of CCl_4 TPD spectra at one of the exposures ($\sim 7\times10^{14}$ molecules cm^{-2}) before and after irradiation with 3 keV Ar^+ is given in Figure 64. 2.4×10^{17} ions in total were delivered during the first exposure to the ions, while the second exposure involved additional dosing of 3.0×10^{17} ions. We believe that about 10-30% of these ions were intercepted by the sample.

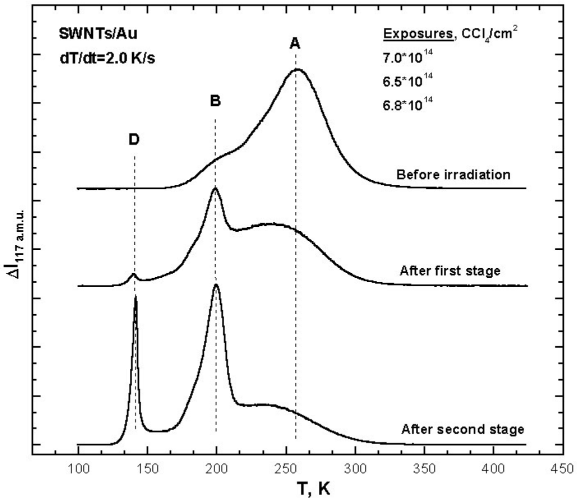

Figure 64. Changes in the TPD spectra of CCl_4 adsorbed on SWNTs after they were irradiated by 3 keV Ar+ ions. The irradiation was performed in two stages, with TPD spectra of CCl_4 taken after each of them.

It can be seen that before irradiation all the adsorbate is in the nanotube interior sites (site A). The groove sites (site B) feature is only a shoulder on the broader interior site peak. The multilayer peak (site D) is completely absent. After the first stage of irradiation the interior peak decreases in intensity, and the adsorbate is displaced into the groove sites. After the second stage of irradiation, hardly any of the interior site capacity remains and the adsorbate is adsorbed mostly on the groove sites and in the multilayer. Even though the occupancy of the groove sites is increased, this fact does not indicate that the number of the groove sites increased. Rather, it is a consequence of the decrease in the number of available interior sites. The number of available groove sites also decreases, as witnessed by the increase in the amount of adsorbate in the multilayer.

We tentatively attribute the destruction of the available interior surface area to the amorphization and graphitization of the nanotubes by the energetic Ar^+ ions. Once the hollow structure of the nanotubes is destroyed, the area available for adsorption drops dramatically due to the denser structure of the resulting material.

BIBLIOGRAPHY

[1]. Iijima, S. *Nature* **1991**, *354*, 56.

[2]. Masenelli-Varlot, K.; McRae, E.; Dupont-Pavlovsky, N. *Applied Surface Science* **2002**, *196*, 209.

[3]. Burchell, T. D. *Carbon materials for advanced technologies*, 1st ed.; Pergamon: Amsterdam ; Oxford, 1999.

[4]. Osawa, E. *Kagaku* **1970**, *25*, 854.

[5]. Bovchar, D. A.; Galperkin, E. G. *Dokl. Acad. Sci. SSSR* **1973**, *209*, 610.

[6]. Kroto, H. W.; Heath, J. R.; O'Brian, S. C.; Curl, S. C.; Smalley, R. E. *Nature* **1985**, *318*, 162.

[7]. Dresselhaus, M. S.; Dresselhaus, G.; Eklund, P. C. *Science of fullerenes and carbon nanotubes*; Academic Press: San Diego, 1996.

[8]. Dresselhaus, M. S.; Dresselhaus, G.; Saito, R. *Carbon* **1995**, *33*, 883.

[9]. Saito, R.; Dresselhaus, G.; Dresselhaus, M. S. *Physical properties of carbon nanotubes*; Imperial College Press: London, 1998.

[10]. Saito, R.; Fujita, M.; Dresselhaus, G.; Dresselhaus, M. S. *Applied Physics Letters* **1992**, *60*, 2204.

[11]. Ajayan, P. M.; Iijima, S. *Nature* **1992**, *358*, 23.

[12]. Dresselhaus, M. S. *Nature* **1992**, *358*, 195.

[13]. Iijima, S.; Ichihashi, T. *Nature* **1993**, *363*, 603.

[14]. Bethune, D. S.; Kiang, C. H.; Devries, M. S.; Gorman, G.; Savoy, R.; Vazquez, J.; Beyers, R. *Nature* **1993**, *363*, 605.

[15]. Saito, Y.; Kawabata, K.; Okuda, M. *Journal of Physical Chemistry* **1995**, *99*, 16076.

[16]. Saito, Y.; Nishikubo, K.; Kawabata, K.; Matsumoto, T. *Journal of Applied Physics* **1996**, *80*, 3062.

[17]. Sawada, S.; Hamada, N. *Solid State Communications* **1992**, *83*, 917.

[18]. Lucas, A. A.; Lambin, P. H.; Smalley, R. E. *Journal of Physics and Chemistry of Solids* **1993**, *54*, 587.

[19]. Tang, Z. K.; Sun, H. D.; Wang, J.; Chen, J.; Li, G. *Applied Physics Letters* **1998**, *73*, 2287.

[20]. Robertson, N.; McGowan, C. A. *Chemical Society Reviews* **2003**, *32*, 96.

[21]. Guo, T.; Nikolaev, P.; Thess, A.; Colbert, D. T.; Smalley, R. E. *Chemical Physics Letters* **1995**, *243*, 49.

[22]. Thess, A.; Lee, R.; Nikolaev, P.; Dai, H. J.; Petit, P.; Robert, J.; Xu, C. H.; Lee, Y. H.; Kim, S. G.; Rinzler, A. G.; Colbert, D. T.; Scuseria, G. E.; Tomanek, D.; Fischer, J. E.; Smalley, R. E. *Science* **1996**, *273*, 483.

[23]. Hafner, J. H.; Bronikowski, M. J.; Azamian, B. R.; Nikolaev, P.; Rinzler, A. G.; Colbert, D. T.; Smith, K. A.; Smalley, R. E. *Chemical Physics Letters* **1998**, *296*, 195.

[24]. Fonseca, A.; Hernadi, K.; Piedigrosso, P.; Colomer, J. F.; Mukhopadhyay, K.; Doome, R.; Lazarescu, S.; Biro, L. P.; Lambin, P.; Thiry, P. A.; Bernaerts, D.; Nagy, J. B. *Applied Physics a-Materials Science & Processing* **1998**, *67*, 11.

[25]. Kong, J.; Cassell, A. M.; Dai, H. J. *Chemical Physics Letters* **1998**, *292*, 567.

[26]. Nikolaev, P.; Bronikowski, M. J.; Bradley, R. K.; Rohmund, F.; Colbert, D. T.; Smith, K. A.; Smalley, R. E. *Chemical Physics Letters* **1999**, *313*, 91.

[27]. Schlittler, R. R.; Seo, J. W.; Gimzewski, J. K.; Durkan, C.; Saifullah, M. S. M.; Welland, M. E. *Science* **2001**, *292*, 1136.

[28]. Dai, H. J. *Surface Science* **2002**, *500*, 218.

[29]. Bernier, P.; Maser, W.; Jouret, C.; Loiseau, A.; de la Chapelle, M. L.; Lefrant, S.; Lee, R.; Fischer, J. E. *Carbon* **1998**, *36*, 675.

[30]. Zhu, H. W.; Xu, C. L.; Wu, D. H.; Wei, B. Q.; Vajtai, R.; Ajayan, P. M. *Science* **2002**, *296*, 884.

[31]. Shenderova, O. A.; Zhirnov, V. V.; Brenner, D. W. *Critical Reviews in Solid State and Materials Sciences* **2002**, *27*, 227.

[32]. Yakobson, B. I.; Brabec, C. J.; Bernholc, J. *Physical Review Letters* **1996**, *76*, 2511.

[33]. Kim, P.; Shi, L.; Majumdar, A.; McEuen, P. L. *Physical Review Letters* **2001**, *87*, 215502.

[34]. Kong, J.; Yenilmez, E.; Tombler, T. W.; Kim, W.; Dai, H. J.; Laughlin, R. B.; Liu, L.; Jayanthi, C. S.; Wu, S. Y. *Physical Review Letters* **2001**, *87*, 106801.

[35]. Wei, B. Q.; Vajtai, R.; Ajayan, P. M. *Applied Physics Letters* **2001**, *79*, 1172.

[36]. Saito, R.; Dresselhaus, G.; Dresselhaus, M. S. *Journal of Applied Physics* **1993**, *73*, 494.

[37]. Avouris, P. *Accounts of Chemical Research* **2002**, *35*, 1026.

[38]. Weisman, R. B. *Nature Materials* **2003**, *2*, 569.

[39]. Krupke, R.; Hennrich, F.; von Lohneysen, H.; Kappes, M. M. *Science* **2003**, *301*, 344.

[40]. Chattopadhyay, D.; Galeska, L.; Papadimitrakopoulos, F. *Journal of the American Chemical Society* **2003**, *125*, 3370.

[41]. Zheng, M.; Jagota, A.; Strano, M. S.; Santos, A. P.; Barone, P.; Chou, S. G.; Diner, B. A.; Dresselhaus, M. S.; McLean, R. S.; Onoa, G. B.; Samsonidze, G. G.; Semke, E. D.; Usrey, M.; Walls, D. J. *Science* **2003**, *302*, 1545.

[42]. Chen, Z. H.; Du, X.; Du, M. H.; Rancken, C. D.; Cheng, H. P.; Rinzler, A. G. *Nano Letters* **2003**, *3*, 1245.

[43]. Cinke, M.; Li, J.; Chen, B.; Cassell, A.; Delzeit, L.; Han, J.; Meyyappan, M. *Chemical Physics Letters* **2002**, *365*, 69.

[44]. Lafi, L.; Cossement, D.; Chahine, R. *Carbon* **2005**, *43*, 1347.

[45]. Stan, G.; Cole, M. W. *Surface Science* **1998**, *395*, 280.

[46]. Shi, W.; Johnson, J. K. *Physical Review Letters* **2003**, *91*, 015504.

[47]. Talapatra, S.; Zambano, A. Z.; Weber, S. E.; Migone, A. D. *Physical Review Letters* **2000**, *85*, 138.

[48]. Zambano, A. J.; Talapatra, S.; Migone, A. D. *Physical Review B* **2001**, *64*, 075415.

[49]. Rols, S.; Johnson, M. R.; Zeppenfeld, P.; Bienfait, M.; Vilches, O. E.; Schneble, J. *Physical Review B* **2005**, *71*, 155411.

[50]. Simonyan, V. V.; Johnson, J. K.; Kuznetsova, A.; Yates, J. T., Jr. *Journal of Chemical Physics* **2001**, *114*, 4180.

[51]. Rawat, D. S.; Heroux, L.; Krungleviciute, V.; Migone, A. D. *Langmuir* **2006**, *22*, 234.

[52]. Kondratyuk, P.; Wang, Y.; Johnson, J. K.; Yates, J. T., Jr. *Journal of Physical Chemistry B* **2005**, *109*, 20999.

[53]. Peigney, A.; Laurent, C.; Flahaut, E.; Bacsa, R. R.; Rousset, A. *Carbon* **2001**, *39*, 507.

[54]. Kuznetsova, A.; Yates, J. T., Jr.; Liu, J.; Smalley, R. E. *Journal of Chemical Physics* **2000**, *112*, 9590.

[55]. Rinzler, A. G.; Liu, J.; Dai, H.; Nikolaev, P.; Huffman, C. B.; Rodriguez-Macias, F. J.; Boul, P. J.; Lu, A. H.; Heymann, D.; Colbert, D. T.; Lee, R. S.; Fischer, J. E.; Rao, A. M.; Eklund, P. C.; Smalley, R. E. *Applied Physics A - Materials Science & Processing* **1998**, *67*, 29.

[56]. Kuznetsova, A.; Mawhinney, D. B.; Naumenko, V.; Yates, J. T., Jr.; Liu, J.; Smalley, R. E. *Chemical Physics Letters* **2000**, *321*, 292.

[57]. Kuznetsova, A.; Yates, J. T., Jr.; Simonyan, V. V.; Johnson, J. K.; Huffman, C. B.; Smalley, R. E. *Journal of Chemical Physics* **2001**, *115*, 6691.

[58]. Kuznetsova, A.; Popova, I.; Yates, J. T.; Bronikowski, M. J.; Huffman, C. B.; Liu, J.; Smalley, R. E.; Hwu, H. H.; Chen, J. G. G. *Journal of the American Chemical Society* **2001**, *123*, 10699.

[59]. Mawhinney, D. B.; Naumenko, V.; Kuznetsova, A.; Yates, J. T., Jr.; Liu, J.; Smalley, R. E. *Chemical Physics Letters* **2000**, *324*, 213.

[60]. Mawhinney, D. B.; Naumenko, V.; Kuznetsova, A.; Yates, J. T., Jr.; Liu, J.; Smalley, R. E. *Journal of the American Chemical Society* **2000**, *122*, 2383.

[61]. Jakubek, Z. J.; Simard, B. *Langmuir* **2004**, *20*, 5940.

[62]. Arab, M.; Picaud, F.; Ramseyer, C.; Babaa, M. R.; Valsaque, F.; McRae, E. *Chemical Physics Letters* **2006**, *423*, 183.

[63]. Babaa, M. R.; Dupont-Pavlovsky, N.; McRae, E.; Masenelli-Varlot, K. *Carbon* **2004**, *42*, 1549.

[64]. Babaa, M. R.; Stepanek, I.; Masenelli-Varlot, K.; Dupont-Pavlovsky, N.; McRae, E.; Bernier, P. *Surface Science* **2003**, *531*, 86.

[65]. Matranga, C.; Bockrath, B. *Journal of Physical Chemistry B* **2005**, *109*, 9209.

[66]. Talapatra, S.; Migone, A. D. *Physical Review Letters* **2001**, *8720*, 206106.

[67]. Calbi, M. M.; Cole, M. W. *Physical Review B* **2002**, *66*, 115413.

[68]. Gatica, S. M.; Stan, G.; Calbi, M. M.; Johnson, J. K.; Cole, M. W. *Journal of Low Temperature Physics* **2000**, *120*, 337.

[69]. Lasjaunias, J. C.; Biljakovic, K.; Sauvajol, J. L.; Monceau, P. *Physical Review Letters* **2003**, *91*, 025901.

[70]. Ancilotto, F.; Calbi, M. M.; Gatica, S. M.; Cole, M. W. *Physical Review B* **2004**, *70*, 165422.

[71]. Marcone, B.; Orlandini, E.; Toigo, F.; Ancilotto, F. *Physical Review B* **2006**, *74*, 085415.

[72]. Byl, O.; Liu, J. C.; Wang, Y.; Yim, W. L.; Johnson, J. K.; Yates, J. T., Jr. *Journal of the American Chemical Society* **2006**, *128*, 12090.

[73]. Byl, O.; Liu, J.; Yates, J. T., Jr. *Carbon* **2006**, *44*, 2039.

[74]. Hinds, B. J.; Chopra, N.; Rantell, T.; Andrews, R.; Gavalas, V.; Bachas, L. G. *Science* **2004**, *303*, 62.

[75]. Majumder, M.; Chopra, N.; Andrews, R.; Hinds, B. J. *Nature* **2005**, *438*, 44.

[76]. Majumder, M.; Chopra, N.; Hinds, B. J. *Journal of the American Chemical Society* **2005**, *127*, 9062.

[77]. Arora, G.; Wagner, N. J.; Sandler, S. I. *Langmuir* **2004**, *20*, 6268.

[78]. Chen, H. B.; Sholl, D. S. *Journal of the American Chemical Society* **2004**, *126*, 7778.

[79]. Jakobtorweihen, S.; Verbeek, M. G.; Lowe, C. P.; Keil, F. J.; Smit, B. *Physical Review Letters* **2005**, *95*, 044501.
[80]. Lee, K. H.; Sinnott, S. B. *Journal of Physical Chemistry B* **2004**, *108*, 9861.
[81]. Sinnott, S. B.; Mao, Z. A.; Lee, K. H. *Cmes-Computer Modeling in Engineering & Sciences* **2002**, *3*, 575.
[82]. Skoulidas, A. I.; Sholl, D. S.; Johnson, J. K. *Journal of Chemical Physics* **2006**, *124*, 054708.
[83]. Kondratyuk, P.; Wang, Y.; Liu, J.; Johnson, J. K.; J.T. Yates, J. *Journal of Physical Chemistry C* **2007**, *111*, 4578.
[84]. Rivière, J. C. *Surface analytical techniques*; Clarendon Press: Oxford, 1990.
[85]. Woodruff, D. P.; Delchar, T. A. *Modern techniques of surface science*, 2nd ed.; Cambridge University Press: Cambridge ; New York, 1994.
[86]. Yates, J. T., Jr. *Methods of Experimental Physics* **1985**, *22*, 425.
[87]. Gasser, R. P. H. *An introduction to chemisorption and catalysis by metals*; Oxford University Press: Oxford, 1985.
[88]. Kreuzer, H. J.; Payne, S. H. In *Dynamics of Gas-Surface Interactions*; C.T. Rettner, Ashfold, M. N. R., Eds.; The Royal Society of Chemistry: Cambridge, 1991.
[89]. Bozack, M. J.; Muehlhoff, L.; Russell, J. N., Jr.; Choyke, W. J.; Yates, J. T., Jr. *J. Vac. Sci. Technol. A* **1987**, *5*, 1.
[90]. Winkler, A.; Yates, J. T., Jr. *J. Vac. Sci. Technol. A* **1988**, *6*, 2929.
[91]. Yates, J. T., Jr. *Experimental Innovations in Surface Science: A guide to practical laboratory methods and instruments*; AIP Press : Springer: New York, 1998.
[92]. Shinskey, F. G. *Process control systems : application, design, and tuning*, 4th ed.; McGraw-Hill: New York, 1996.
[93]. Stan, G.; Bojan, M. J.; Curtarolo, S.; Gatica, S. M.; Cole, M. W. *Physical Review B* **2000**, *62*, 2173.
[94]. Duren, T.; Keil, F. J. *Chemical Engineering & Technology* **2001**, *24*, 698.
[95]. Meyer, E. F.; Feil, J. *Langmuir* **1994**, *10*, 2399.
[96]. Ulbricht, H.; Moos, G.; Hertel, T. *Physical Review Letters* **2003**, *90*, 095501.
[97]. Yin, Y. F.; Mays, T.; McEnaney, B. *Langmuir* **1999**, *15*, 8714.
[98]. Striolo, A.; Gubbins, K. E.; Chialvo, A. A.; Cummings, P. T. *Molecular Physics* **2004**, *102*, 243.
[99]. Hu, Y. H.; Ruckenstein, E. *Industrial & Engineering Chemistry Research* **2004**, *43*, 708.
[100]. Byl, O.; Kondratyuk, P.; Forth, S. T.; FitzGerald, S. A.; Chen, L.; Johnson, J. K.; Yates, J. T., Jr. *Journal of the American Chemical Society* **2003**, *125*, 5889.
[101]. Byl, O.; Kondratyuk, P.; Yates, J. T., Jr. *Journal of Physical Chemistry B* **2003**, *107*, 4277.
[102]. Kondratyuk, P.; Yates, J. T., Jr. *Chemical Physics Letters* **2004**, *383*, 314.
[103]. *CRC Handbook of Chemistry and Physics*; Lide, D. R., Ed.; CRC: Boca Raton, 2003.
[104]. Arab, M.; Picaud, F.; Devel, M.; Ramseyer, C.; Girardet, C. *Physical Review B* **2004**, *69*, 165401.
[105]. Pickett, G. T.; Gross, M.; Okuyama, H. *Physical Review Letters* **2000**, *85*, 3652.
[106]. Mickelson, W.; Aloni, S.; Han, W. Q.; Cumings, J.; Zettl, A. *Science* **2003**, *300*, 467.
[107]. Fan, X.; Dickey, E. C.; Eklund, P. C.; Williams, K. A.; Grigorian, L.; Buczko, R.; Pantelides, S. T.; Pennycook, S. J. *Physical Review Letters* **2000**, *84*, 4621.

[108]. Matranga, C.; Chen, L.; Smith, M.; Bittner, E.; Johnson, J. K.; Bockrath, B. *Journal of Physical Chemistry B* **2003**, *107*, 12930.

[109]. De Meyer, K. M. A.; Chempath, S.; Denayer, J. F. M.; Martens, J. A.; Snurr, R. Q.; Baron, G. V. *Journal of Physical Chemistry B* **2003**, *107*, 10760.

[110]. Sun, M. S.; Talu, O.; Shah, D. B. *Journal of Physical Chemistry* **1996**, *100*, 17276.

[111]. Millot, B.; Methivier, A.; Jobic, H. *Journal of Physical Chemistry B* **1998**, *102*, 3210.

[112]. Richards, R. E.; Rees, L. V. C. *Langmuir* **1987**, *3*, 335.

[113]. Zhu, W.; Kapteijn, F.; van der Linden, B.; Moulijn, J. A. *Physical Chemistry Chemical Physics* **2001**, *3*, 1755.

[114]. Kondratyuk, P.; Yates, J. T., Jr. *Chemical Physics Letters* **2005**, *410*, 324.

[115]. Winkler, A.; Yates, J. T., Jr. *J. Vac. Sci. Technol. A* **1988**, *6*, 2929.

[116]. Duane, S.; Kennedy, A. D.; Pendleton, B. J.; Roweth, D. *Phys. Lett. B* **1987**, *195*.

[117]. Brass, A.; Pendleton, B. J.; Chen, Y.; Robson, B. *Biopolymers* **1993**, *33*, 1307.

[118]. Clamp, M. E.; Baker, P. G.; Stirling, C. J.; Brass, A. *Journal of Computational Chemistry* **1994**, *15*, 838.

[119]. Humphreys, D. D.; Friesner, R. A.; Berne, B. J. *Journal of Physical Chemistry* **1994**, *98*, 6885.

[120]. Steele, W. A. *Surf. Sci.* **1973**, *36*, 317.

[121]. Martin, M. G.; Siepmann, J. I. *J. Phys. Chem. B* **1998**, *102*, 2569.

[122]. Martin, M. G.; Siepmann, J. I. *J. Phys. Chem. B* **1999**, *103*, 4508.

[123]. Poling, B. E.; Prausnitz, J. M.; O'Connell, J. P. *The properties of gases and liquids*, 5th ed.; McGraw-Hill: New York, 2001.

[124]. Hu, Y. H.; Ruckenstein, E. *Chemical Physics Letters* **2006**, *425*, 306.

[125]. Kolesnikov, A. I.; Zanotti, J. M.; Loong, C. K.; Thiyagarajan, P.; Moravsky, A. P.; Loutfy, R. O.; Burnham, C. J. *Physical Review Letters* **2004**, *93*, 035503.

[126]. Jakubek, Z. J.; Simard, B. *Langmuir* **2005**, *21*, 10730.

[127]. Korner, S. K.; Tucci, F. C.; Rudkevich, D. M.; Heinz, T.; Rebek, J. *Chemistry-a European Journal* **2000**, *6*, 187.

[128]. Shimizu, T.; Masuda, M.; Minamikawa, H. *Chemical Reviews* **2005**, *105*, 1401.

[129]. Kameta, N.; Masuda, M.; Minamikawa, H.; Goutev, N. V.; Rim, J. A.; Jung, J. H.; Shimizu, T. *Advanced Materials* **2005**, *17*, 2732.

[130]. Wohrle, D.; Schulzekloff, G. *Advanced Materials* **1994**, *6*, 875.

[131]. Morgan, M. T.; Carnahan, M. A.; Finkelstein, S.; Prata, C. A. H.; Degoricija, L.; Lee, S. J.; Grinstaff, M. W. *Chemical Communications* **2005**, 4309.

[132]. Ziegler, M.; Brumaghim, J. L.; Raymond, K. N. *Angewandte Chemie-International Edition* **2000**, *39*, 4119.

[133]. Fiedler, D.; Leung, D. H.; Bergman, R. G.; Raymond, K. N. *Journal of the American Chemical Society* **2004**, *126*, 3674.

[134]. Bozack, M. J.; Muehlhoff, L.; Russell, J. N., Jr.; Choyke, W. J.; Yates, J. T., Jr. *J. Vac. Sci. Technol. A* **1987**, *5*, 1.

[135]. Klein, R.; Scheer, M. D. *Journal of Physical Chemistry* **1958**, *62*, 1011.

[136]. Scheer, M. D.; Klein, R. *Journal of Physical Chemistry* **1961**, *65*, 375.

[137]. Klein, R.; Scheer, M. D. *Journal of Physical Chemistry* **1963**, *67*, 1874.

[138]. Klein, R.; Scheer, M. D. *Journal of Physical Chemistry* **1961**, *65*, 324.

[139]. Klein, R.; Scheer, M. D.; Kelley, R. *Journal of Physical Chemistry* **1964**, *68*, 598.

[140]. Yates, J. T., Jr. *Experimental innovations in surface science : a guide to practical laboratory methods and instruments*; AIP Press : Springer: New York, 1998.

[141]. Muha, R. J.; Gates, S. M.; Yates, J. T., Jr. *Rev. Sci. Instrum.* **1985**, *56*, 613.

[142]. Nikitin, A.; Ogasawara, H.; Mann, D.; Denecke, R.; Zhang, Z.; Dai, H.; Cho, K.; Nilsson, A. *Physical Review Letters* **2005**, *95*, 225507.

[143]. Zhang, G. Y.; Qi, P. F.; Wang, X. R.; Lu, Y. R.; Mann, D.; Li, X. L.; Dai, H. J. *Journal of the American Chemical Society* **2006**, *128*, 6026.

[144]. Jakobtorweihen, S.; Verbeek, M. G.; Lowe, C. P.; Keil, F. J.; Smit, B. *Phys. Rev. Lett.* **2005**, *95*, 044501.

[145]. Cao, D. P.; Wu, J. Z. *Langmuir* **2004**, *20*, 3759.

[146]. Sokhan, V. P.; Nicholson, D.; Quirke, N. *J. Chem. Phys.* **2000**, *113*, 2007.

[147]. Skoulidas, A. I.; Ackerman, D. M.; Johnson, J. K.; Sholl, D. S. *Phys. Rev. Lett.* **2002**, *89*, 185901.

[148]. Marmier, A.; Spohr, H.; Cooke, D. J.; Kerisit, S.; Brodholt, J. P.; Wilson, P. B.; Parker, S. C. *Molecular Simulation* **2005**, *31*, 385.

[149]. Marti, J.; Gordillo, M. C. *Journal of Chemical Physics* **2001**, *114*, 10486.

[150]. Ulbricht, H.; Kriebel, J.; Moos, G.; Hertel, T. *Chemical Physics Letters* **2002**, *363*, 252.

[151]. Gutsze, A.; Masierak, W.; Geil, B.; Kruk, D.; Pahlke, H.; Fujara, F. *Solid State Nuclear Magnetic Resonance* **2005**, *28*, 244.

[152]. Leroy, F.; Rousseau, B. *Molecular Simulation* **2004**, *30*, 617.

[153]. Favre, D. E.; Schaefer, D. J.; Auerbach, S. M.; Chmelka, B. F. *Physical Review Letters* **1998**, *81*, 5852.

[154]. von Meerwall, E.; Ozisik, R.; Mattice, W. L.; Pfister, P. M. *Journal of Chemical Physics* **2003**, *118*, 3867.

[155]. Geier, O.; Vasenkov, S.; Freude, D.; Karger, J. *Journal of Catalysis* **2003**, *213*, 321.

[156]. Schuring, D.; Jansen, A. P. J.; van Santen, R. A. *Journal of Physical Chemistry B* **2000**, *104*, 941.

[157]. Stallmach, F.; Karger, J.; Krause, C.; Jeschke, M.; Oberhagemann, U. *Journal of the American Chemical Society* **2000**, *122*, 9237.

[158]. Goddard, M.; Ruthven, D. M. *Zeolites* **1986**, *6*, 445.

[159]. Goddard, M.; Ruthven, D. M. *Zeolites* **1986**, *6*, 283.

[160]. Lorentz, P.; Bulow, M.; Karger, J. *Colloids and Surfaces* **1984**, *11*, 353.

[161]. Jobic, H.; Fitch, A. N.; Combet, J. *Journal of Physical Chemistry B* **2000**, *104*, 8491.

[162]. Ackerman, D. M.; Skoulidas, A. I.; Sholl, D. S.; Johnson, J. K. *Molec. Sim.* **2003**, *29*, 677.

[163]. Chen, H.; Sholl, D. S. *J. Am. Chem. Soc.* **2004**, *126*, 7778.

[164]. Mao, Z. G.; Sinnott, S. B. *J. Phys. Chem. B* **2000**, *104*, 4618.

[165]. Supple, S.; Quirke, N. *Phys. Rev. Lett.* **2003**, *90*, 214501.

[166]. Supple, S.; Quirke, N. *Journal of Chemical Physics* **2004**, *121*, 8571.

[167]. Jakobtorweihen, S.; Lowe, C. P.; Keil, F. J.; Smit, B. *J. Chem. Phys.* **2006**, submitted.

[168]. Krishna, R.; van Baten, J. M. *Ind. Eng. Chem. Res.* **2006**, *45*, 2084.

[169]. Skoulidas, A. I.; Sholl, D. S. *J. Phys. Chem. B* **2002**, *106*, 5058.

[170]. Skoulidas, A. I.; Sholl, D. S.; Johnson, J. K. *J. Chem. Phys.* **2006**, *124*, 054708.

[171]. Chen, H.; Sholl, D. S.; Johnson, J. K. *J. Phys. Chem. B* **2006**, *in press*.

[172]. Chesnokov, S. A.; Nalimova, V. A.; Rinzler, A. G.; Smalley, R. E.; Fischer, J. E. *Physical Review Letters* **1999**, *82*, 343.

[173]. Kondratyuk, P.; Yates, J. T., Jr. *Journal of Vacuum Science & Technology A* **2005**, *23*, 215.

[174]. Maginn, E. J.; Bell, A. T.; Theodorou, D. N. *Journal of Physical Chemistry* **1993**, *97*, 4173.

[175]. Theodorou, D. N.; Snurr, R. Q.; Bell, A. T. Molecular Dynamics and diffusion in microporous materials. In *Comprehensive Supramolecular Chemistry*; Alberti, G., Bein, T., Eds.; Pergamon Press: New York, 1996; Vol. 7; pp 507.

[176]. Martyna, G. J.; Tuckerman, M. E.; Tobias, D. J.; Klein, M. L. *Molecular Physics* **1996**, *87*, 1117.

[177]. Allen, M. P.; Tildesley, D. J. *Computer Simulation of Liquids*; Oxford University Press: New York, 1987.

[178]. Martin, M. G. http://towhee.sourceforge.net/.

[179]. Siepmann, J. I.; Frenkel, D. *Mol. Phys.* **1992**, *75*, 59.

[180]. Fichthorn, K. A.; Miron, R. A. *Physical Review Letters* **2002**, *89*, 196103.

[181]. Crank, J. *Mathematics of Diffusion*; University Press: Oxford, 1957.

[182]. Bard, A. J.; Faulkner, L. R. *Electrochemical Methods*; John Wiley & Sons: New York, 1980.

[183]. Douglass, D. C.; McCall, D. W. *Journal of Physical Chemistry* **1958**, *62*, 1102.

[184]. Calbi, M. M.; Riccardo, J. L. *Physical Review Letters* **2005**, *94*, 246103.

[185]. Paserba, K. R.; Gellman, A. J. *Journal of Chemical Physics* **2001**, *115*, 6737.

[186]. Paserba, K. R.; Gellman, A. J. *Phys. Rev. Lett.* **2001**, *86*, 4338.

[187]. Ebbesen, T. W. *Carbon nanotubes : preparation and properties*; CRC Press: Boca Raton, Fla., 1997.

[188]. Zimmerman, J. L.; Bradley, R. K.; Huffman, C. B.; Hauge, R. H.; Margrave, J. L. *Chemistry of Materials* **2000**, *12*, 1361.

[189]. Mawhinney, D. B.; Yates, J. T. *Carbon* **2001**, *39*, 1167.

[190]. Muris, M.; Dupont-Pavlovsky, N.; Bienfait, M.; Zeppenfeld, P. *Surface Science* **2001**, *492*, 67.

[191]. Fujiwara, A.; Ishii, K.; Suematsu, H.; Kataura, H.; Maniwa, Y.; Suzuki, S.; Achiba, Y. *Chemical Physics Letters* **2001**, *336*, 205.

[192]. Gatica, S. M.; Bojan, M. J.; Stan, G.; Cole, M. W. *Journal of Chemical Physics* **2001**, *114*, 3765.

[193]. Kostov, M. K.; Cole, M. W.; Lewis, J. C.; Diep, P.; Johnson, J. K. *Chemical Physics Letters* **2000**, *332*, 26.

[194]. Fournier, R. P.; Savoie, R.; Besette, F.; Cabana, A. *Journal of Chemical Physics* **1968**, *49*, 1159.

[195]. Yang, J. H.; Clark, L. A.; Ray, G. J.; Kim, Y. J.; Du, H.; Snurr, R. Q. *Journal of Physical Chemistry B* **2001**, *105*, 4698.

[196]. Zhukov, V.; Popova, I.; Yates, J. T. *Journal of Vacuum Science & Technology a-Vacuum Surfaces and Films* **2000**, *18*, 992.

[197]. Frisch, M. J., et al. Gaussian 98, Revision A.11.

[198]. Allen, M. P.; Tildesley, D. J. *Computer simulation of liquids*; Oxford University Press: Oxford England, 1987.

[199]. Rowley, R. L. *Statistical mechanics for thermophysical property calculations*; PTR Prentice Hall: Englewood Cliffs, NJ, 1994.

[200]. Snurr, R. Q.; Kärger, J. *Journal of Physical Chemistry B* **1997**, *101*, 6469.

[201]. Skoulidas, A. I.; Sholl, D. S. *J. Phys. Chem. B* **2001**, *105*, 3151.
[202]. Simonyan, V. V.; Johnson, J. K. *Manuscript in preparation*.
[203]. Nextoux, P.; Drifford, M.; Belloni, L.; Vinit, A. *Mol. Phys.* **1983**, *49*, 1375.
[204]. Rowland, B.; Kadagathur, N. S.; Devlin, J. P. *Journal of Chemical Physics* **1995**, *102*, 13.
[205]. Buch, V.; Delzeit, L.; Blackledge, C.; Devlin, J. P. *Journal of Physical Chemistry* **1996**, *100*, 3732.
[206]. Delzeit, L.; Devlin, M. S.; Rowland, B.; Devlin, J. P.; Buch, V. *Journal of Physical Chemistry* **1996**, *100*, 10076.
[207]. Jones, L. H.; Swanson, B. I. *Journal of Physical Chemistry* **1991**, *95*, 2701.
[208]. Gilbert, M.; Drifford, M. *Chem. Phys.* **1977**, *66*, 3205.
[209]. Daly, F. P.; Hopkins, A. G.; Brown, C. W. *Spectrochimica Acta* **1974**, *30A*, 2159.
[210]. Scherer, J. R. *Adv. Infrared Raman Spectrosc.* **1978**, *5*, 149.
[211]. Evans, J. C. *Spectrochimica Acta* **1960**, *16*, 994.
[212]. Evans, J. C.; Wright, N. *Spectrochimica Acta* **1960**, *16*, 352.
[213]. Bertie, J.; Devlin, J. P. *J. Chem. Phys.* **1983**, *79*, 2092.
[214]. Devlin, J. P.; Wooldridge, P. J.; Ritzhaupt, G. *J. Chem. Phys.* **1986**, *84*, 6095.
[215]. Scherer, J. R.; Go, M. K.; Kint, S. *J. Phys. Chem.* **1973**, *77*, 2108.
[216]. Herzberg, G. *Molecular spectra and molecular structure*; Van Nostrand: New York, 1996; Vol. II.
[217]. Turner, J. J. In *Handbook of vibrational spectroscopy*; Chalmers, J. M., Griffiths, P. R., Eds.; Wiley: New York, 2002; Vol. 1, p. 101.
[218]. Belhayara, K.; Chamma, D.; Henri-Rousseau, O. *Chemical Physics* **2003**, *293*, 31.
[219]. Shurvell, H. F. In *Handbook of vibrational spectroscopy*; Chalmers, J. M., Griffiths, P. R., Eds.; Wiley: New York, 2002; Vol. 3, p. 1787.
[220]. Duncan, J. L. *Spectrochimica Acta* **1991**, *47A*, 1.
[221]. Fina, L. J.; Yu, H. H. *Journal of Polymer Science Part B-Polymer Physics* **1992**, *30*, 1073.
[222]. Miyazawa, T. *J. Mol. Spectrosc.* **1960**, *4*, 168.
[223]. Flakus, H. T.; Chelmecki, M. *Journal of Molecular Structure* **2003**, *659*, 103.
[224]. Bratos, S. *J. Phys. Chem.* **1975**, *77*, 3499.
[225]. Stahl, H.; Appenzeller, J.; Martel, R.; Avouris, P.; Lengeler, B. *Physical Review Letters* **2000**, *85*, 5186.
[226]. Zhu, Y. F.; Yi, T.; Zheng, B.; Cao, L. L. *Applied Surface Science* **1999**, *137*, 83.
[227]. Krasheninnikov, A. V.; Nordlund, K.; Keinonen, J. *Physical Review B* **2002**, *65*, 165423.
[228]. Krasheninnikov, A. V.; Nordlund, K.; Keinonen, J.; Banhart, F. *Nuclear Instruments & Methods in Physics Research Section B-Beam Interactions with Materials and Atoms* **2003**, *202*, 224.
[229]. Krasheninnikov, A. V.; Nordlund, K.; Sirvio, M.; Salonen, E.; Keinonen, J. *Physical Review B* **2001**, *63*, 245405.